COUPLED PLASMA, FLUID AND THERMAL MODELING OF LOW-PRESSURE AND MICROSCALE GAS DISCHARGES

A Dissertation

Submitted to the Faculty

of

Purdue University

by

Gayathri Shivkumar

In Partial Fulfillment of the

Requirements for the Degree

of

Doctor of Philosophy

August 2019

Purdue University

West Lafayette, Indiana

THE PURDUE UNIVERSITY GRADUATE SCHOOL
STATEMENT OF DISSERTATION APPROVAL

Dr. Alina A. Alexeenko, Chair

School of Aeronautics and Astronautics

Dr. Timothy S. Fisher

Department of Mechanical and Aerospace Engineering, University of California, Los Angeles, CA

Dr. Sergey O. Macheret

School of Aeronautics and Astronautics

Dr. Jonathan Poggie

School of Aeronautics and Astronautics

Approved by:

Dr. Weinong Wayne Chen

Head of the School Graduate Program

Dedicated to my parents for always believing in me.

ACKNOWLEDGMENTS

I would like to express my deepest gratitude to my advisor, Prof. Alina Alexeenko, for constantly supporting and guiding my education and research. She has been a motivational mentor and a positive, impactful influence on my career choices and ambitions. Her help has been invaluable throughout my time at Purdue. I would like to thank Prof. Timothy Fisher for his expertise and guidance on the various aspects of carbon nanostructure deposition and Prof. Sergey Macheret for valuable lessons and discussions on plasma physics and engineering. Their advise and collaboration have been cruical and added great value to my graduate education. I thank Prof. Li Qiao for lending her microcombustion expertise to improve this work and Prof. Dimitrios Peroulis for his microfabrication advice. I would like to thank Prof. Jonathan Poggie for being a member of my committee and providing his valuable insight on plasma modeling.

I would like to thank Dr. Majed Alrefae for his experimental expertise and insightful discussions. Dr. Siva Sashank Tholeti for being a great friend and mentor through the years. All my research group members, especially Dr. Israel Sebastiao, Andrew Strongrich, Dr. Devon Parkos, Dr. Marat Kulakhmetov, Dr. Anthony Cofer, Han Luo and Nikhil Varma, for their advice, support and friendship. The faculty and staff of Purdue's School of Aeronautics and Astronautics for everything they have taught me and helped me with through the years.

I am eternally grateful to my professors at PESIT, Bangalore, Dr. TS. Prahlad and Dr. TR. Seetharam, for their kindness, mentorship and guidance throughout my undergraduate education. I thank Dr. Sherwin Shang and Dr. Steven Nail for being great sources of inspiration that I will always look up to and learn from. I would like to gratefully acknowledge the generosity and support of the National Science

Foundation, the Bilsland Dissertation Fellowship and the John and Patricia Rich Scholarship Fund.

I would like to thank all my friends, especially Abhishek Krishnan, Arjun Upadhya and Mughilan Ramasamy, for their incredible support, dependability, and for all the fun times. I owe a debt of gratitude to Prashanth Bangalore for being my best friend and a great companion. His encouragement, entertainment, trust and love have been an unparalleled source of positivity through the years. I thank Jamuna Ramanan for all her love and for always being there for me. My father, Shivkumar Adiseshan, for being my biggest critic and proudest cheerleader throughout my life. My mother, Revathi Shivkumar, for her endless patience, warmth, and encouragement and for instilling in me my love of math and problem solving. If I turn out to be half as kind and selfless as my parents, I will have succeeded.

TABLE OF CONTENTS

Page

LIST OF TABLES

LIST OF FIGURES

Figure Page

Figure Page

Figure Page

ABBREVIATIONS

CNT	carbon nanotube
CVD	chemical vapor deposition
PECVD	plasma enhanced chemical vapor deposition
MPCVD	microwave plasma chemical vapor deposition
R2R	roll-to-roll
RFCVD	radio frequency chemical vapor deposition
CC	capacitively coupled
RF	radio frequency
FE	field emission
DBD	dielectric barrier discharge
EHD	electrohydrodynamic
CFD	computational fluid dynamics
RANS	reynolds averaged navier-stokes
LES	large eddy simulations
PIV	particle image velocimetry
MEMS	micro-electro-mechanical systems
SEM	scanning electron microscope
OES	optical emission spectroscopy
PIC	particle-in-cell
MCC	monte carlo collisions
CRM	collision radiative model
RSS	root sum squared
FFT	fast fourier transform
PAI	plasma assisted ignition
PAC	plasma assisted combustion

NPD	nanosecond pulsed discharge
μC	microcombustion
MD	molecular dynamics
PAH	polycyclic aromatic hydrocarbons

ABSTRACT

Shivkumar, Gayathri PhD, Purdue University, August 2019. Coupled Plasma, Fluid and Thermal Modeling of Low-Pressure and Microscale Gas Discharges. Major Professor: Alina A. Alexeenko.

Large scale and cost-efficient synthesis of carbon nanostructured materials has garnered tremendous interest over the last decade owing to their plethora of engineering and bio-science applications. One promising method is roll-to-roll radio frequency chemical vapor deposition and this work presents a computational investigation of the capacitively coupled radio frequency plasma in such a system. The system operates at moderate pressures (less than 30 mbar) with an 80 kHz square wave voltage input. The computational model aids the understanding of plasma properties and $\alpha - \gamma$ transition parameters which strongly influence the nanostructure deposition characteristics in the system. One dimensional argon and hydrogen plasma models are developed to characterize the effects of input voltage, gas pressure, frequency, and waveform on the plasma properties. A hybrid mode which displays the characteristics of both α and γ discharges is found to exist for the low cycle frequency 80 kHz square wave voltage input due to the high frequency harmonics associated with a square waveform. The threshold voltage at which the transition between the different regimes occurs is higher for hydrogen than for argon owing to its diatomic nature. Collision radiative modeling is performed to predict the argon emission intensity in the discharge gap. The results are found to lie within 16% of the optical emission spectroscopy measurements with better agreement at the center of the discharge, where the measurement uncertainty is low and the emission by ions is not significant. A quasi-zero dimensional steady state chemistry model which uses the hydrogen plasma properties as inputs predicts high concentrations of C_2H, C_2H_2, $C_2H_3^+$, $C_2H_4^+$ and $C_2H_6^+$ during carbon nanostructure deposition.

Carbon nanostructures are popularly used as field emitters. Field emission based microplasma actuators generate highly non-neutral surface discharges that can be used to heat, pump, and mix the flow through microchannels and offer an innovative solution to the problems associated with microcombustion. They provide a constant source of heat to counter the large heat loss through the combustor surface, they aid in flow transport at low Reynolds numbers without the use of moving parts, and they provide a constant supply of radicals to promote chain branching reactions. This work presents two actuator concepts for the generation of field emission microplasma, one with offset electrodes and the other with planar electrodes. They operate at input voltages in the 275 to 325 V range at a frequency of 1 GHz which is found to be the most suitable value for flow enhancement. The momentum and energy imparted by the charged particles to the neutrals as modeled by 2D Particle-In-Cell with Monte Carlo Collisions (PIC/MCC) are applied to actuate flow in microchannels using 2D Computational Fluid Dynamics modeling. The planar electrode configuration is found to be more suitable for the purpose of heating, igniting and mixing the flow, as well as improving its residence time through a 10 mm long microcombustor. The combustion of hydrogen and air with the help of 4 such actuators, each with a power consumption of 47.5 mW/cm, generates power with an efficiency of 28.8%. Coating the electrode surface with carbon nanostructures improves the combustion efficiency by a factor of 2.5 and reduces the input voltage by a factor of 6.5. Such microcombustors can be applied to all battery based systems requiring micropower generation with the ultimate goal of “generating power on a chip”.

1. INTRODUCTION

1.1 Chemical Vapor Deposition of Carbon Nanostructures

Carbon nanostructures such as graphene, graphitic nanopetals and carbon nanotubes (CNTs) find a wide variety of applications owing to their exceptional electrical [1,2,3,4], structural [5,6] and thermal [7,8] properties. Graphitic nanopetals show exceptional performance as electrodes in Li-ion batteries [9], as flexible supercapacitors [10] and as glucose biosensors [11]. Graphene and graphitic nanopetals could be used to improve the electrical conductivity of composite materials used to protect aircraft fuselage from lightning strike damage [12]. Ultimately, graphene could replace all the steel in aircraft bodies on account of being much lighter in spite of being stronger and stiffer, thus improving the range and fuel efficiency. It is also applied as an ultra-thin coating to prevent oxidation in air [13] under vigorous flow boiling conditions [14]. Carbon nanotubes have potential applications in aircraft de-icing [15], in aircraft and spacecraft sensing [16], to reduce detectability of stealth aircraft, and in the construction of UAVs [17]. They may also be used as nanoparticle additives in chemical propellants for earlier ignition and extension of burning rate [18]. These nanostructures also find applications in transistors [19], hydrogen fuel cells [20, 21], and bone tissue engineering [22]. However, most of these applications are still in the developmental stages. Large scale utilization of these nanostructures requires cost-efficient and reproducible methods of synthesis, which have garnered tremendous interest over the last decade [23].

Chemical Vapor Deposition (CVD) is a technique that generates higher quality, more impervious and pure nanostructures in a reactor at ambient temperature when compared to other methods of synthesis such as laser ablation [24], exfoliation and cleavage [25], and arc discharges [26, 27]. Some of the popular types of CVD

used in the industry are direct liquid injection CVD, aerosol assisted CVD, atomic layer CVD, combustion CVD, photo initiated CVD and plasma assisted or plasma enhanced CVD. Plasma enhanced CVD (PECVD) has the advantage of requiring lower growth temperatures when compared to most other types. While Microwave Plasma Chemical Vapor Deposition (MPCVD) of diamond has been widely studied [28,29,30], this method has the disadvantage of being time consuming on account of being a batch (non-continuous) process.

Roll-to-Roll Radio Frequency Chemical Vapor Deposition (R2R RFCVD), on the other hand, allows for continuous deposition that can go on for hours or days. The Diener electronics RFCVD system, shown in Figure 1.1 (a), is capable of mass producing carbon nanostructures. In this system, the growth substrate is rolled through a Capacitively Coupled Radio Frequency (CCRF) plasma that is generated between two electrodes. A schematic of the process is shown in Figure 1.1 (b). The plasma is generated in a mixture of argon, hydrogen, methane, nitrogen and oxygen in gas pressure and equipment power ranges of 7 to 20 mbar and 500 to 1500 W, respectively. The free electrons in the plasma transfer energy to the methane gas molecules which dissociate to generate highly reactive radical precursors. These precursors combine to create a material film on the substrate. The system produces high quality nanostructures at low temperatures in a time and cost efficient manner.

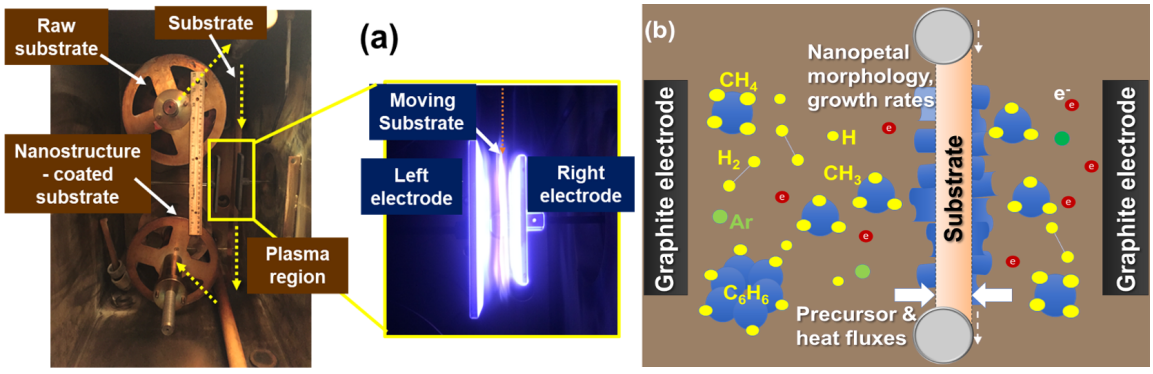

Figure 1.1. (a) Experimental setup and (b) schematic of the R2R RFCVD process.

Graphene is deposited by various CVD methods on transition metal substrates such as nickel, cobalt, copper etc. and most of the optimization advances have been achieved primarily through empirical methods [31, 32, 33, 34]. The process of graphene growth on substrates with high carbon solubility differ from the growth on substrates with low carbon solubility and these mechanisms are explained in the literature [35, 36]. The first step is called dissolution wherein the hydrocarbons are chemisorbed onto the metal surface, dissociate by dehydrogenation, and the carbon adatoms diffuse into the metal. However, the metal has a finite solubility limit, and when this limit is reached, the segregation step occurs. Here, the saturated carbon adatoms diffuse onto the surface of the metal substrate and segregate to form a layer of graphene. Thus, the deposition process is dependent on the solubility and is controlled by cooling the substrate surface, which reduces the carbon solubility limit. However, for copper which has almost zero solubility even at 1000 °C [35], the chemisorption and dissociation are followed by the formation of a carbon sheet on the surface. Thus, the temperature of the substrate does not affect the thickness of the graphene film. Consequently, in the present RFCVD system, a copper film is used as the substrate for graphene deposition.

1.2 Regimes of Operation of CCRF Plasma

Capacitively Coupled Radio Frequency (CCRF) plasmas manifest two distinct modes, the α and the γ, which have very different discharge structures as indicated by the light emission and electrical characteristics [37]. The α regime shows bright plasma layers close to the electrodes with dark gas between them. Electron impact ionization in the bulk sustains such a discharge [38]. The high conduction current in the discharge center is closed by high displacement current in the non-conducting sheath. The γ regime is similar to a glow discharge with a bright positive column in the center of the electrode gap. The secondary electrons multiply rapidly, leading to high conduction current in the sheath. The sheath thickness is close to the cathode

sheath thickness in a normal glow discharge [39]. Figure 1.2 shows the discharge structure appearance and sustaining ionization mechanism for both the regimes.

Figure 1.2. Schematic of the sustaining ionization processes for α and γ discharges.

The transition from the α to the γ regime has been studied extensively for sinusoidal input waveform in the MHz cycle frequency range [40,41,42,43,44,45,46,47,48]. Raizer *et al.* [39] describe the α discharge sheath as a gas gap containing no electrons. An increase in the current at the electrodes results in a higher discharge current density which raises the ion density in the sheath. This in turn increases the sheath voltage amplitude which eventually reaches the breakdown threshold in a gas gap nearly equal to the sheath thickness, triggering the transition from α to γ. The sheath voltage and thickness at breakdown correspond to approximately the electrode gap at the Paschen [49] minimum at that particular pressure. For a γ discharge, the ion current density at the electrode is close to the normal current density of a glow discharge. However, the normal current density is higher due to the addition of displacement current. The relative contribution of the displacement current decreases with increasing pressure. Godyak *et al.* [40] experimentally observed a change in the steepness of the I-V characteristics when the discharge transitions from α to γ as shown in Figure 1.3. The plasma density increases rapidly beyond the transition point, whereas the electron temperature at the gap center drops as seen in Figure 1.3.

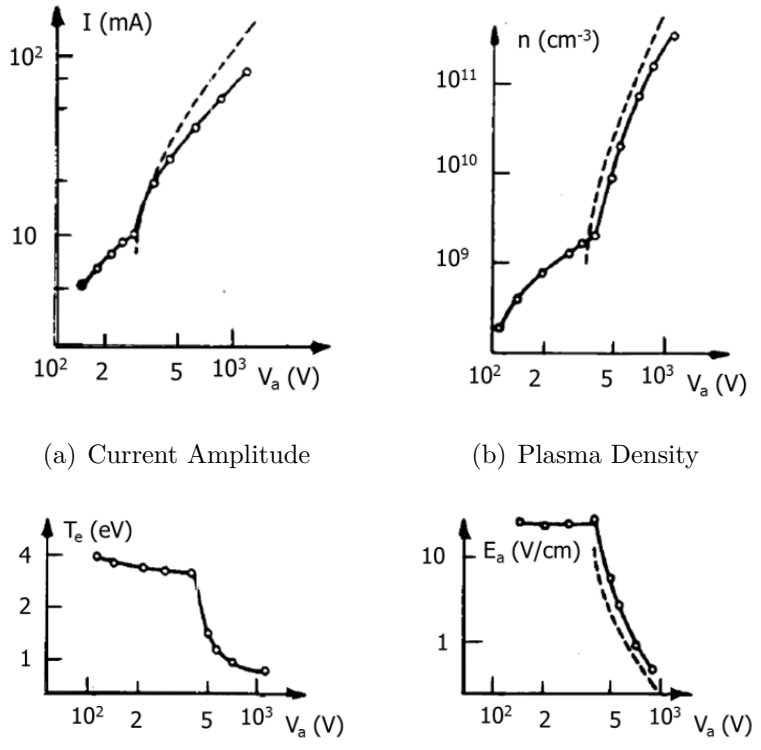

(a) Current Amplitude (b) Plasma Density

(c) Electron Temperature (d) Electric Field Amplitude

Figure 1.3. Variation of plasma properties with sinusoidal voltage wave amplitude for helium at $P_g = 3$ Torr, gap = 7.8 cm and $f_{cycle} = 3.2$ MHz. Solid lines: experiments, Dashed lines: calculations. From Godyak *et al.* [40].

At moderate pressures, the transition is abrupt and the discharge structure changes radically. The γ discharge bulk plasma possesses a fairly high electron temperature, close to that in an α discharge. However, at low pressures on the left branch of Paschen's curve [49], the sheath shrinkage that occurs while operating on the right branch of Paschen's curve is impossible. Thus, the transition is continuous and the γ discharge bulk electron temperature is lower than that in an α discharge [39]. Schweigert *et al.* [47] observed the existence of the 'volume dominated' and 'active sheath' modes instead of the α and γ modes in methane in the 0.01 to 1 Torr range. In molecular gases, the smaller electron energy relaxation length leads to the absence of

the high energy electron beams created by secondary electrons. Thus, they attributed the transition to the reduction in characteristic ionization length below the sheath length at some critical current density, rather than the electron avalanche produced by secondary electrons.

The transition voltage decreases with increasing applied frequency and the transitions become continuous at high frequencies [50, 51]. Although some work [52, 53] has been performed in the tens of kHz range, the α discharge is non-existent in this range for a sinusoidal wave input due to the absence of sheath displacement current. The displacement current is proportional to the driving frequency and at low frequencies, the current continuity in the sheath is not maintained by the low displacement current. The R2R RFCVD system studied in the present work uses a square wave input at 80 kHz cycle frequency and thus, the existence of α and γ modes under these conditions are investigated here.

1.3 Application of Carbon Nanostructures for Field Emission Plasma Assisted Microcombustion

Gas breakdown, described by Paschen's law [49], accounts for Townsend processes [54] namely, electron impact ionization in the bulk of the plasma and secondary electron emission from the cathode [55]. However, at microscale electrode gaps, quantum tunneling of electrons, due to high electric field at the electrodes leads to reduction of the breakdown voltage [56,57,58,59]. This tunneling process is termed field emission (FE) and is accounted for by the modified Paschen's curve [60] as shown by Figure 1.4. A schematic of all the charge generation processes in air is shown in Figure 1.5.

Surface discharges generated by Dielectric Barrier Discharge (DBD) actuators have been widely used to manipulate flow [62, 63, 64, 65, 66, 67, 68, 69]. The electrohydrodynamic (EHD) body force generated by the plasma transfers momentum from charged particles to neutrals, which enables directed flow actuation [70]. This EHD

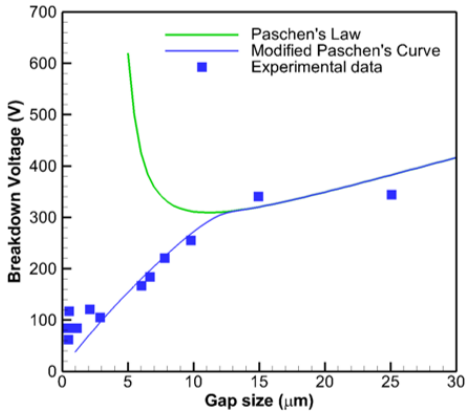

Figure 1.4. Paschen's and modified Paschen's curves for gold cathode [58, 61].

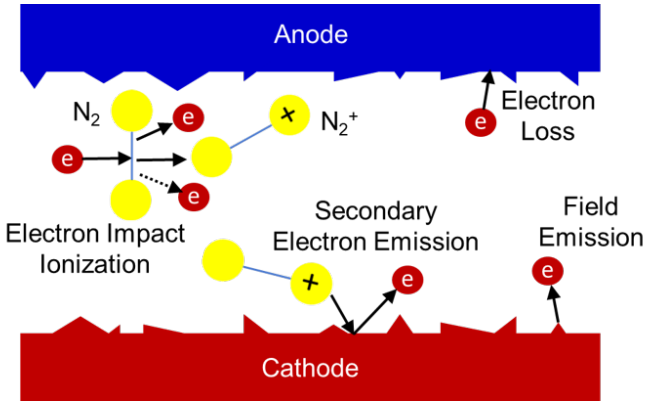

Figure 1.5. Charge generation processes in a DC discharge in air.

force, alternatively described as "ionic wind" [71], increases with the net space charge density. Consequently, substantial momentum transfer can only be expected in the cathode sheath region of glow discharges or the space-charge region of corona discharges for macro-scale actuators [72]. However, field-emission aided microdischarges are highly non-neutral, which leads to the generation of a large directed body force that can aid flow pumping.

Microscale DBD actuators have been used by Wang and Roy [73] for pumping applications. Ten actuators are placed in a T-shaped pump with two inlets and one outlet, all at atmospheric pressure. The separation between the DC driven electrodes in this case is 50 μm and thus, field emission does not play a major role in facilitating breakdown. In the present work, the DBD electrode gaps are reduced to less than 10 μm and thus, microplasma can be generated at low input voltages [74, 75, 76]. The field emission from such a device can be enhanced by coating the electrode surface with carbon nanopetals or nanotube arrays [77, 78, 79, 80] which creates irregularities to increase the surface roughness.

This study uses both theoretical and numerical modeling and the latter includes a combination of kinetic modeling for plasma and Computational Fluid Dynamics (CFD) modeling for fluid flow. Similar fluid, kinetic and hybrid modeling for DBD flow actuation has been widely performed and summarized in [81]. More recently, Babaeva *et al.* [82] performed fluid and hybrid modeling to quantify the effect of polarity and secondary electron emission on streamer propagation in nanosecond surface discharges. Fluid model for plasma was combined with Navier-Stokes solution for fluid flow in [83, 84, 85], and Euler solution for fluid flow in [86]. Shan *et al.* [87] used a combination of empirical and circuit models with unsteady Reynolds Averaged Navier Stokes (RANS) and Large Eddy Simulations (LES) solutions to simulate DBD plasma actuation. Benard *et al.* [88] modeled the time evolution of the DBD induced volumetric force based on Particle Image Velocimetry (PIV) flow-field measurements. In the present work, a method similar to [74, 85] is adopted, where kinetic modeling for plasma is combined with CFD modeling for fluid flow.

The continuing proliferation of micro-electro-mechanical systems (MEMS) for mobile communication, computing, wireless sensor and actuator networks, as well as unmanned aerial vehicles and picosatellites motivates the search for compact power generation and energy conversion technologies. Microscale combustion heat engines are an attractive solution owing to their potential for very high energy density and fast cycling when compared to currently used battery power sources. During the

last decade, research on combustion at meso and microscales has received a lot of interest [89, 90, 91]. The large surface-area-to-volume ratio of small scale combustors reduces the characteristic thermal inertia time, making combustion difficult to be initiated and sustained. This leads to three significant challenges with respect to the development of successful microcombustion power generation systems when compared to conventional scale reactors [91].

The first challenge is thermal quenching due to the increased surface-area-to-volume ratio. This causes the heat loss from the wall to exceed the heat release from the chemical reactions leading to reduction of the flame temperature and eventual flame extinction. The second is radical quenching due to the more frequent collision of species with the combustor walls rather than with other species. These species include important intermediate radicals for chain branching reactions, which slows down chemical reactions and leads to extinction. Lastly, it is difficult to control microcombustors because their operation requires similarly small-scale auxiliary components such as valves and pumps. Viscous losses greatly diminish the efficiency of conventional gas phase pumping methods and thus, microcombustors require new approaches for fuel-oxidizer pumping and mixing [91]. Plasma assisted microcombustion has to potential to overcome these problems and this work explores the application of FE-DBDs to aid microcombustion.

1.4 Motivation and Objectives

Carbon nanostructures such as graphene, graphitic nanopetals and carbon nanotubes have numerous potential applications and it is imperative to understand the underlying plasma processes for more efficient manufacturing. Recently, Alrefae *et al.* [92] demonstrated few layer graphene deposition on a Cu foil at web speeds as high as 1 m/min and Saviers *et al.* [93] coated graphitic nanopetals on a 1 m long carbon fiber substrate. These studies show the highest quality of few layer graphene deposition in the α mode and a decrease in the quality with increasing pressure and

power set point due to the α to γ transition leading to higher ion bombardment [92]. This can be seen in the Scanning Electron Microscope (SEM) images of the graphene deposited under both the CCRF plasma regimes shown in Figure 1.6. On the other hand, the growth of dense graphitic nanopetals with the desired morphology is favored by the γ mode [93]. This is because the growth rate, quality, type and morphology of the nanostructures deposited are controlled by the heat and mass fluxes onto the substrate. These depend on the plasma properties, temperature distributions and precursor concentrations in the vicinity of the substrate, which in turn are determined by the mode of operation of the CCRF discharge. Thus, characterizing the plasma properties of the α and γ modes of the system and the transition between the two are required to control and optimize the large-scale manufacturing of carbon nanostructures.

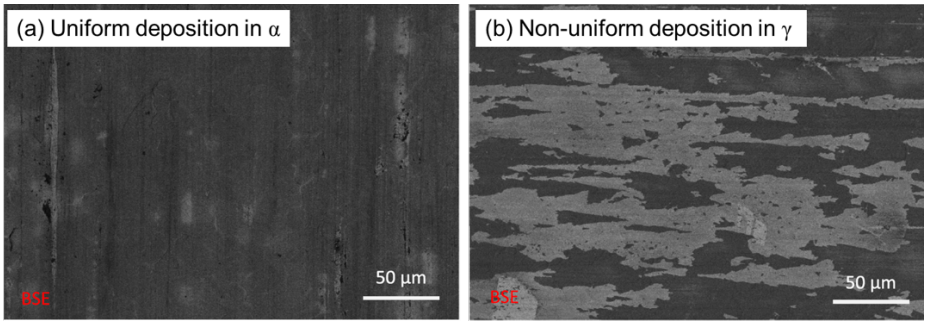

Figure 1.6. SEM images of graphene grown on a copper substrate in the R2R RFCVD system under (a) α and (b) γ discharge conditions [92].

Various gas mixtures of Ar, H_2, CH_4, N_2, and O_2 are used to deposit graphene in the RFCVD system [92, 93]. Ar and H_2 are used as carrier gases, and CH_4 is used to generate the carbon species for nanostructure deposition. N_2 and O_2 are used in small concentrations for doping and deposition rate enhancement. Since Ar and H_2 are the main gases used to generate plasma in the RFCVD system, this work focuses on developing plasma models for these carrier gases for an 80 kHz square wave voltage

input. Hydrocarbon chemistry is introduced to determine the predominant radical species responsible for carbon nanostructure deposition.

Plasma assited combustion at the macroscale has be used for decades in the form of spark ignition, nanosecond pulsed discharges and DBDs [94, 95, 96, 97, 98]. Although non-equilibrium macroscale plasmas indicate great potential for ignition and combustion, they require operational voltages on the order of 10 kV which is prohibitive to their integration in microsystems. However, FE-DBDs operate at input voltages on the order of 100 V [55] and their non-neutrality can overcome the viscous forces at microscales. When integrated in a microcombustor, they aid flow transport at low Reynolds numbers without the use of moving parts. The high energy electrons and ions in the plasma heat the gas which is favorable due to the requirement of a short ignition time. Plasma also stimulates the production of radicals such as hydroxyl and oxygen atoms that play a key role in the initiation and propagation of reactions, which ultimately result in ignition. The pre-exponent factor in the Arrhenius equation for these radicals is orders of magnitude higher in the presence of plasma [99]. The plasma also provides a constant source of heat to counter the large heat loss through the combustor surface. Thus, FE-DBD aided microcombustion shows promising potential for power generation in microsystems.

The goals of this dissertation are to characterize the plasma properties of the R2R RFCVD system, understand their effects on carbon nanostructure deposition, and to apply the nanostructures for FE-DBD aided microcombustion. The specific objectives to achieve the aforementioned goals are listed below.

Carbon nanostructure deposition objectives

- **Objective 1:** Develop a 1D argon plasma model in the R2R RFCVD system. Perform a parametric study to evaluate the effect of input voltage, pressure, frequency and waveform on the plasma properties.

- **Objective 2:** Perform collision radiative modeling of the simulated argon plasma and compare the results to experimental Optical Emission Spectroscopy (OES) measurements to validate the model.
- **Objective 3:** Implement hydrogen chemistry in the plasma model to evaluate the effect of gas composition on the plasma properties in the RFCVD system.
- **Objective 4:** Apply the hydrogen plasma modeling results to a quasi-0D hydrocarbon plasma chemistry model to determine the most important active species and radicals in the discharge during carbon nanostructure deposition.

Field emission assited microcombustion objectives

- **Objective 5:** Perform Particle-In-Cell with Monte Carlo Collisions (PIC/MCC) modeling of surface plasma generation in nitrogen using two different designs of FE-DBDs, one with offset electrodes and the other with planar electrodes. Evaluate the effect of the driving frequency on the plasma properties.
- **Objective 6:** Determine the electrohydrodynamic (EHD) characteristics of FE-DBDs and compare them to commonly used plasma devices for aerospace applications. Develop a theoretical model to evaluate the feasibility of flow actuation using FE-DBDs.
- **Objective 7:** Perform Computational Fluid Dynamics (CFD) modeling of atmospheric air actuation in microchannels using FE-DBDs. Compare the performance of the two different FE-DBD designs for the purpose of pumping, heating and mixing the flow in microchannels.
- **Objective 8:** Evaluate the feasibility of FE-DBD aided microcombustion in a MEMS microcombustor concept using CFD modeling.

The rest of this dissertation is organized as follows. Chapter 2 describes the argon plasma and collision radiative modeling of the RFCVD system and compares

the results to experimental measurements. Hydrogen plasma is modeled and the plasma properties are used to study hydrocarbon chemistry in Chapter 3. Chapter 4 presents the PIC/MCC modeling of plasma generated by two different designs of FE-DBDs. Chapter 5 outlines a theoretical microchannel flow model for plasma actuation, performs CFD modeling of FE-DBD actuated flow in microchannels, and studies the EHD characteristics of popular aerospace plasmas in comparison to FE-DBDs and the effect of coating the electrodes with carbon nanostructures. It also proposes a microcombustor concept and evaluates the ability of the FE-DBD plasma to initiate and sustain combustion in it. Chapter 6 summarizes the main findings and conclusions of this dissertation. Finally, chapter 7 suggests potential directions for future work to further the research presented here.

2. DISCHARGE REGIMES AND EMISSION CHARACTERISTICS OF CCRF ARGON PLASMA WITH A SQUARE WAVE INPUT

As a first step in understanding the RFCVD of carbon nanostructures, argon plasma is modeled in the system. This chapter describes the model, presents the predicted CCRF plasma properties and regime transitions, and compares the modeling results to experimental measurements.

2.1 Numerical Model

2.1.1 Plasma Model

A 1D CCRF plasma model in COMSOL Multiphysics is used to model the argon plasma in the R2R RFCVD system. The lowest pressure modeled is 5.5 mbar, for which the electron-neutral collision frequency is $\nu_m = 2.2 \times 10^{10}$ s^{-1} for argon plasma [37]. This is much higher than the RF frequency of 80 kHz or 5.03×10^5 s^{-1}. The fractional loss of electron energy per collision in argon is $\delta = 2.74 \times 10^{-5}$. The electron energy relaxation frequency is $\nu_m \delta = 6.03 \times 10^5$ s^{-1}, which is greater than the applied RF frequency even at the lowest pressure. The electrons relax faster than the applied electric field and react to instantaneous field values, and thus may be assumed to be in equilibrium. Owing to the small mass of electrons, their inertia may be neglected. The Knudsen number for electron-neutral collisions at the lowest pressure is about 1.6×10^{-3} and the plasma density is low with the highest ionization fraction $\sim 10^{-4}$. There are no large gradients in the flow. Thus, the continuum approach of the drift diffusion approximation for momentum and energy conservation of electrons is applied to model the plasma in the system.

The simulation setup consists of two electrodes separated by a distance of 4.5 cm as shown in Figure 2.1. A square wave voltage input with a cycle frequency of 80 kHz is applied at each of the electrodes. The DC bias and amplitude of the waveform correspond to the experimentally measured values at the corresponding pressure and input power setting on the system. The rise time for the square wave also corresponds to the that of the measured voltage waveform which limits the high frequency components associated with the voltage input. Three different gas pressure values of 5.5, 9.5 and 13.8 mbar are considered here. The current density, obtained as an output from the 1D model, is multiplied by the electrode area of 62.5 cm^2 to determine the current at the electrode, I_{el}. This in turn is used to determine the power at the electrode, P_{el}, as:

$$P_{el} = \frac{1}{T}\int_0^T V_{el} I_{el} dt \tag{2.1}$$

where, V_{el} is the voltage at the electrode, t is time and T is the cycle duration. This power is compared to experimental measurements in the following section. The setup for the experimental measurement of power, temperature and emission intensity is described in [100].

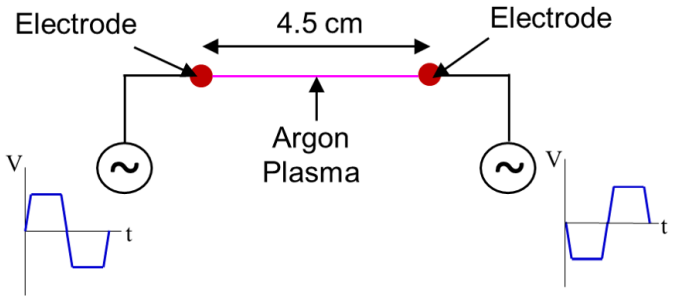

Figure 2.1. Simulation setup for the 1D plasma model.

In the CCRF plasma, the electric field, E, in the domain is obtained using Poisson's equation:

$$\frac{\partial E}{\partial x} = -\frac{\partial^2 V}{\partial x^2} = \frac{e}{\epsilon_0 \epsilon_r}\left(\sum_{ions} Z_+ n_+ - n_e\right) \tag{2.2}$$

where, the x-axis is oriented along the electrode gap, V is the electric potential, e is the electronic charge, ϵ_0 is the permittivity of free space, ϵ_r is the relative permittivity of the medium, Z_+ is the ionic charge, n_+ is the ion number density and n_e is the electron number density. The electron number density and mean electron energy, $\overline{\epsilon_e}$, are obtained using a fluid model with the drift diffusion approximation for electrons [101, 102]:

$$\frac{\partial n_e}{\partial t} + \frac{\partial \Gamma_e}{\partial x} = S_e \tag{2.3}$$

$$\Gamma_e = -\mu_e n_e E - D_e \frac{\partial n_e}{\partial x} \tag{2.4}$$

$$\frac{\partial n_e \overline{\epsilon_e}}{\partial t} + \frac{\partial \Gamma_\epsilon}{\partial x} + eE\Gamma_e = S_\epsilon \tag{2.5}$$

$$\Gamma_\epsilon = -\frac{5}{3}\mu_e n_e \overline{\epsilon_e} E - \frac{5}{3} D_e \frac{\partial n_e \overline{\epsilon_e}}{\partial x} \tag{2.6}$$

where, S_e is the net production rate of electrons, μ_e is the electron mobility, D_e is the electron diffusivity, and S_ϵ is the net rate of gain in electron energy.

The energy balance for ions is not considered since their temperature is assumed to be equal to the neutral gas temperature. The particle balances and fluxes of the neutral species and ions are determined by solving the modified Maxwell Stefan equations:

$$\rho \frac{\partial w_k}{\partial t} = \frac{\partial}{\partial x}\left(\rho w_k \left(\frac{D_k}{w_k}\frac{\partial w_k}{\partial x} + \frac{D_k}{M}\frac{\partial M}{\partial x} - Z_k \mu_k E\right)\right) + S_k \tag{2.7}$$

where, the subscript k represents the properties of the species k which includes all ions and neutrals, ρ is the total density, w is the mass fraction, D is the Maxwell-Stefan diffusivity, M is the molar mass, Z is the charge, μ is the mobility, and S is the net production rate of the species.

The source terms, S_e, S_ϵ and S_k, in Eqs. 2.3, 2.5 and 2.7 are obtained from the chemistry model. The full set of considered gas phase reactions and the references for their rates or cross sections are given in Table 2.1.

The surface reactions modeled are the following:

$$Ar^+ \rightarrow Ar$$

Table 2.1. Gas phase reactions modeled for Ar chemistry.

Reaction	**Chemical reaction**	**Reference**
Elastic	$e + Ar \rightarrow e + Ar$	[103]
Excitation	$e + Ar \rightarrow e + Ar^*$	[103]
Relaxation	$e + Ar^* \rightarrow e + Ar$	[103]
Ionization	$e + Ar \rightarrow 2e + Ar^+$	[103]
Ionization	$e + Ar^* \rightarrow 2e + Ar^+$	[104]
Binary quenching	$Ar^* + Ar \rightarrow Ar + Ar$	[105]
Recombination	$2e + Ar^+ \rightarrow e + Ar$	[105]
Ionization	$Ar^* + Ar^* \rightarrow e + Ar + Ar^+$	[106]
Dimer formation	$Ar^* + Ar + Ar \rightarrow Ar_2^* + Ar$	[106]
Ion conversion	$Ar + Ar + Ar^+ \rightarrow Ar + Ar_2^+$	[106]
Recombination	$e + Ar_2^+ \rightarrow Ar + Ar$	[106]
Ionization	$e + Ar_2^* \rightarrow 2e + Ar_2^+$	[107]
Dissociation	$e + Ar_2^+ \rightarrow e + Ar^+ + Ar$	[108]

$$Ar^* \rightarrow Ar$$

$$Ar_2^+ \rightarrow Ar$$

Secondary electron emission is modeled as a boundary condition at the graphite electrodes. The secondary electron emission coefficient, γ, is calibrated to match the electrode power at 9.5 mbar and $V_{amp} = 186$ V. In the model, the voltage waveform at the electrode, V_{el}, is provided as an input and the current waveform, I_{el}, is obtained as an output. These are used to calculate the cycle averaged power at the electrode, P_{el} based on Eq. 2.1. The electrode power is also determined experimentally from the voltage and current measurements. The values are averaged over 10 steady state cycles for simulations and 5 cycles for experiments. The variation of predicted elec-

trode power with γ values is shown in Table 2.2. Since the deviation of the modeled power at $\gamma = 0.02$ from the experimental value of 155.7 W is under 10%, this value is chosen as the input for all the cases modeled here.

Table 2.2. Variation of computational electrode power with secondary electron emission coefficient at $P_g = 9.5$ mbar and $V_{amp} = 186$ V. The experimental power at the electrode is 155.7 W.

$\boldsymbol{\gamma}$	$\boldsymbol{P_{el}}$ **[W]**
0.005	32.7
0.01	66.6
0.02	140.5
0.03	231.0
0.1	11214.07

The gas temperature, T_g, is determined using a heat transfer solver that models conduction, free convection and energy transfer from the electrons as given by:

$$k_g \frac{\partial^2 T_g}{\partial x^2} + Q_g - Q_{conv} = 0 \tag{2.8}$$

where, k_g is the thermal conductivity of the gas and Q_g is the power density imparted to the gas during collisions with electrons [109]:

$$Q_g = \frac{3}{2}\delta n_e \nu_m k_B \left(T_e[K] - T_g[K]\right) \tag{2.9}$$

where, δ is the fractional energy loss of an electron per collision and ν_m is the momentum transfer collision frequency for electron neutral collisions. Q_{conv} is the power density lost by the gas due to free convection given by:

$$Q_{conv} = h_{conv} A_{el} \left(T_{out} - T_{in}\right) \tag{2.10}$$

where A_{el} is the electrode area. The temperature of the gas leaving the plasma region, T_{out} is taken as the gas temperature being computed, T_g. The temperature of the

gas entering the plasma region is assumed to be at the same temperature as the electrodes. The experimentally measured electrode temperature [110], T_{el}, is imposed as a boundary condition for the heat transfer simulations. The values are derived from the results of $H_2/CH_4/Ar$ plasma [110] since it is assumed to be nearly independent of the gas mixture. The convective heat transfer coefficient, h_{conv} is fixed at 50 W/m^2-K based on the results of a convection model which is described in [110].

The plasma solver and heat transfer solver are coupled to each other and solved iteratively till a deviation in gas temperature of <5% from the previous iteration is attained. The algorithm is shown in Figure 2.2. The 1D gap is divided into 1000 elements with smaller elements closer to the electrodes. A grid convergence study is performed for the case with $P_g = 9.5$ mbar and $V_{amp} = 186$ V by increasing the number of elements by 100%. The maximum variation is 3.26% for the plasma solution and 0.30% for the heat transfer solver. Since the variation is <5%, the grid with 1000 elements is taken to be sufficiently converged and is used for all the computations. The adaptive time stepping method in COMSOL Multiphysics is used to determine and refine the time step based on the modeled physics. In order to determine that the simulations are temporally resolved, the relative tolerance is lowered in conjunction with a grid refinement. Reducing the relative tolerance by an order of magnitude from 10^{-3} to 10^{-4} produces a maximum deviation of 1.17% in the electron number density and 0.03% in the electron temperature. Thus, the results are temporally resolved.

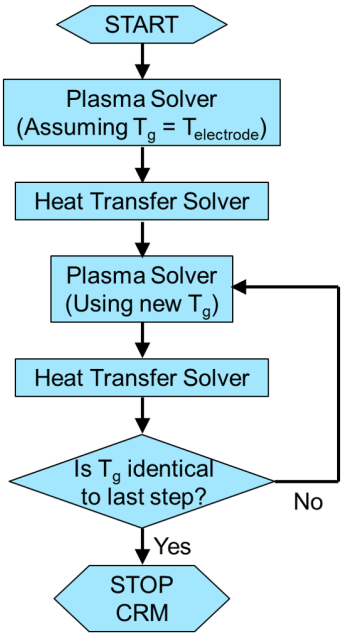

Figure 2.2. Flowchart for the solution algorithm.

2.1.2 Collision Radiative Model

The electron and ion number densities, electron temperature and gas temperature obtained from the plasma model are used as inputs in a Collision Radiative Model (CRM) to determine the emission intensity at various locations in the discharge which are compared to Optical Emission Spectroscopy (OES) results. The model is developed based on the argon CRM proposed in [111,112]. The CRM evaluates the steady state 0D kinetics of the ground state (*gs*) and first 40 excited states (*1s*, *2p*, *3d*, *2s* and *3p*). The energies of each state and their degeneracies can be found in [112]. The excitation rate coefficient from level i to level j, k_{ij}^{ex}, is determined from the excitation cross sections assuming a Maxwellian EEDF as [111]:

$$k_{ij}^{ex} = \sqrt{\frac{2}{m_e}} \int_{\Delta\epsilon_{ij}}^{\infty} \sigma_{ij}(\epsilon)\, \epsilon^{1/2} f(\epsilon)\, d\epsilon \tag{2.11}$$

where, m_e is the electron mass, ϵ is the electron energy, $f(\epsilon)$ is the EEDF, $\Delta\epsilon_{ij}$ is the excitation threshold energy and σ_{ij} is the electron-impact excitation cross section.

The excitation processes considered and the references for their cross sections are provided in Table 2.3. The relaxation rate coefficients, k_{ji}^{rel}, for each of the processes are determined by using detailed balance as:

$$k_{ji}^{rel} = \frac{g_i}{g_j} \exp\left(\Delta\epsilon_{ij}/T_e\right) k_{ij}^{ex} \tag{2.12}$$

where, g_i is the degeneracy of level i and T_e is the electron temperature in energy units. The ionization reaction rate coefficients, k_{i+}^{ion}, for each of the excited states are determined similar to Eq. 2.11 by using cross section data taken from [113, 114]. The recombination rate coefficients, k_{+i}^{rec}, are determined using the ionization rates based on detailed balance similar to Eq. 2.12. Ionization and recombination are only considered for the Ar^+ ion and not for the Ar_2^+ ion. The diffusion and quenching of the excited state neutrals are computed as [112]:

$$\nu_i^d = \begin{cases} \frac{Dn_i}{n_g}\sqrt{\frac{T_g}{300[K]}}\left(\frac{2405}{L}\right)^2 & \text{for } \; i = 2\ (1s_5) \text{ or } i = 4\ (1s_3) \\ 0 \quad \text{otherwise} \end{cases} \tag{2.13}$$

where, ν_i^d is the quenching probability per unit time, n_g is the gas number density, Dn_i is the diffusion coefficient of the metastable state at 300 K and L is the plasma characteristic length which is taken as the distance between the electrodes. The wavelengths, λ_{ij}, and Einstein coefficients, A_{ij}, for 133 optical transitions from level i to level j involving the 41 levels considered are obtained from [115]. The escape factor, Λ_{ij}, and reabsorption coefficient, κ_{ij}, are determined as [112]:

$$\kappa_{ij} = \frac{g_i}{g_j}\frac{\lambda_{ij}^3}{8\pi^{3/2}} n_j A_{ij} \sqrt{\frac{M}{2RT_g}} \tag{2.14}$$

$$\Lambda_{ij} = \frac{2 - \exp\left(-L\kappa_{ij}/1000\right)}{1 + L\kappa_{ij}} \tag{2.15}$$

where M is the molar mass and R is the gas constant.

The ideal gas law gives the population density of the ground state. The particle balance equation is used to determine the population densities of the excited states:

$$\begin{aligned} &\sum_{j\neq i} n_e n_j k_{ij}^{ex/rel} + n_e^2 n_+ k_{+i}^{rec} + \sum_{j>i} n_j A_{ji}\Lambda_{ji} \\ &-n_i \sum_{j\neq i} n_e k_{ij}^{ex/rel} - n_e n_i k_{i+}^{ion} - n_i \sum_{j<i} A_{ij}\Lambda_{ij} - n_i \nu_i^d = 0 \end{aligned} \tag{2.16}$$

where n_i is the number density of atoms in the ith level, n_+ is the Ar^+ ion number density, and ν_i^d is the diffusion coefficient for atoms in the ith level. Finally, the population densities determined by solving the system of 40 equations are used to evaluate the emission intensities of the optical transition spectral lines as [112]:

$$I_{ij}^{CRM} = C\ hc\frac{n_i A_{ij}\Lambda_{ij}}{\lambda_{ij}} \tag{2.17}$$

where the value of C is the correction factor which remains constant for all the lines. The intensities are normalized by the intensity of the 706.7 nm emission line which is chosen on account of having a high signal-to-noise ratio without detector saturation. The relative intensities [112] are computed as:

$$I_{ij}^{rel} = \frac{I_{ij}}{\sum\limits_{i,j} I_{ij}} \tag{2.18}$$

where the indexes i and j run through all the values in the wavelength range of 400 nm to 870 nm for direct comparison to experimental results. The Root Sum Squared (RSS) error is determined as a representation of the deviation in the relative emission intensity between OES and CRM as [112]:

$$\Delta = \sqrt{\sum_{ij}\left(I_{ij}^{rel,OES} - I_{ij}^{rel,CRM}\right)^2} \tag{2.19}$$

Table 2.3. Excitation processes considered in the CRM.

Process	**Reference**
$gs \rightarrow 1s$	[116, 117]
$gs \rightarrow 2p$	[116, 117]
$gs \rightarrow 3d$	[116, 117]
$gs \rightarrow 2s$	[116, 117]
$gs \rightarrow 3p$	[118]
$1s \rightarrow 1s$	[119]
$1s \rightarrow 2p$	[119]
$2p \rightarrow 2p$	[119]

2.2 Effect of Voltage and Pressure

This section presents the modeling results averaged over 10 steady state cycles and compares them to experimental measurements. The input square wave voltage has a cycle frequency of 80 kHz and a rise frequency in the range of 700 to 850 kHz based on the experimentally measured voltage waveform at the electrode. Figure 2.3 shows the time averaged electron number density profiles in the discharge gap at different voltage amplitudes and gas pressures. The electron density increases with voltage amplitude due to increase in the energy imparted into the system. A distinct transition in the discharge structure is observed when the voltage amplitude is increased. The average density in the center of the discharge increases by about 4 orders of magnitude and the profile loses its single central peak. The high pressure cases show more pronounced 2-peak profiles. The transition voltage increases with pressure and for discharges on the same side of the transition, the electron density increases with pressure due to an increase in the number of collisions.

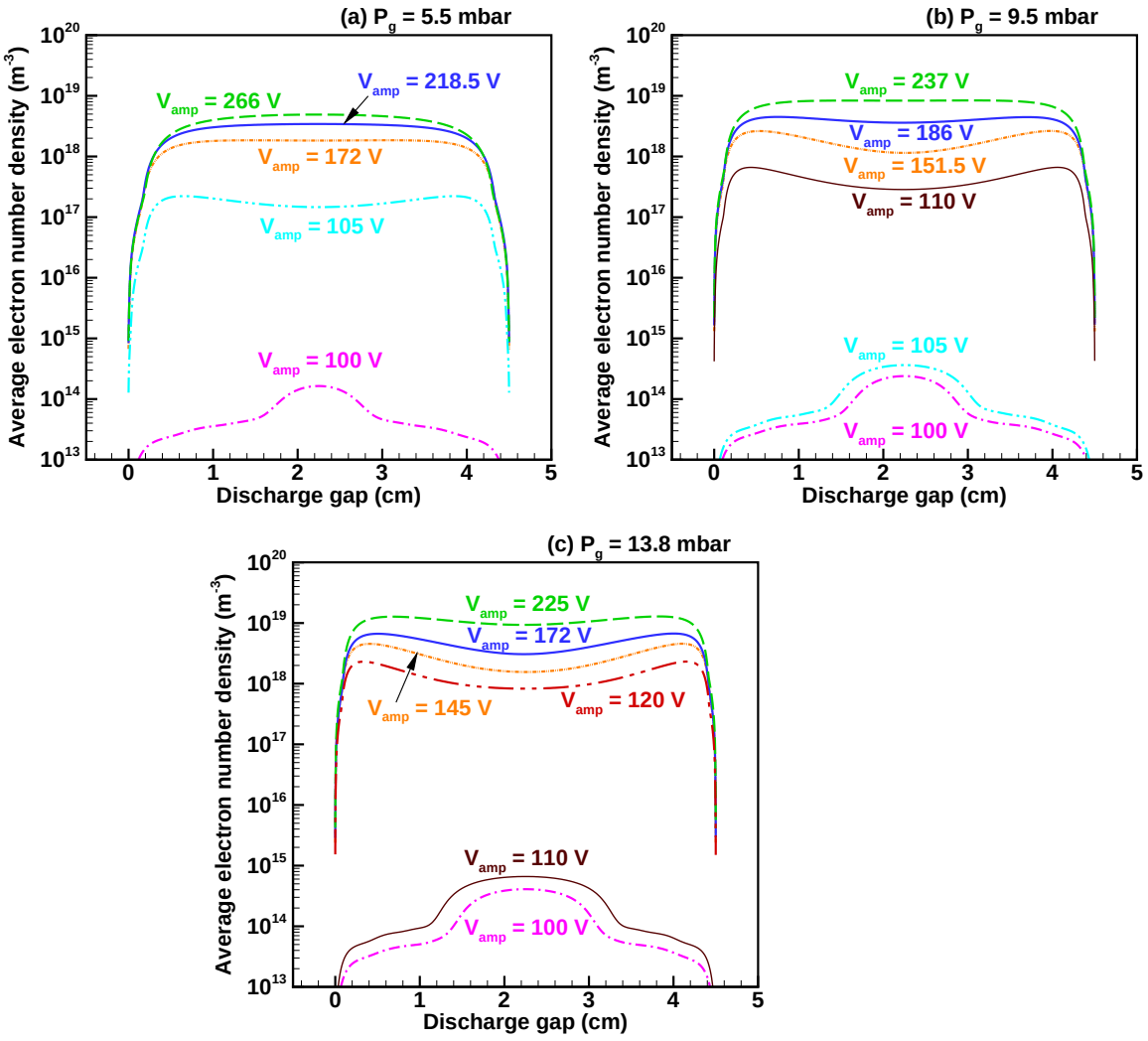

Figure 2.3. Variation of electron number density with voltage amplitude and gas pressure.

The time averaged electron temperature profiles shown in Figure 2.4 also displays a sharp transition in the discharge structure with a 1.3 times lower temperature at the center and at least 3 times higher temperature near the electrodes after the transition. The maximum electron temperature always occurs in the sheath region near the electrodes where most of the energy is imparted from the electric field to the electrons. Increasing the voltage amplitude imparts more energy increasing the

maximum electron temperature. On the other hand, increasing the gas pressure leads to increased collisions, which results in greater energy transfer from electrons to neutrals and reduces the electron temperature.

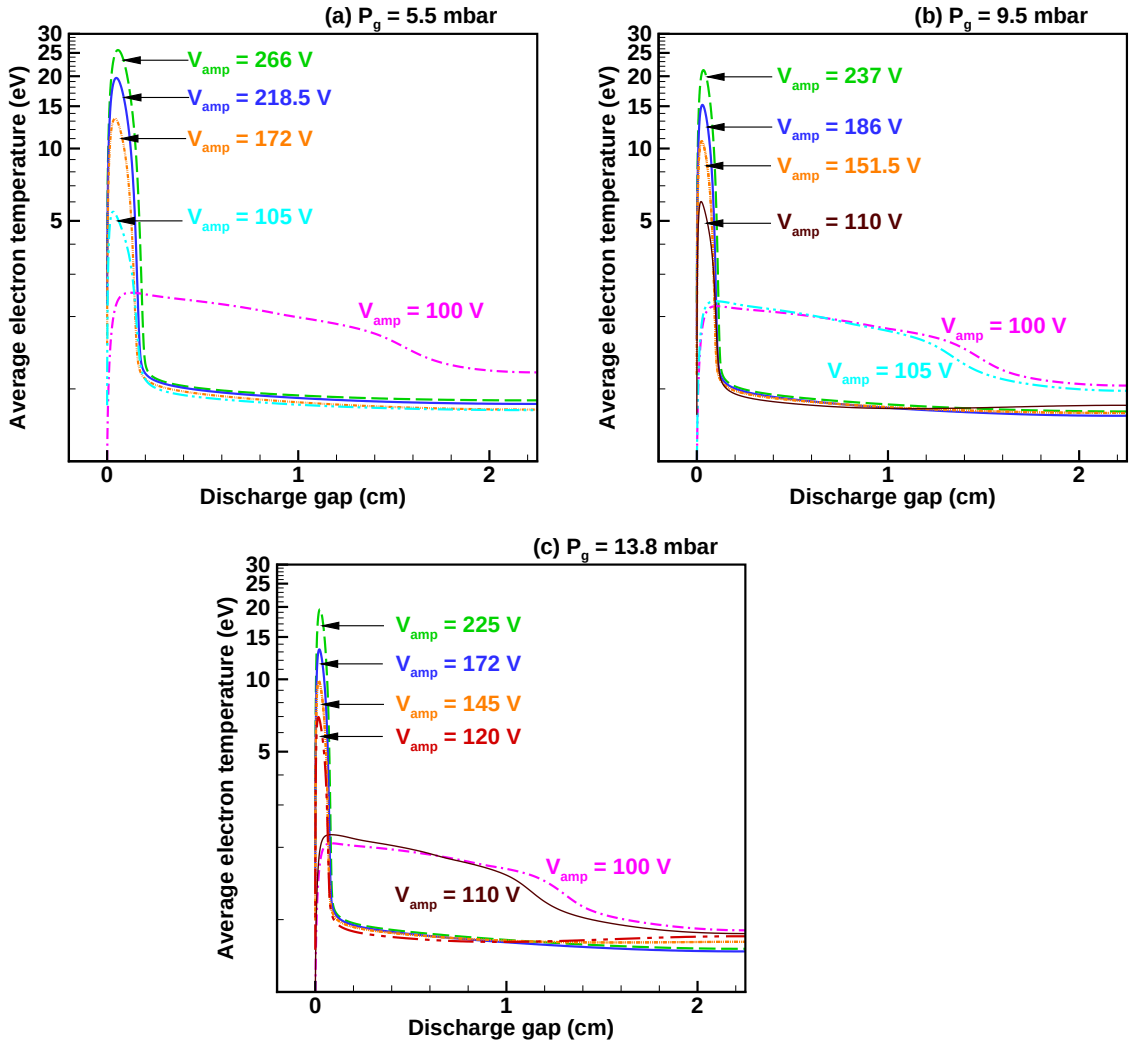

Figure 2.4. Variation of electron temperature with voltage amplitude and gas pressure. Profiles are shown for half the discharge gap.

The time averaged gas temperature profiles are shown in Figure 2.5. Higher voltage amplitude and gas pressure result in higher gas temperatures due to greater energy input and collisions, respectively. The gas temperature displays a uniform profile be-

fore the transition in discharge structure. Even though the electron temperature is higher in the center of the discharge, the 4 orders of magnitude lower electron density results in a negligibly small collisional heating source term, Q_g in Eq. 2.8, which leads to a constant gas temperature in the entire discharge.

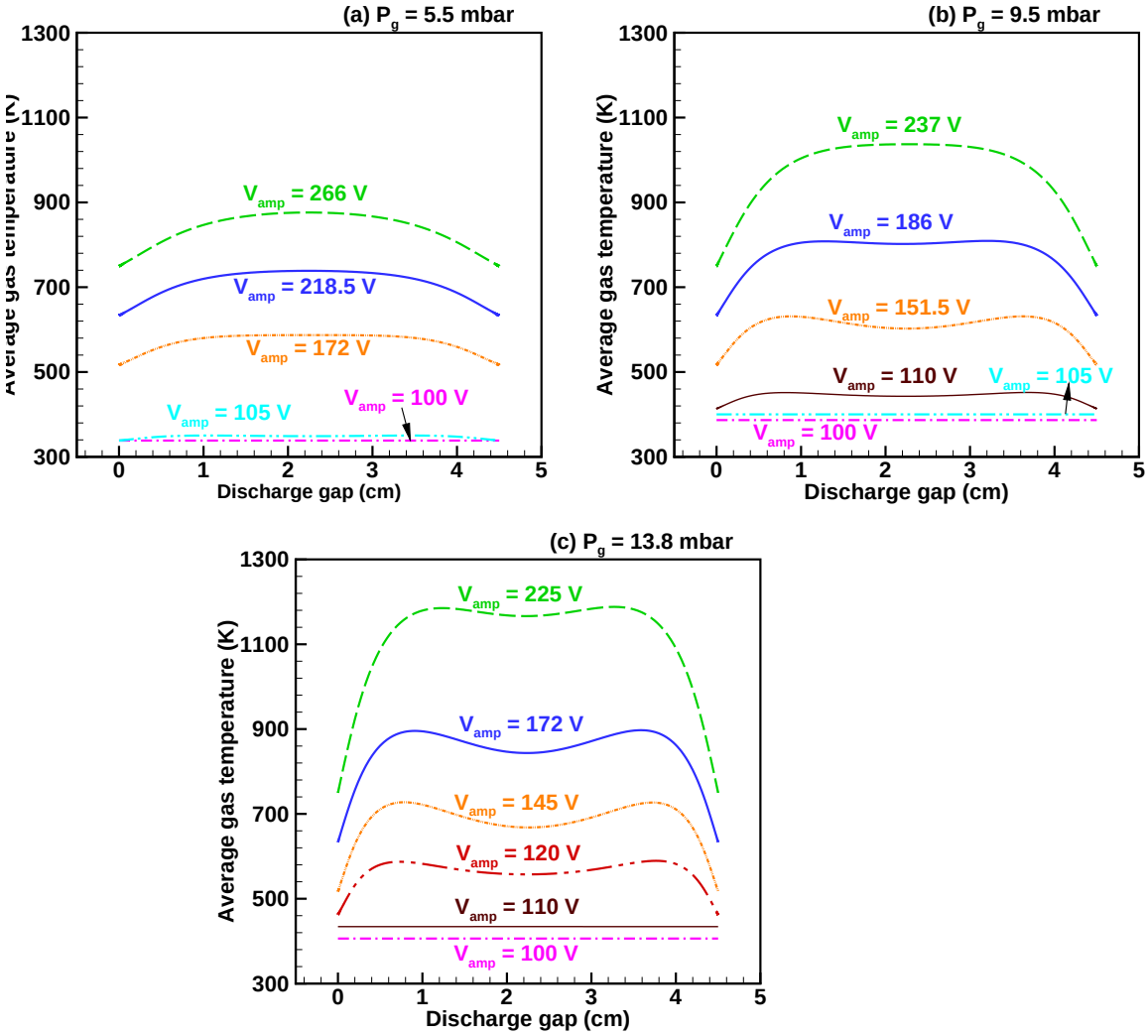

Figure 2.5. Variation of gas temperature density with voltage amplitude and gas pressure.

The transition in discharge structure in the MHz frequency range for sinusoidal wave input has been associated with $\alpha - \gamma$ transition in the literature. However, the

sustenance of α discharge for the tens of kHz range has not been observed due to the small displacement current. In order to understand the transition characteristics further, the sheath characteristics and the current density variation within the sheath are studied. Figure 2.6 shows the cycle averaged sheath thickness determined from the electron and ion number density profiles as the length of the non quasi-neutral region near the electrodes. Before the transition occurs, the sheath thickness is much larger than the gap corresponding to the Paschen minimum [49] at that pressure. Beyond the transition, however, the sheath thickness stays almost constant and equal to the Paschen minimum distance. This is characteristic of sheath breakdown in $\alpha - \gamma$ transitions.

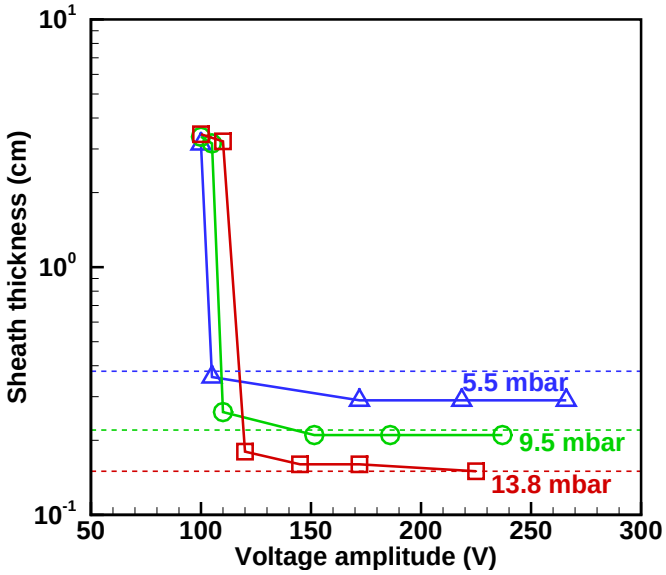

Figure 2.6. Variation of sheath thickness with voltage amplitude and gas pressure. The dotted lines show the Paschen minimum distance at each pressure.

Figure 2.7 shows the maximum contribution of displacement current to the total current density in the sheath at different instances of time in one input cycle. For the 100 V case, the current at the time of rise or fall of input voltage is higher than that when the voltage stays constant. Moreover, all the current in the sheath at the

rise or fall instant is due to displacement current, which indicates a non-conducting sheath, characteristic of an α discharge. As the voltage is increased, the current in the constant voltage part of the cycle exceeds that during the rise or fall of voltage indicating a transition in the discharge type. The contribution of displacement current for the 172 V case at the rise or fall instant is 70% of the total current. It falls to a low value of 15% for the 225 V case which is representative of a γ discharge. The characteristics displayed by all the voltage amplitudes $\geq$ 105 V at 5.5 mbar, 110 V at 9.5 mbar, and 120 V at 13.8 mbar are similar to that of the 172 V case at 13.8 mbar. These cases show electron number density and temperature profiles similar to a γ discharge, but high sheath displacement current at instances of voltage variation similar to an α discharge. This intermediate discharge between the pure α and γ regimes is referred to in this work as a "hybrid mode" owing to its mixed characteristics.

The existence of the α and hybrid modes at a cycle frequency 80 kHz is possible due to the higher frequency harmonics associated with the square wave voltage input. Fast Fourier Transform analysis of the measured waveform to extract the high frequency components is performed and the results are shown in the following subsection. The hybrid mode operates like an α discharge during the rise or fall of voltage, and like a γ discharge when the voltage stays constant. Since the constant voltage lasts for a longer period of time in each cycle, the cycle averaged plasma properties are closer to those of a γ discharge. The transition from the hybrid mode to the γ mode occurs at lower voltages for higher pressures.

The RMS current density profiles are shown in Figure 2.8. The profiles in Figure 2.8 (a) are representative of the α mode dominated by displacement current in the sheath and conduction current in the center of the discharge. The profiles in Figure 2.8 (b) represent the hybrid mode. The contribution of the displacement current in the sheath drops more in the γ mode and the entire discharge is sustained mostly by the conduction current.

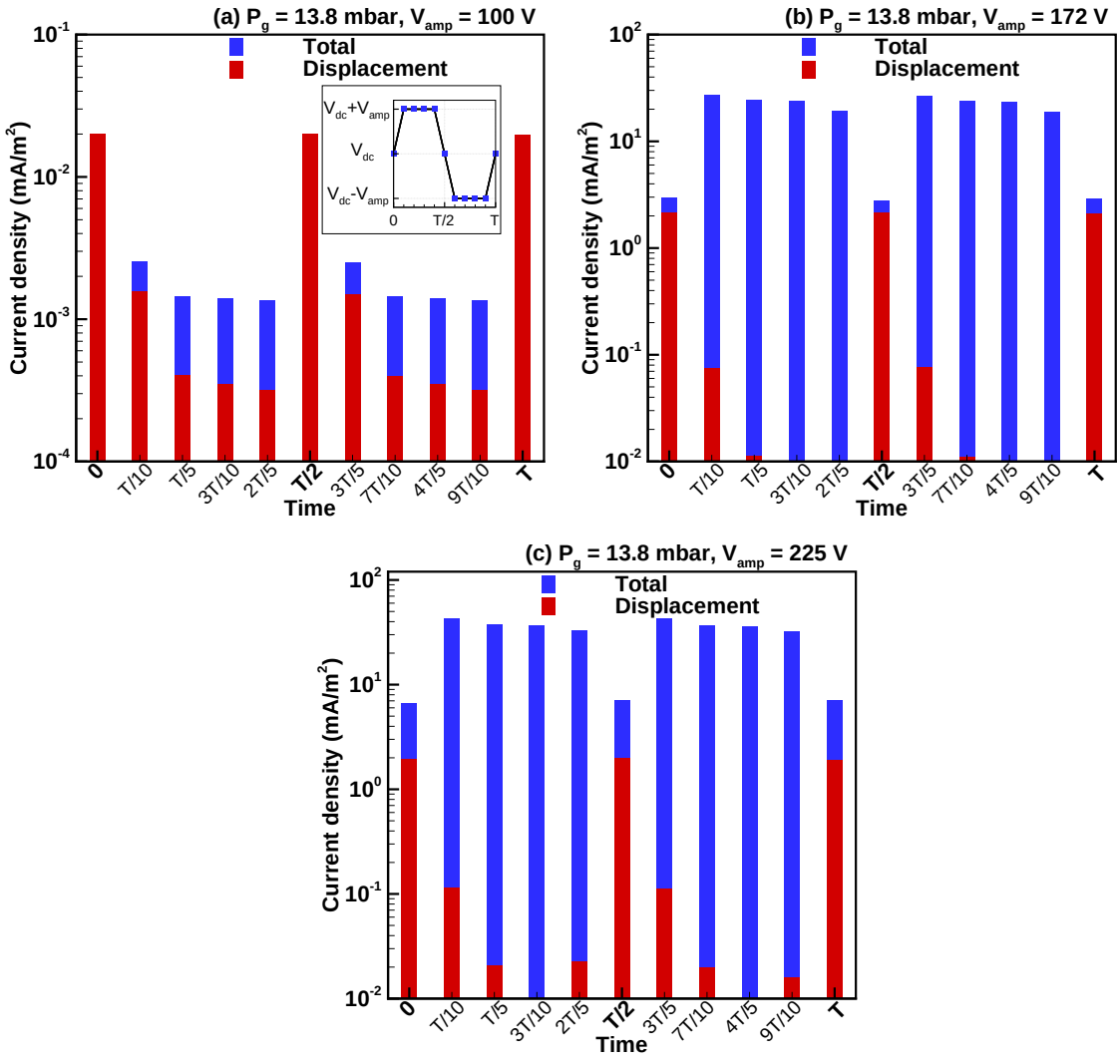

Figure 2.7. Maximum contribution of displacement current to the total current in the sheath at 13.8 mbar. T represents the cycle time. The inset in (a) shows the points in time when the current densities are plotted.

In order to characterize the sharp change in electron density profiles from the α to the hybrid mode, the characteristic ionization length, λ_{ion}, in the sheath is computed as:

$$\lambda_{ion} = \frac{j_e}{eS_e} \tag{2.20}$$

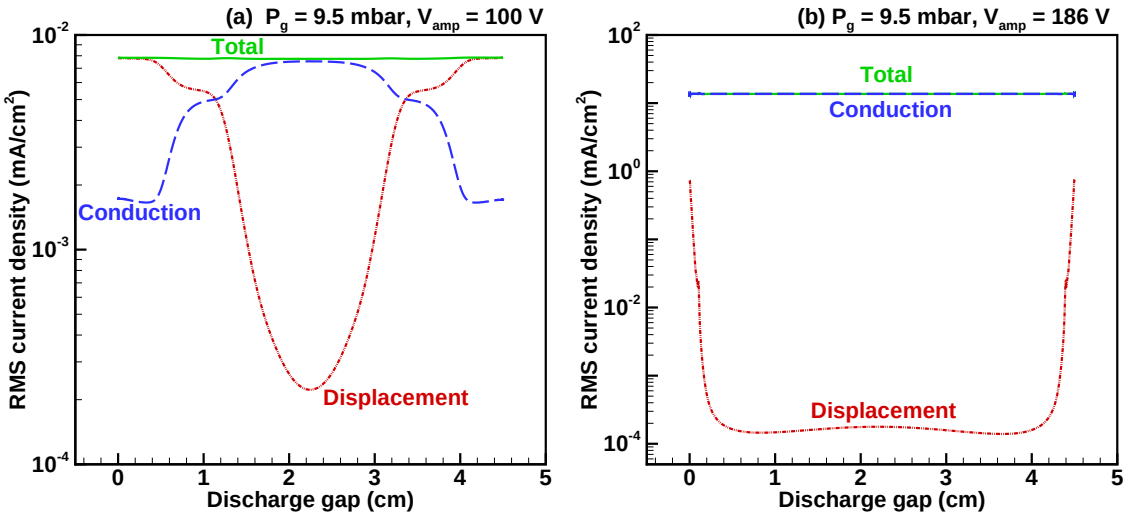

Figure 2.8. RMS current density profiles in the discharge gap at 9.5 mbar.

where, j_e is the electron current density and S_e is the net rate of production of electrons in $[\mathrm{m}^{-3}\mathrm{s}^{-1}]$. The 4 ionization reactions in Table 2.1 contribute positively and the 2 recombination reactions contribute negatively to S_e. If a constant average value of ion number density, $n_{i,sh}$ is assumed in the sheath, the α discharge sheath thickness, d_α is given by Raizer *et al.* [39] as:

$$d_\alpha = \frac{2j_{amp}}{e\omega n_{i,sh}} \tag{2.21}$$

where j_{amp} is the current density amplitude and ω is the driving frequency. The discharge structure transitions from α to hybrid mode when α sheath breaks down due to avalanche ionization caused by secondary electrons within the sheath. In other words, the discharge operates in the α regime when $\frac{\lambda_{ion}}{d_\alpha} >> 1$ and transitions to the hybrid mode or the γ regime if this ratio is less than or on the order of 1. This is corroborated by the values of ratio of ionization length to the α sheath length given in Table 2.4. The electron temperature is lower at higher pressure leading to larger ionization length. Consequently, the α to hybrid transition voltage increases with pressure. Beyond transition, higher voltage gives rise to higher electron current density leading to a slight increase in the ionization length.

Table 2.4. Ratio of characteristic ionization length to α sheath length and relation to mode of plasma operation.

Gas pressure, P_g **[mbar]**	**Voltage amplitude**, $\boldsymbol{V_{amp}}$ **[V]**	$\frac{\lambda_{ion}}{d_\alpha}$	**Mode of operation**
5.5	100	11.42	α
5.5	105	0.20	Hybrid
5.5	172	1.29	Hybrid
5.5	218.5	1.53	Hybrid
5.5	266	2.27	Hybrid
9.5	100	111.36	α
9.5	105	12.51	α
9.5	110	0.23	Hybrid
9.5	151.5	0.27	Hybrid
9.5	186	0.32	Hybrid
9.5	237	0.43	Hybrid
13.8	100	57.98	α
13.8	110	17.90	α
13.8	120	0.24	Hybrid
13.8	145	0.26	Hybrid
13.8	172	0.33	Hybrid
13.8	225	0.40	γ

Figure 2.9 shows the number density profiles of each of the heavy species in the α and hybrid modes. The dimer ions are present in abundance in the center of the discharge for the α mode, whereas in the hybrid mode, the Ar_2^+ number density is 2 orders of magnitude lower than the Ar^+ number density. For the hybrid mode, most of the excited species are present close to the sheath region, but for the α mode they are spread out in the entire discharge gap. The number densities of Ar^* and Ar_2^* are comparable for the α mode, whereas the dimers have two orders of magnitude lower number densities for the hybrid mode.

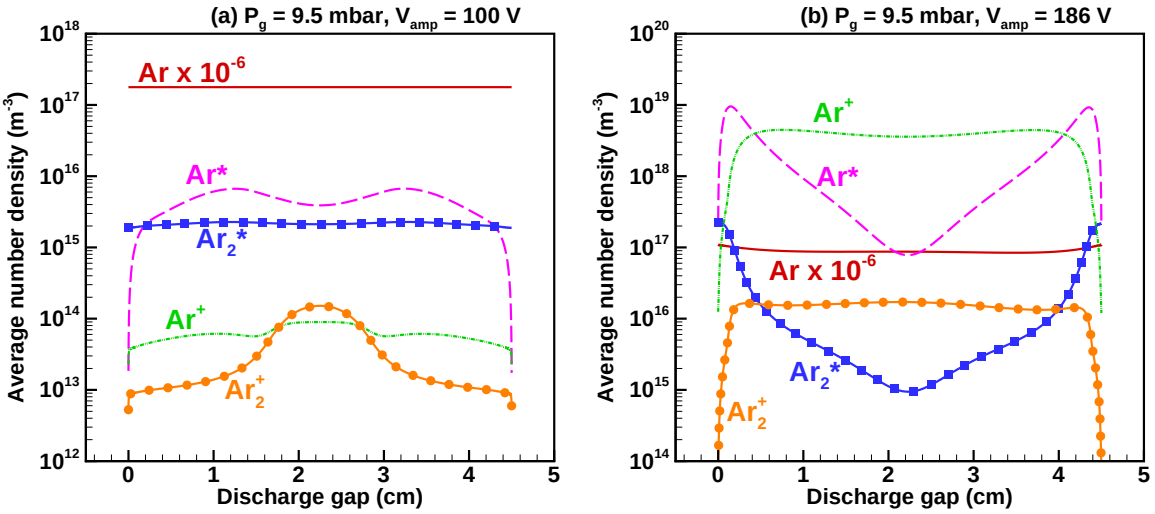

Figure 2.9. Ion and neutral species number density profiles at 9.5 mbar.

Figure 2.10 (a) compares the powers at the electrode modeled according to Eq. 2.1 for each of the conditions with the experimentally measured values. Experiments are not performed at voltage amplitudes below 145 V. The experimental power at the electrode is almost independent of the pressure for similar input voltage amplitudes. However, the computational power at the electrode increases significantly with pressure due to increase in the electron temperature which leads to greater current density. The average deviation from experimental measurements is 36% at 5.5 mbar, 7% at 9.5 mbar, and 74% at 13.8 mbar. Since the secondary electron emission coefficient is

used as a calibration parameter for 9.5 mbar case, the deviation from experiments is larger at other pressures.

Figure 2.10 (b) compares the experimentally measured H_2 rotational temperature and computational gas temperature at 2.6 cm from the left electrode. Experimental measurements are not available at low input voltages and pressures owing to the weak H_2 signal. The gas temperature variation with set power or voltage and pressure exhibits a similar trend for experiments and simulations. The simulated temperatures are higher than experimental values by 22.5% on average. This is due to the presence of molecular species such as H_2 and hydrocarbons as gas residue in the chamber which modify the plasma and heat transfer characteristics, and are not accounted for in the model. Such a deviation is in agreement with earlier work [120] which demonstrated that the presence of molecular impurities strongly influences the $\alpha - \gamma$ transition voltage and plasma characteristics.

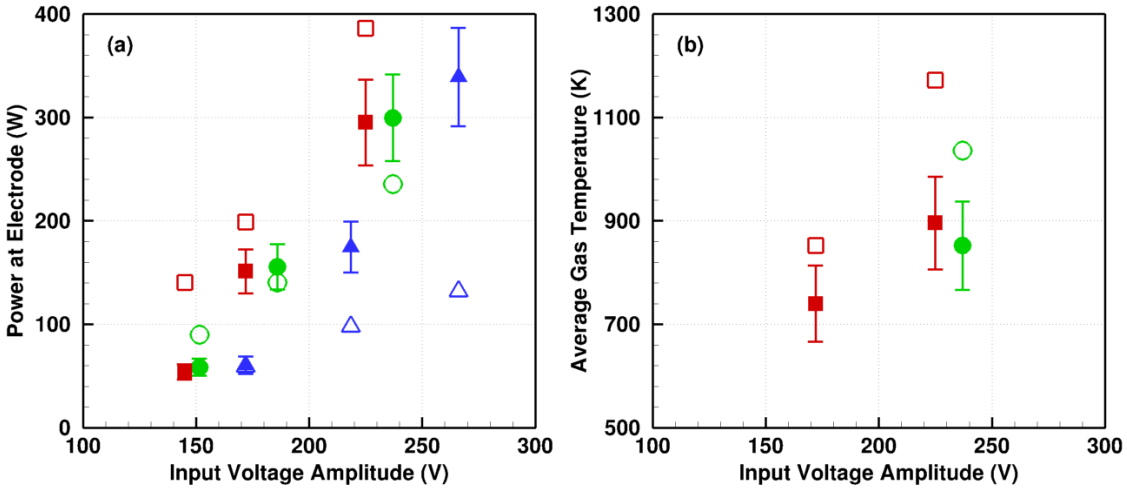

Figure 2.10. Comparison of computational (empty symbols) (a) power at the electrode and (b) average gas temperature in the discharge to experimental measurements (filled in symbols) at 5.5 mbar (blue triangles), 9.5 mbar (green circles) and 13.8 mbar (red squares) for $\gamma = 0.02$. Experimental measurements provided by Dr. Majed Alrefae from Prof. Timothy Fisher's research group.

2.3 Effect of Frequency and Waveform

This section explores the effect of three input properties, namely cycle frequency, rise frequency, and waveform, on the plasma characteristics. Figure 2.11 (a) presents the experimentally measured 80 kHz square voltage waveform at the electrode for $V_{amp} = 151.5$ V at 9.5 mbar. In order to investigate the main frequency components of the square voltage waveform measured experimentally, Fast Fourier Transform (FFT) analysis is performed. Figure 2.11 (b) presents the amplitudes of the square waveform with higher order components till the 9^{th} frequency (i.e., 720 kHz) at $V_{amp} = 151.5$ V and $P_g = 9.5$ mbar. The ratios of the amplitude at the frequencies $3f$, $5f$, $7f$, and $9f$ to that at the main frequency, $f = 80$ kHz, are 31.6%, 16.0%, 8.5%, and 3.81%, respectively. The presence of these high frequency components contributes to the existence of the α and hybrid modes for an 80 kHz square wave input. Figure 2.11 (a) also shows the averaged waveform used as an input for the simulations. The cycle frequency $f_{cycle} = 80$ kHz and the rise frequency $f_{rise} = 800$ kHz, which is 10 times the cycle frequency. It is significant to note that the rise and fall frequencies used have the same value for the square waveform.

Figure 2.12 shows the effect of the rise frequency for an 80 kHz cycle frequency voltage input on the plasma properties at $V_{amp} = 151.5$ V and $P_g = 9.5$ mbar. For the square wave input, as the rise frequency increases, the duration for which the high voltage lasts extends for a longer time, allowing more ionization in the discharge gap, thereby leading to higher electron density, sheath electron temperature, and gas temperature. This high voltage lasts for the lowest duration in the case of a sine wave input, thus leading to the lowest plasma properties for this case. Figure 2.13 shows the maximum contribution of displacement current to the total current in the sheath for these conditions. The discharge, which operates under hybrid mode at $f_{rise} = 800$ kHz, transitions to the γ mode when the f_{rise} decreases to 200 kHz because the maximum contribution of the displacement current decreases from 72% to 32% of the total sheath current. For a sine wave input, the maximum contribution is

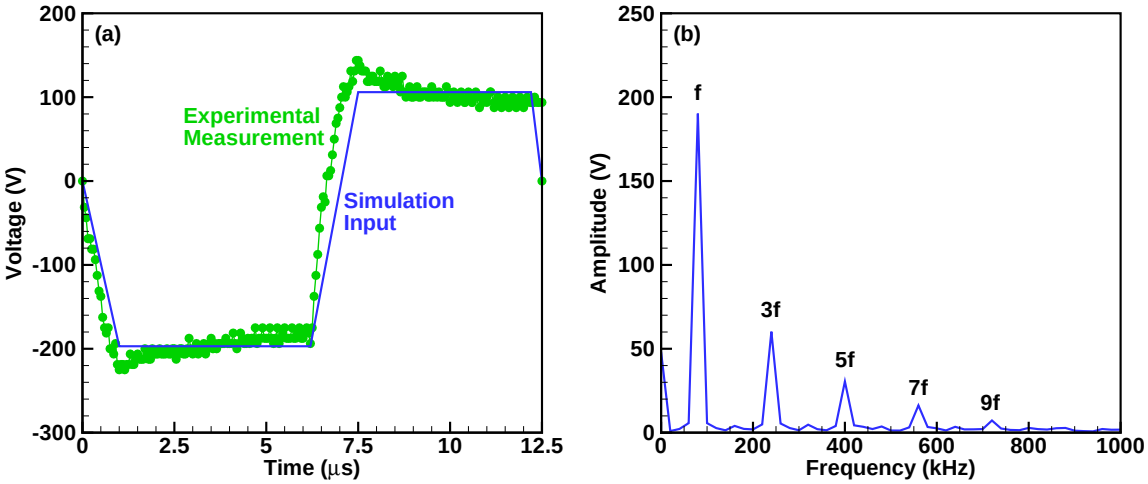

Figure 2.11. (a) Experimentally measured voltage waveform and averaged voltage input for simulations and (b) FFT analysis results on the measured waveform for V_{amp} = 151.5 V and f_{cycle} = 80 kHz at 9.5 mbar. Experimental measurements and FFT analysis performed by Dr. Majed Alrefae from Prof. Timothy Fisher's research group.

30% indicating a γ discharge. The displacement current also has a small contribution at every time instant in this case due to the continuously varying voltage input. The transition from hybrid to γ occurs between rise frequency values of 400 kHz to 200 kHz for an 80 kHz cycle frequency square wave input at 9.5 mbar. Moreover, for the conditions where the discharge operates in the γ mode at 151.5 V, a steady state discharge is not sustained at lower voltage inputs of 100 V and 125 V, indicating that a sharp rise of at least 400 kHz is required to sustain the α and hybrid modes.

Figure 2.14 shows the effect of cycle frequency and waveform type at V_{amp} = 151.5 V and P_g = 9.5 mbar when the rise frequency is maintained at 800 kHz. When the cycle frequency is reduced from 80 kHz to 5 kHz, the electron density increases in magnitude by a factor of 3 because the high voltage lasts for a longer time duration. The electron temperature shows the same peak magnitude in the sheath region due to the electric field magnitude being the same. However, in the center of the discharge, the electron temperature reduces with the cycle frequency on account of the discharge

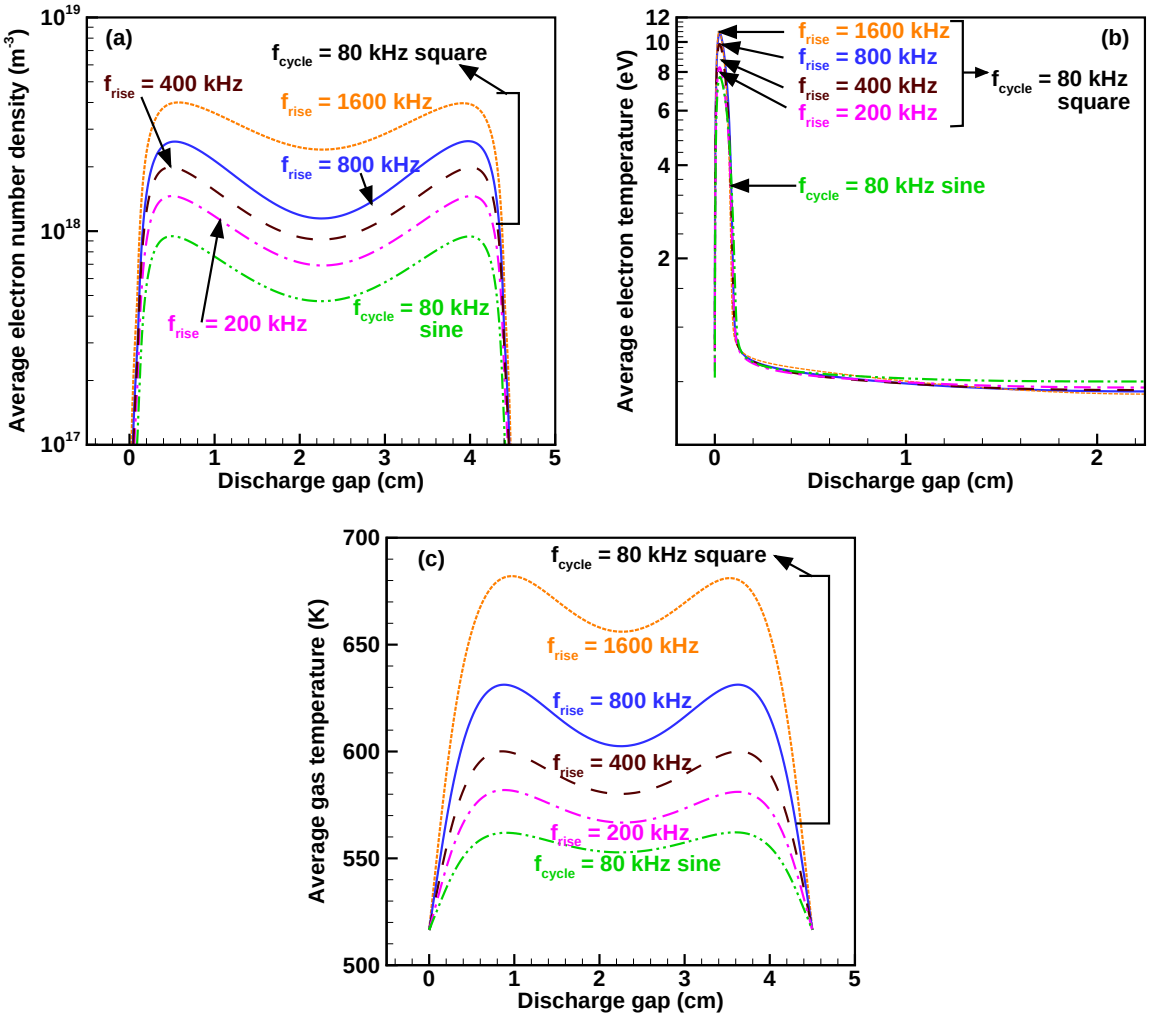

Figure 2.12. Variation of plasma properties with rise frequency and waveform for V_{amp} = 151.5 V and f_{cycle} = 80 kHz at 9.5 mbar. Electron temperatures in (b) are shown for half the discharge gap.

operating in the γ mode rather than a hybrid mode. The maximum contribution of the displacement current to the total sheath current as seen in Figure 2.15 is only 15% when the cycle frequency is 5 kHz. This indicates that although the square wave input has a high rise frequency, the total cycle frequency also plays a role in determining the type of discharge that is sustained. In the present system, the transition

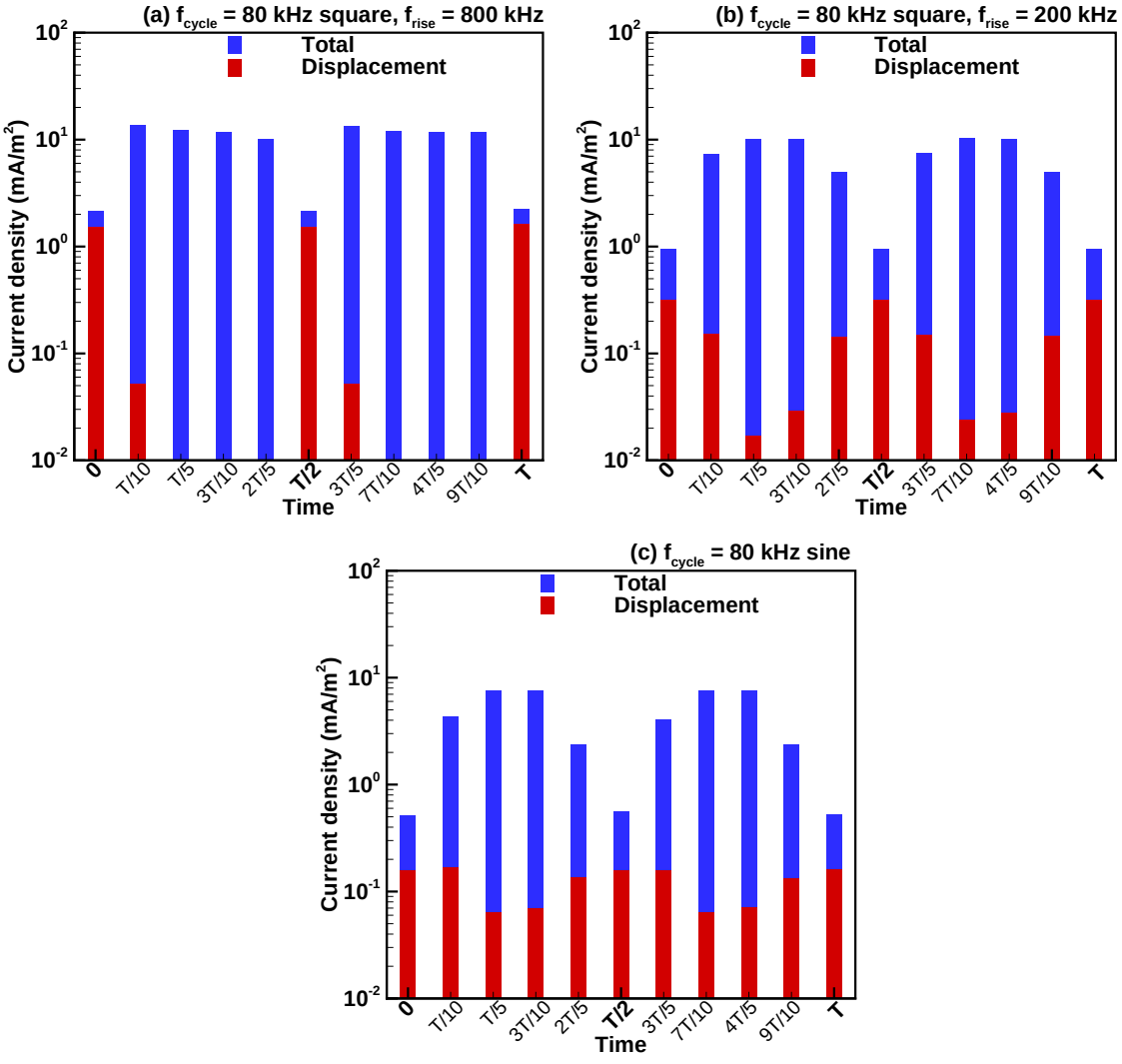

Figure 2.13. Effect of rise frequency on the maximum contribution of displacement current to the total current in the sheath for $V_{amp} = 151.5$ V and $f_{cycle} = 80$ kHz at 9.5 mbar.

from hybrid to γ modes occurs between cycle frequencies of 5 kHz and 40 kHz when the rise frequency is maintained at 800 kHz at 9.5 mbar.

When a sawtooth waveform with $f_{cycle} = 80$ kHz, $f_{rise} = 800$ kHz, $V_{amp} = 151.5$ V at 9.5 mbar is used, the plasma properties have lower values than those for a square wave due to the high voltage duration having the lowest value for a sawtooth wave.

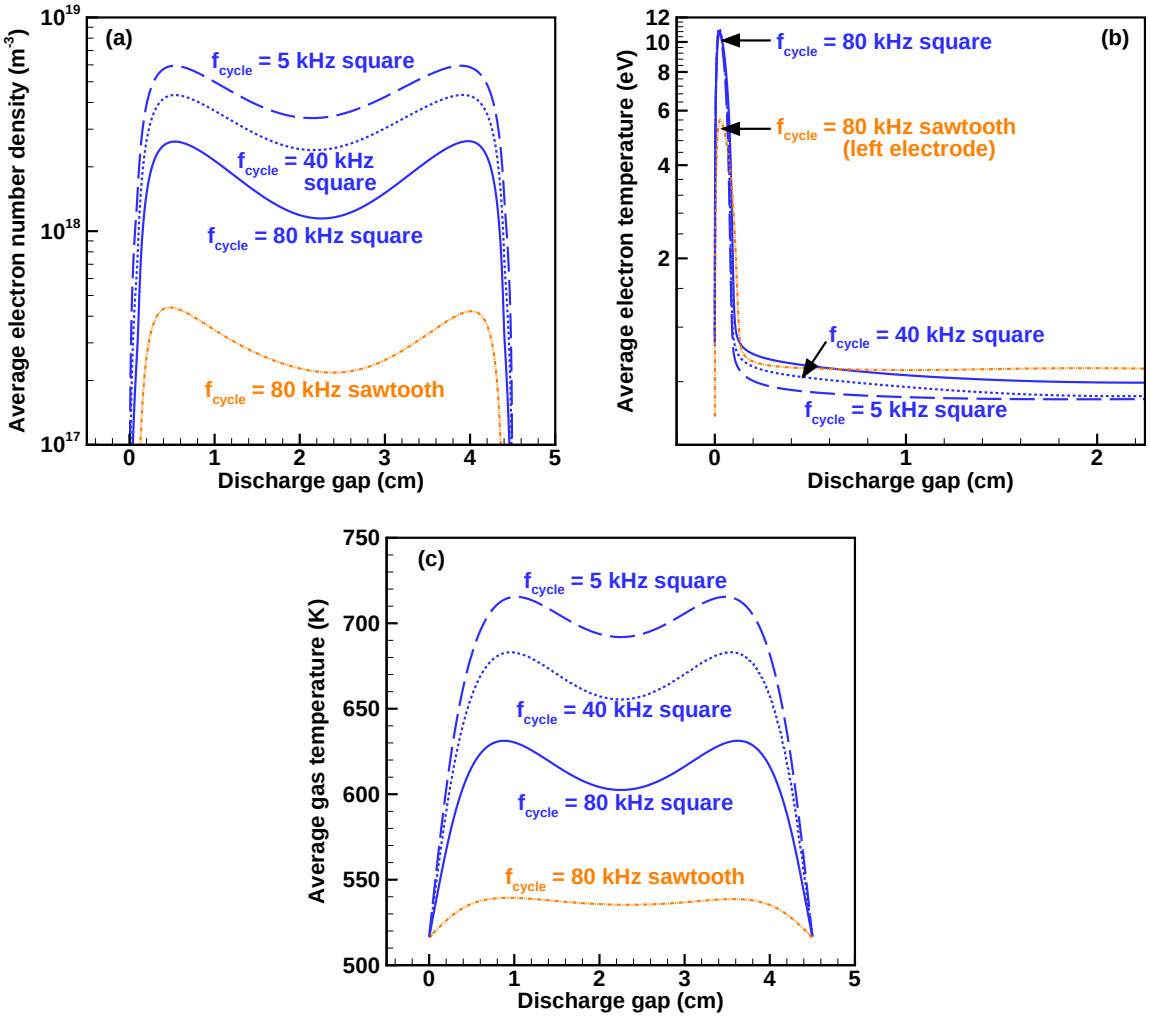

Figure 2.14. Variation of plasma properties with cycle frequency and waveform for V_{amp} = 151.5 V and f_{rise} = 800 kHz at 9.5 mbar. Electron temperatures in (b) are shown for half the discharge gap.

The profiles display asymmetry with higher electron density and temperature closer to the left electrode which has a quicker rise time than the right electrode which has a quicker fall time. This is because the sheath expands quicker when the rise time is shorter, imparting greater energy to the electrons, and increasing the ionization [121]. The asymmetry might be of significance while designing future RFCVD systems where the growth substrate is closer to one electrode than the other. Due to the sharp

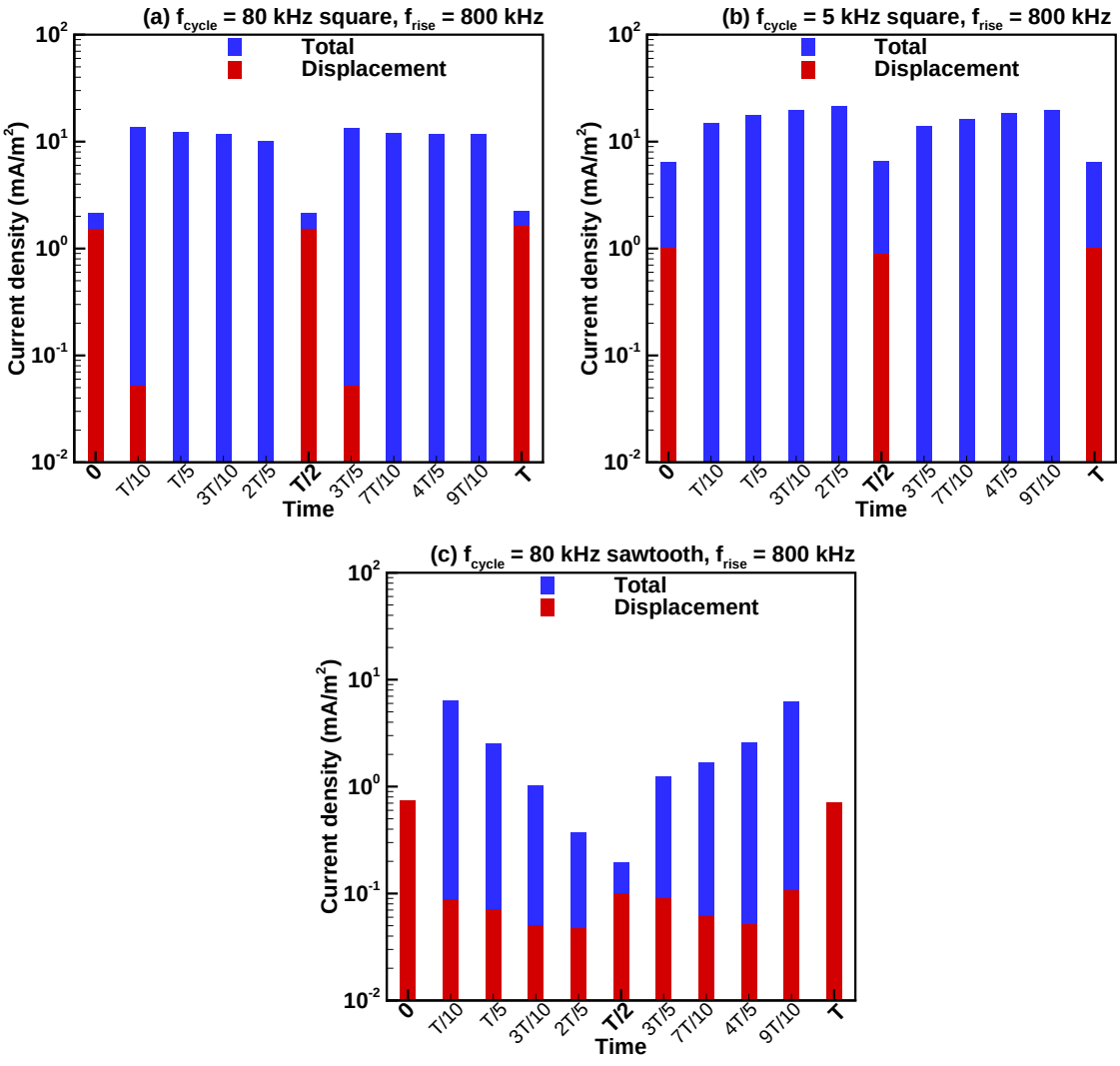

Figure 2.15. Effect of cycle frequency on the maximum contribution of displacement current to the total current in the sheath for V_{amp} = 151.5 V and f_{rise} = 800 kHz at 9.5 mbar.

rise and fall of voltage for a sawtooth wave, a hybrid mode is sustained as seen in Figure 2.15 (c), which shows the characteristics for the left electrode. At the instant when the voltage rises, the displacement current is responsible for 100% of all the current in the sheath. It also contributes 50% of the total current at the midpoint of

the fall duration. Once again, displacement current shows a small contribution to the total at every instant of time due to the continuously varying voltage in this case.

This work shows that the square waveform can sustain α and hybrid discharge modes at a lower cycle frequency than the sine waveform. Low frequency plasma systems have lower capital cost when compared to high frequency plasma systems [122, 123]. Furthermore, the uniformity of the deposition over a large area of the substrate becomes more attainable at lower frequencies. As a result, it is favorable to construct new RFCVD systems with low frequency square wave inputs, but the ion energy of these plasmas has to be controlled to avoid the degradation of the deposited carbon film [92].

2.4 Emission Intensities

OES measurements are performed to determine the emission intensities at different points in the discharge along the central axis with a position uncertainty of about 0.2 cm. The emission intensities from the CRM are compared to the measurements at three points in the discharge gap as shown in Figure 2.16: (1) at the left electrode (x = 0 cm), (2) 0.4 cm from the left electrode very close to the sheath region (x = 0.4 cm), and (3) 2.4 cm from the left electrode very close to the center point of the discharge (x = 2.4 cm). The simulation results shown in Figure 2.17 indicate good agreement with experimental OES measurements.

Very close to the electrode (x = 0 cm), the high concentration of energetic ions is expected to contribute significantly to the total emission. Since the Ar^+ and Ar_2^+ emission are not included in the CRM, the modeling results show least agreement with experiments at x = 0 cm. This is clearly seen in the 400 to 500 nm range which contains strong emission lines from Ar^+. 12 lines with high Einstein coefficients and significant deviation between modeling and experiments are indicated in Figure 2.17. Table 2.5 gives the wavelengths and optical transitions corresponding to these 12 lines. At the electrode, the model significantly overpredicts the intensities for lines

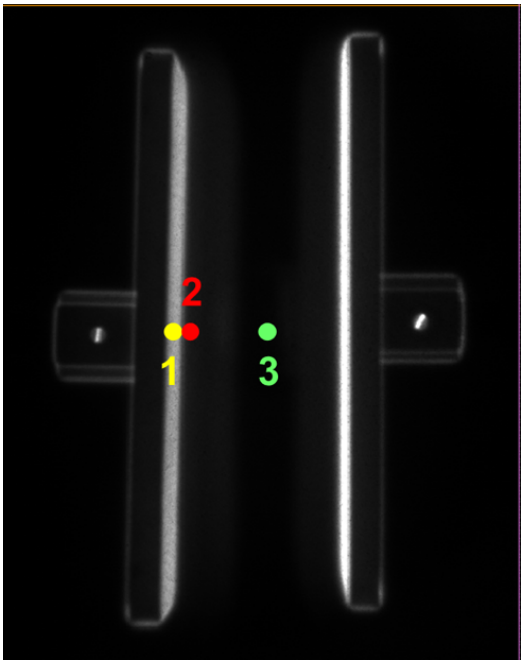

Figure 2.16. Locations in the discharge gap at which the emission intensities are modeled. Plasma image shown for V_{amp} = 186 V, P_g = 9.5 mbar, f_{cycle} = 80 kHz square wave input.

A to E and G and underpredicts the intensities for lines F, and H to L. The CRM shows maximum emission in the 700 to 820 nm range whereas OES shows maximum emission in the 820 to 870 nm range. The highest experimental peak is caused by the transition from state $2p4$ to $1s2$ and that for the CRM is caused by transition from state $2p6$ to $1s5$. The measurement also contributes to the deviation between OES and CRM because the plasma properties vary rapidly in the sheath region as seen in Figures 2.3 and 2.4. The position uncertainty of 0.2 cm is equal to the sheath thickness at this condition, and even a small deviation in the measurement location leads to significant variation in the plasma properties and therefore, the emission intensity profile.

As the location is moved away from the electrodes, the agreement between modeling and experiments improve. This is because energetic ions are absent in the center of the discharge gap and their emission is negligible compared to the atomic emission.

Also, in the center of the discharge, the plasma properties (especially the electron temperature) are relatively more uniform and thus, the uncertainty in the measurement location does not cause a significant deviation to the measured intensity profile. At x = 0.4 cm, lines A to C are underpredicted and lines D, I and K are overpredicted by the model. All the other lines show reasonable agreement with the OES data. At x = 2.4 cm, lines A, B, E, F, H, I and J are underpredicted by the model. Overall, the model tends to predict lower emission intensity at the center and higher at the electrode. The highest intensity is observed at 811.5 nm away from the electrode. This is caused by the spontaneous emission from state $2p9$ to $1s5$. The RSS errors are computed based on the relative intensities as given by Eq. 2.19. The values at x = 0 cm, 0.4 cm and 2.4 cm are 0.16, 0.10 and 0.07 respectively indicating an improvement in the modeling results as the distance between the point under consideration and the electrode increases.

Table 2.5. Wavelengths and argon energy levels associated with the emission lines indicated in Fig 2.17.

Line	**Wavelength [nm]**	**Transition**
A	750.4	$2p1 \rightarrow 1s2$
B	751.5	$2p5 \rightarrow 1s4$
C	763.5	$2p6 \rightarrow 1s5$
D	794.8	$2p4 \rightarrow 1s3$
E	801.5	$2p8 \rightarrow 1s5$
F	810.4	$2p7 \rightarrow 1s4$
G	811.5	$2p9 \rightarrow 1s5$
H	826.5	$2p2 \rightarrow 1s2$
I	840.8	$2p3 \rightarrow 1s2$
J	842.5	$2p8 \rightarrow 1s4$
K	852.1	$2p4 \rightarrow 1s2$
L	866.8	$2p7 \rightarrow 1s3$

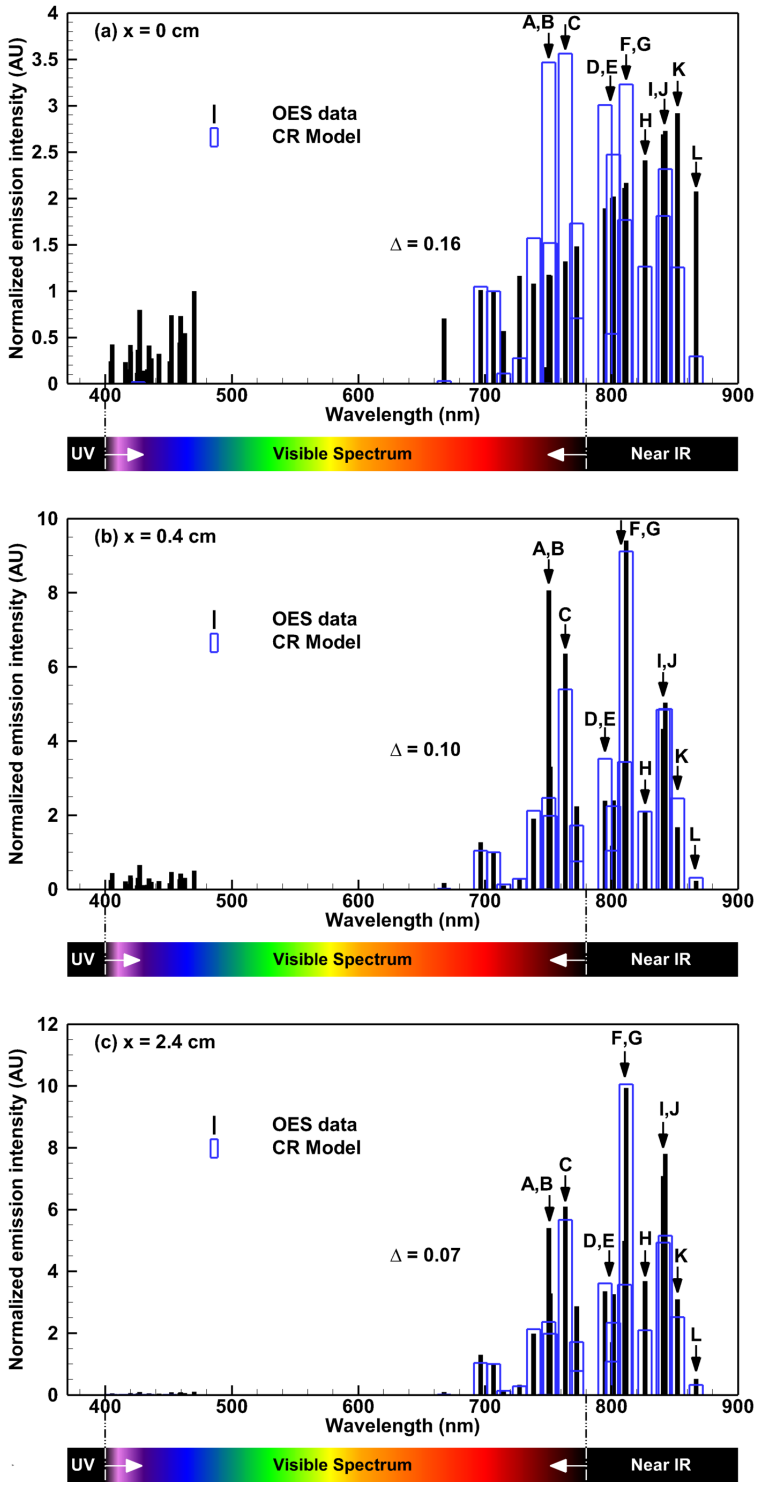

Figure 2.17. Comparison of emission intensity from the CRM with OES measurements in the 400 to 870 nm range for V_{amp} = 186 V, P_g = 9.5 mbar, f_{cycle} = 80 kHz square wave at x = (a) 0 cm, (b) 0.4 cm, and (c) 2.4 cm. OES measurements provided by Dr. Majed Alrefae from Prof. Timothy Fisher's research group.

3. HYDROGEN AND HYDROCARBON CHEMISTRY EFFECTS ON CCRF PLASMA PROPERTIES IN A R2R RFCVD SYSTEM

This chapter extends the 1D CCRF argon plasma model presented in Chapter 2 to hydrogen plasma in order to study the effect of gas composition on the plasma transition properties. The plasma properties from the 1D H_2 model are applied to a quasi-0D hydrocarbon chemistry model to determine the concentration of various hydrocarbon ions and neutrals during the deposition of carbon nanostructures using RFCVD.

3.1 Hydrogen Plasma Model

The simulation setup, 1D geometry and electrode dimensions used in the hydrogen plasma model are the same as those described in Section 2.1.1 for the argon plasma model. The DC bias, amplitude, and rise frequency of the 80 kHz cycle frequency square voltage waveform specified as inputs for the simulations correspond to experimentally measured values for pure hydrogen plasma at the same gas pressure and input power setting on the system. Since the effect of the gas pressure is known based on the argon plasma and this chapter focuses more on the chemistry effects, all the simulations are performed at a gas pressure of 9.5 mbar.

The electric field is determined using Poisson's equation given in Equation 2.2 and the electron number density and energy from the drift diffusion fluid model given by Equations 2.3 to 2.6. The energy source term consists of an additional energy gain component from the vibrational state, which is explained subsequently in this section. The particle balances for the neutral species and ions are determined based

on the modified Maxwell Stefan equations given by Equation 2.7. The gas phase hydrogen chemistry model used to determine the source terms is given in Table 3.1 which also indicates the references used to obtain the reaction rates or cross sections for the corresponding reactions. The diatomic nature of hydrogen results in a larger chemistry model consisting of 10 species and 31 reactions when compared to the monatomic argon. The rotationally excited levels are not modeled as separate species, but as a single H_2 molecule. The 3 vibrationally excited states of H_2 are modeled as a single vibrationally excited molecule. Only positive ions H^+, H_2^+ and H_3^+ are considered due to the electropositive nature of hydrogen plasma and based on previous work [124, 30, 125] which found the concentration of the H^- ion to be much lower in comparison to the positive ions.

The surface reactions modeled are the following:

$$H^+ \rightarrow H$$

$$H_2^+ \rightarrow H_2$$

$$H_3^+ \rightarrow H_2 + H$$

$$H(n = 2, 3, 4) \rightarrow H$$

The secondary electron emission is modeled as a boundary condition similar to the argon plasma model and the secondary electron emission coefficient, γ, is calibrated to match the power measured at the electrode at 9.5 mbar, V_{amp} = 209.5 V, and f_{rise} = 950 kHz. The cycle averaged power is calculated using Equation 2.1 and the variation of predicted electrode power with γ values is shown in Table 3.2. Since the modeled power at $\gamma = 0.028$ closely matches the experimental value of 263 W, this value is chosen as the input for all the cases modeled here.

The heat transfer solver for H_2 plasma solves the heat equation for two temperatures instead of a single gas temperature. The first is the temperature of the rotational and translational modes, T_g, which equilibrate fairly quickly [129] and the

Table 3.1. Gas phase reactions modeled for H_2 chemistry.

Reaction	**Chemical reaction**	**Reference**
Excitation	$e + H_2(j = 0, 1) \rightarrow e + H_2(j = 2, 3)$	[126]
Excitation	$e + H_2 \rightarrow e + H_2(v = 1, 2, 3)$	[126]
Ionization	$e + H_2 \rightarrow 2e + H_2^+$	[126]
Dissociation	$e + H_2 \rightarrow e + 2H$	[127]
Excitation	$e + H \rightarrow e + H(n = 2, 3, 4)$	[127]
Dissociative excitation	$e + H_2 \rightarrow e + H + H(n = 2, 3)$	[127]
Ionization	$e + H \rightarrow 2e + H^+$	[128]
Recombination	$e + H^+ \rightarrow H(n = 2, 3, 4)$	[127]
Dissociative recombination	$e + H_2^+ \rightarrow H + H(n = 2, 3, 4)$	[127]
Dissociative recombination	$e + H_3^+ \rightarrow 3H$	[127]
Dissociative recombination	$e + H_3^+ \rightarrow H_2 + H(n = 2)$	[127]
Dissociation	$2H_2 \rightarrow 2H + H_2$	[124]
Dissociation	$H_2 + H \rightarrow 3H$	[124]
Association	$2H + H_2 \rightarrow 2H_2$	[124]
Association	$3H \rightarrow H_2 + H$	[124]
Ionization	$H(n = 2, 3, 4) + H_2 \rightarrow H_3^+ + e$	[124]
Ion conversion	$H_2 + H_2^+ \rightarrow H_3^+ + H$	[124]
Relaxation	$H(n = 3, 4) \rightarrow H(n = 2)$	[115]

temperature of the vibrational mode, T_v. The ions are also modeled at T_g, which is determined by solving the following equation:

$$k_g \frac{\partial^2 T_g}{\partial x^2} + Q_g - Q_{conv} + Q_{vT} = 0 \tag{3.1}$$

where, the thermal conductivity of the translational and rotational modes, k_g, is determined based on the expressions given by Lee [130] derived from the Chapman-

Table 3.2. Variation of computational electrode power with secondary electron emission coefficient for H_2 plasma at P_g = 9.5 mbar and V_{amp} = 209.5 V. The experimental power at the electrode is 263 W.

γ	P_{el} [W]
0.025	216.6
0.028	264.7
0.035	391.5

Enskog approximation [131]. The variation of the total thermal conductivity of all states of H_2, k_{H_2} is obtained from the NIST database [132] and is used to determine k_g as:

$$k_g = \frac{15k_{H_2}}{4}\left(1+\frac{4}{15}\right)\frac{k_B}{m_{H_2}} \tag{3.2}$$

where, m_{H_2} is the mass of a hydrogen molecule. The energy transferred from the electrons to the gas during collisions, Q_g, is modeled similar to the argon plasma model. The fractional energy loss in this case accounts for inelastic collisions in addition to the elastic energy transfer due to the diatomic nature of hydrogen. The heat loss due to free convection is modeled similarly to argon and the same convective heat transfer coefficient is assumed. The electrode temperature used as the boundary condition is assumed to be independent of the gas composition [110] and the same values as the argon plasma are used under similar input power settings on the system.

The energy transfer from the vibrational mode to the translational mode, Q_{vT}, is modeled based on the work of Scott *et al.* [129]. The energy transfer rate is given by:

$$Q_{vT} = (e_v - e_v^*(T_g))\left(\frac{1}{\tau_{v_{H_2}}}+\frac{1}{\tau_{v_H}}\right) \tag{3.3}$$

where, $e_v^*(T_g)$ is the equilibrium vibrational energy per unit volume at the translational temperature [130], e_v is the vibrational energy of the flow per unit volume, $\tau_{v_{H_2}}$ is the vibrational-translational relaxation time for collisions of H_2 with H_2, and τ_{v_H} is

the relaxation time for collisions of H_2 with H. The relaxation time, τ_{v_H} is calculated based on the Arrhenius quenching rates for reactive and non-reactive collisions, k_r and k_{nr}, respectively [129, 133] as:

$$\tau_{v_H} = \frac{1}{n_H \left(k_{nr} + k_r\right)} \tag{3.4}$$

where n_H is the number density of H atoms. The Landau-Teller relaxation time for H_2-H_2 collisions based on the Kiefer and Lutz correlations [134] is given by [129]:

$$\tau_{v_{H_2}} = 4.16 \times 10^{-8} \exp\left(\frac{100}{\sqrt[3]{T_g}}\right)[s] \tag{3.5}$$

at a pressure of 9.5 mbar.

The temperature of the vibrational mode is determined by solving the energy conservation as given by:

$$k_v \frac{\partial^2 T_v}{\partial x^2} + Q_{ev} - Q_{vT} = 0 \tag{3.6}$$

where, the vibrational component of the thermal conductivity is given by $k_v = k_{H_2} - k_g$. The energy transferred from the electron and the vibrational mode, Q_{ev}, occurs due to direct excitation from the ground state as well as due to vibrational excitation via electronic excitation of excited singlet states followed by a subsequent radiative transition to a vibrationally excited ground state. The direct excitation from the ground state is modeled to the first three vibrational levels as given in Table 3.1 and the energy transfer is determined based on the S_ϵ term corresponding to these reactions in the drift diffusion model. The energy lost by the electrons in exciting the two singlet states $B^1\Sigma$ and $C^1\Pi$ is given by:

$$Q_{el} = -n_e n_{H_2} \left(k_{ev}^B \epsilon_B + k_{ev}^C \epsilon_C\right) \tag{3.7}$$

where, the reaction rates, k_{ev}^B and k_{ev}^C, as well as the threshold energies per mole, ϵ_B and ϵ_C, are taken from [129]. This term is included as a sink in S_ϵ in the drift diffusion equations. The energy gained by the vibrational mode due to excitaiton from these singlet states is given by [129]:

$$Q_{ev_{singlet}} = n_{H_2} n_e R_u \theta_v \left(k_{ev}^B S_B + k_{ev}^C S_C\right) \tag{3.8}$$

where, R_u is the universal gas constant, θ_v is the characteristic vibrational temperature, and the vibrational excitation probability of the singlet states, S_B and S_C, are taken from [129]. The vibrational temperature at the boundary is assumed to be 3000 K. The plasma and heat transfer solvers are coupled to each other and solved similarly to the argon model till deviations of gas and vibrational temperatures of $<5\%$ from the previous iteration are achieved.

Hydrogen is a diatomic species and building a collision radiative model involves a large number of non-linear rate equations including electronic, vibrational, and rotational excitation, transitions, dissociation, and ionization reactions. Due to the difficulty associated with obtaining cross sectional data for all the reactions involved, a simpler method is used to compare the emission intensity for hydrogen plasma similar to that used by Iordanova *et al* [135]. The atomic spectrum of hydrogen shows two distinct transitions from the $n = 3$ to $n = 2$ and from $n = 4$ to $n = 2$. These two lines are called the H_α line and the H_β line at wavelengths of 656.28 nm and 486.13 nm, respectively. In order to validate the simulated composition of the species and plasma properties, the ratio of the H_α line intensity to the H_β line intensity is compared to experimental measurements. This ratio can be determined based on the simulated plasma properties as:

$$\frac{I_{H_\alpha}}{I_{H_\beta}} = \frac{n_{H(n=3)} A_\alpha \Lambda_\alpha / \lambda_\alpha}{n_{H(n=4)} A_\beta \Lambda_\beta / \lambda_\beta} \tag{3.9}$$

where, the Einstein coefficients for the lines are obtained from the NIST database [115], the number densities of the electronically excited hydrogen atoms are obtained from the plasma model, and the escape factors are determined similar to the argon CRM.

3.2 Effect of Gas Composition on CCRF Plasma Transition Characteristics

This section presents the results of the hydrogen plasma model averaged over 10 steady state cycles. The input voltage in all these cases has a square waveform with a cycle frequency of 80 kHz and rise frequency of $\sim$950 kHz at a pure hydrogen gas

pressure of 9.5 mbar. Figure 3.1 shows the variation of plasma properties with the input voltage amplitude. The electron number density shows a sharp jump in its magnitude similar to the argon plasma case when more energy is imparted into the system. This jump occurs when the voltage amplitude increases from 175 V to 180 V. This is higher than the transition voltage between 105 V and 110 V for argon at the same pressure. The higher α to hybrid transition voltage in the case of the hydrogen discharge is expected based on Paschen's law [49]. The minimum point of the Paschen's curve, termed as Stoletov's point [37], occurs at a higher voltage for hydrogen when compared to argon. Based on the results of the argon plasma, the transition occurs at this minimum point. The voltage at the minimum point is determined by the ionization potential of the gas, the mean free path for electron-neutral collisions, and the transfer of energy from the electrons to the neutral gas. The ionization potentials of argon and hydrogen have comparable values of 15.4 eV and 15.8 eV, respectively. The mean free path for argon and hydrogen at 9.5 mbar are 42.1 μm and 28.1 μm respectively [37] indicating earlier breakdown for hydrogen. However, the major disparity occurs due to the diatomic nature of hydrogen which leads to a loss of electron energy to the rotational and vibrational modes. Thus, more input energy is required for the ionization avalanche in the sheath to reach high enough values for transition to occur. This higher transition voltage for hydrogen is corroborated by experimental observations [136].

Another deviation in the electron number density profiles is the lack of a pronounced two peak structure in the case of hydrogen plasma at the same gas pressure. The number density also does not increase much when the input voltage amplitude is increased beyond 209.5 V. The electron temperature profiles shown in Figure 3.1 (b) display an increase in value in the sheath region during transition and decrease by a factor of 2 in the center of the discharge similar to the argon cases. The gas temperature increases with voltage amplitude due to an increase in the electron number density, but the α case for hydrogen plasma shows spatial variation in contrast to the argon plasma which shows a constant profile throughout the discharge. In the

case of argon, the gas heating occurs due to energy transfer from the electrons. Low electron density for the α case leads to a small source term, Q_g. However, for hydrogen plasma, the gas not only gains energy from the electrons, but also from the vibrational mode. This source term, Q_{vT}, has a contribution even in the α mode because it does not depend on the electron number density, leading to gas heating. However, the increase in Q_g beyond the transition leads to higher gas temperature values at higher voltages.

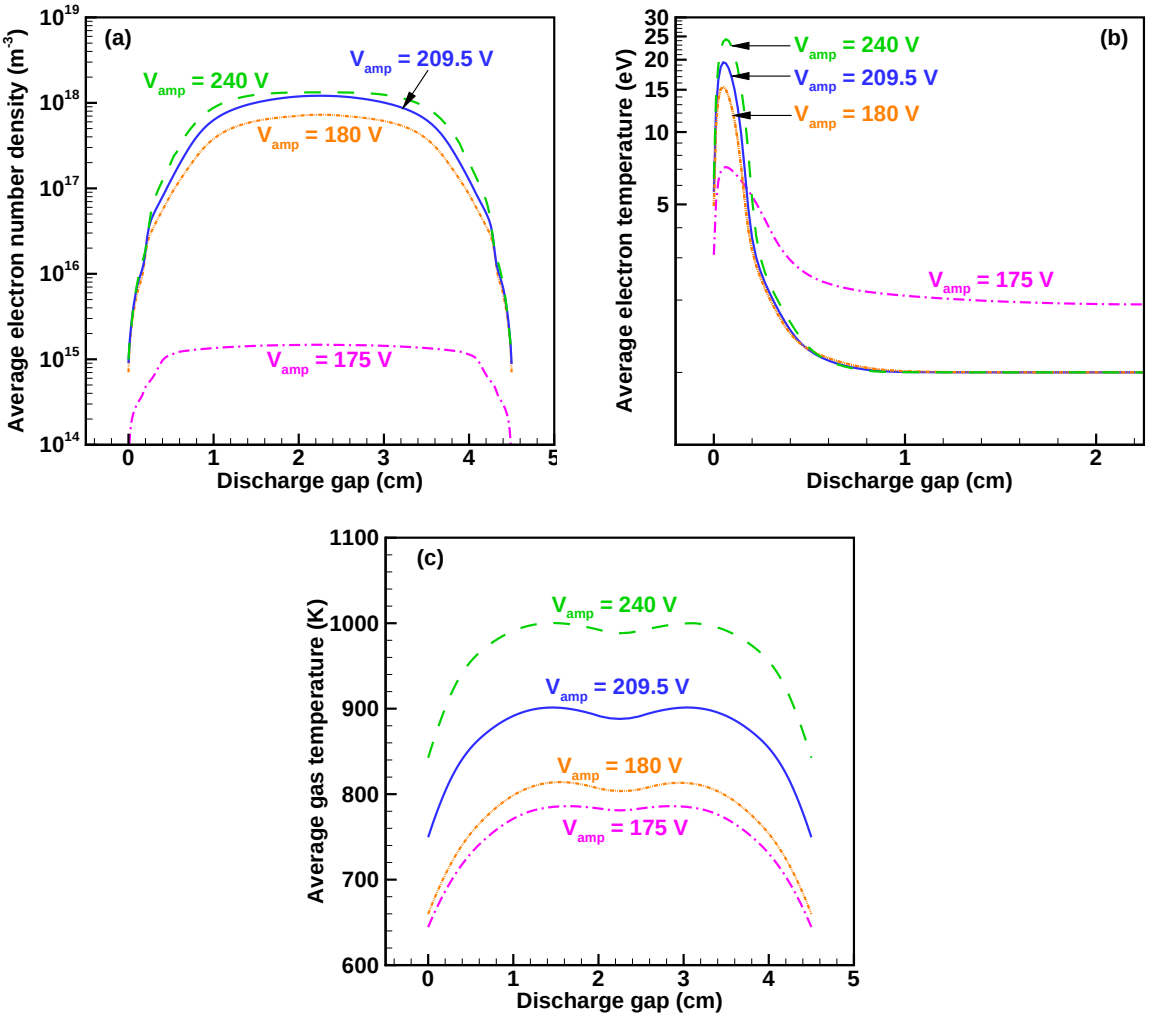

Figure 3.1. Variation of hydrogen plasma properties with voltage amplitude at 9.5 mbar. Electron temperatures in (b) are shown for half the discharge gap.

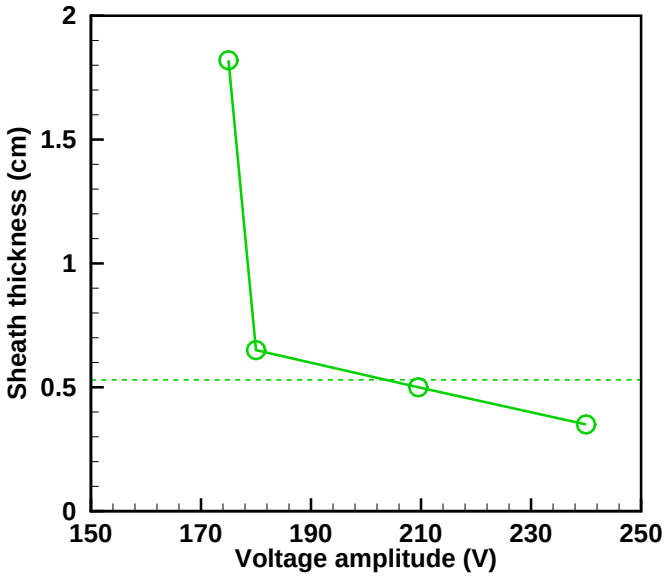

Figure 3.2. Variation of sheath thickness with voltage amplitude for hydrogen plasma. The dotted line shows the Paschen minimum at 9.5 mbar.

The variation of the sheath thickness with the voltage amplitude is shown in Figure 3.2. The behavior is similar to that of the argon plasma. The sheath thickness drops to a value close to the Paschen minimum corresponding to the same pressure during the α to hybrid transition and stays relatively constant beyond transition. This transition is also displayed by the sheath current density profiles shown in Figure 3.3. The α mode at V_{amp} = 175 V shows high current density in the sheath when the sharp transition of the square wave occurs. The sheath is also non-conducting during the transition. When the discharge transitions to the hybrid mode at V_{amp} = 209.5 V, the current density during the constant input voltage region becomes higher than that during the voltage drop or rise. However, during this rise/fall, the displacement current shows a maximum contribution of 100% to the sheath current. At V_{amp} = 240 V, the discharge transitions to the γ mode where the contribution of the displacement current to the sheath current reduces to less than 20% even during the voltage rise/fall. Thus, the phenomena observed are similar to those for the argon

discharge, but the voltages at which the transitions occur are higher in the case of hydrogen due to the inelastic energy loss from the electrons.

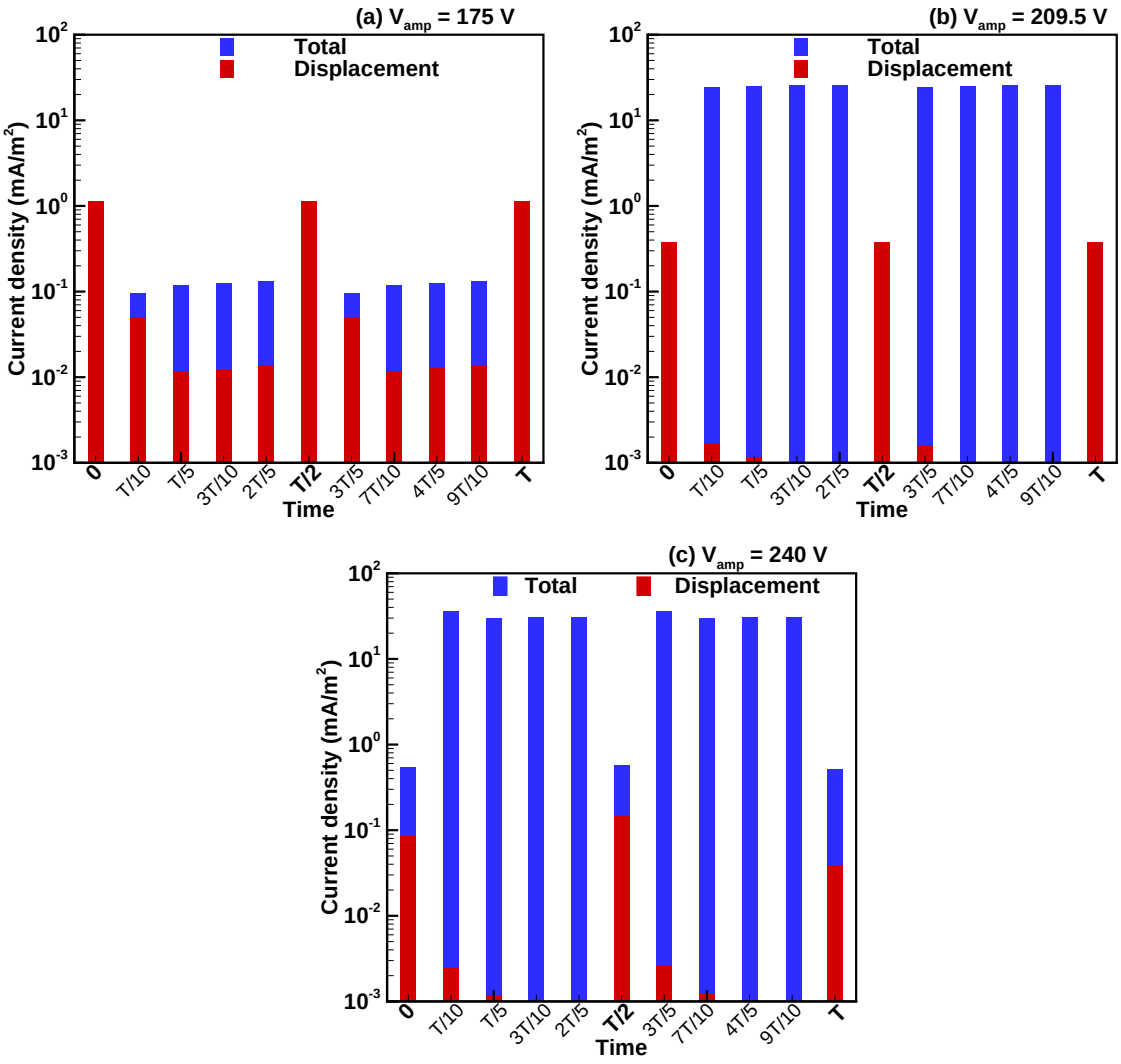

Figure 3.3. Maximum contribution of displacement current to the total current in the sheath at 9.5 mbar.

Figure 3.4 shows the ion and neutral species number densities for the α and hybrid discharges. The profiles for the γ mode are similar to the hybrid case. The dominant species in both cases are H_2 and H. Among the electronically excited states of H, the state with $n = 2$ has an order of magnitude higher density when compared to

states with $n = 3, 4$. For the α mode, H_3^+ is the dominant ionic species, whereas for the hybrid mode, H^+ is the dominant ion in the center of the discharge and H_3^+ dominates in the sheath region near the electrodes. In both cases, H_2^+ has at least 5 orders of magnitude lower density when compared to the other ions in the center of the discharge. This is in agreement with previously published experimental results for hydrogen microwave plasmas [124,125]. In the hybrid case, the density of H_2^+ is lower than in the α case because the higher electron number density leads to a high rate of dissociative recombination which increases the number density of the electronically excited H atoms.

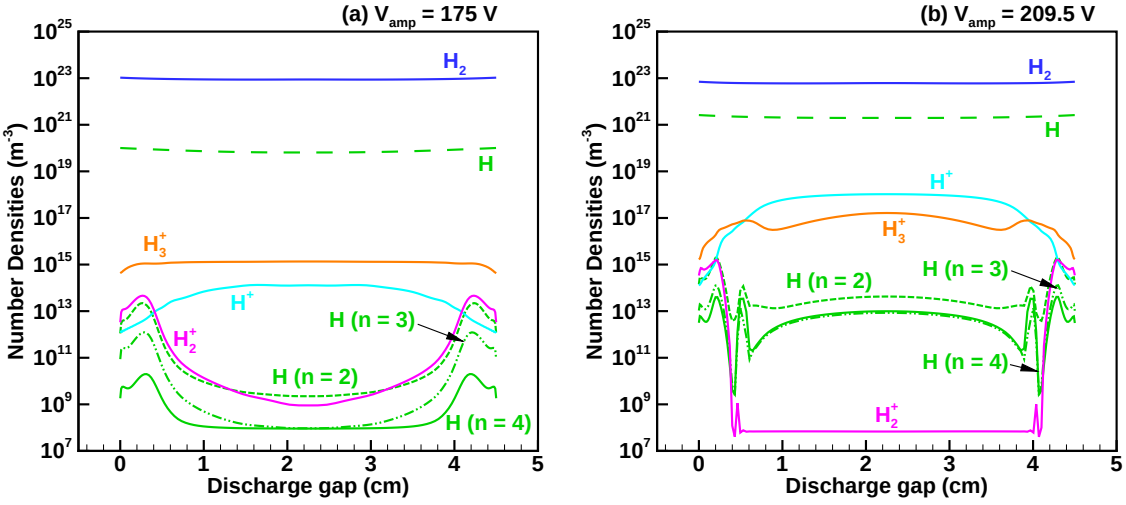

Figure 3.4. Hydrogen ion and neutral species number density profiles at 9.5 mbar.

3.3 Comparison of Modeling Results and Experimental Measurements

This section compares the results of the hydrogen plasma model with experimental measurements. The validation of the argon plasma model is presented in Chapter 2. The modifications to the model are in the form of chemistry and heat transfer and they need to be compared to hydrogen plasma experimental measurements. Experi-

mental measurements of voltage waveform under different input power setpoints and gas pressures are required as inputs for the simulations. The properties output by the simulations that can be compared to experimental measurements are the gas temperature (rotational temperature measured) and emission intensities. However, the input voltage waveform and output temperature and emission intensity profiles are not available under the same conditions for hydrogen plasma in [136].

The voltage waveform is available at 9.5 mbar pressure and 900 W input power setting on the system. This corresponds to the V_{amp} = 209.5 V case presented in the preceding section. This is for symmetric electrode configuration with electrodes of area 62.5 cm^2, which is reduced to a 1D case for the simulations. However, the gas temperature measurements are only available for an asymmetric electrode configuration, with a larger left electrode of area 136 cm^2. The measurements are at a location of 4.13 cm from the left electrode and are compared to the simulated value at the same location. The difference in input voltage and current for pure hydrogen plasma with symmetric and asymmetric electrode configurations are shown in Figure 3.5. The cases at 900 W input power are indicated at 9.5 mbar by the grey markers and do not deviate much from one another. Thus, it is assumed that the plasma properties for the two cases are comparable.

The experimentally measured rotational temperatures of H_2 are available at a pressure of 9 mbar and not at 9.5 mbar. Figure 3.6 (a) shows a weak dependence of the rotational temperature on the gas pressure and thus, the two can be compared. The measurements are available for 95% H_2, 5% N_2 plasma at 900 W input power and for the 100% H_2 plasma at 1000 W input power. Figure 3.6 (b) shows that the H_2 rotational temperature increases with decreasing H_2 concentration and increasing N_2 concentration. Thus, the simulated gas temperature for 100% H_2 plasma is expected to be lower than the value for the 95% H_2, 5% N_2 plasma. This trend of the gas temperature with the nitrogen concentration can also be seen in Figure 3.7 at 1000 W input power. The gas temperature at 900 W is also expected to be slightly lower than the gas temperature at 1000 W for 100% H_2 plasma due to lower energy input into the

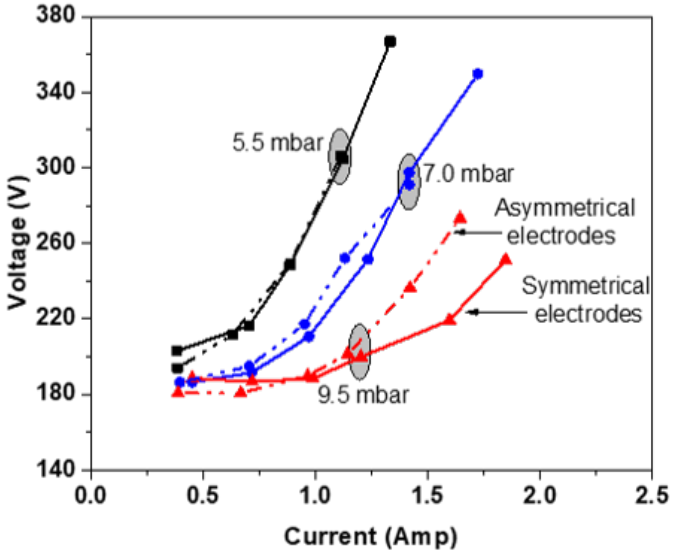

Figure 3.5. Comparison of experimentally measured voltage and current at the electrode for asymmetric and symmetric electrode configurations for pure H_2 plasma [136].

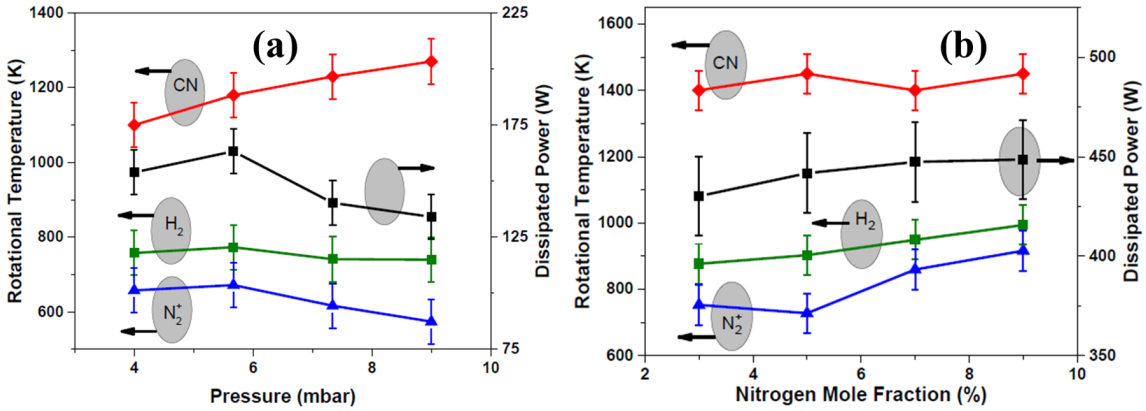

Figure 3.6. Variation of experimentally measured rotational temperature at 4 cm from the left electrode with (a) gas pressure at an input power setpoint of 500 W for 95% H_2, 5% N_2 mixture, and (b) nitrogen mole fraction at 9 mbar and input power setpoint of 1000 W [136].

system. These expected trends are displayed by the comparison shown in Figure 3.7

and the simulated gas temperature lies in the expected range based on experimental measurements.

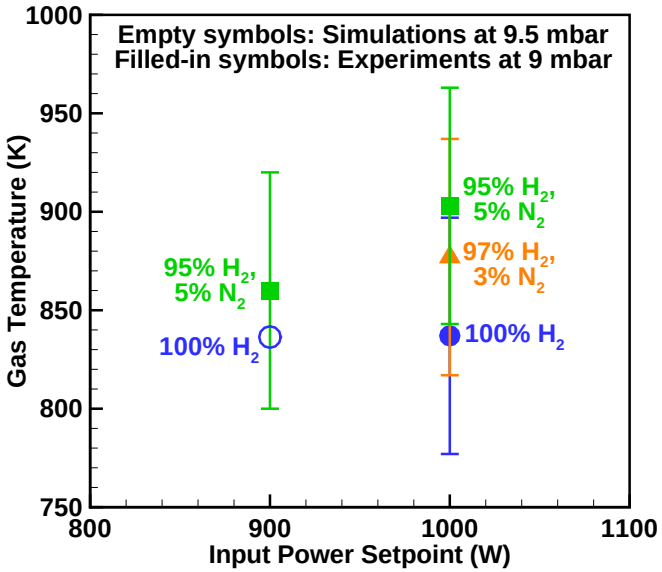

Figure 3.7. Comparison of computational and experimental gas temperatures at a location 4.13 cm from the left electrode. Experimental measurements provided by Dr. Majed Alrefae from Prof. Timothy Fisher's research group.

In addition to the gas temperature, the emission intensity ratios of the H_α line to the H_β line at different locations in the discharge, as described in Section 3.1, are also compared between the simulations and experiments. Since emission intensities are highly sensitive to the species present in the discharge, the cases compared are for 100% H_2 plasma. The experimental measurements are available at 9 mbar and input power setpoint of 1000 W and simulation results are available at 9.5 mbar and 900 W. Figure 3.8 shows that the emission intensity increases with input power and decreases with pressure. Consequently, the simulated conditions are expected to display lower emission intensities than the experimental conditions on account of lower input power and higher gas pressure. This is seen in Figure 3.9 which shows the experimental results and cycle-averaged simulation results as blue circles. Since the experimental

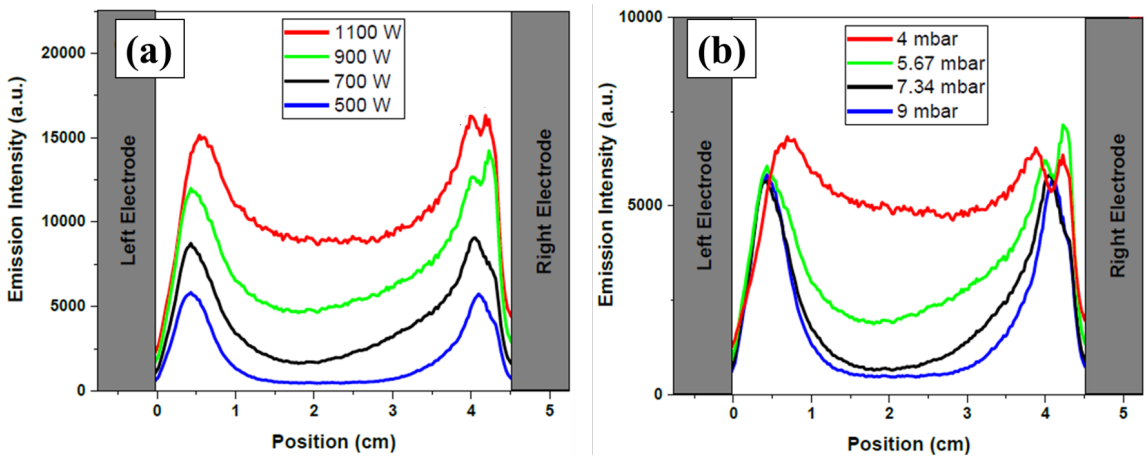

Figure 3.8. Variation of experimentally measured emission intensities for 95% H_2, 5% N_2 mixture with (a) input power setpoint at 9 mbar, and (b) gas pressure at input power setpoint of 500 W [136].

results are not averaged in time and since it is not possible to accurately determine the instant during the cycle at which the measurements are obtained, the variation of I_{H_α}/I_{H_β} at different instances during the cycle are shown as lines of different colors. The simulation results do not agree closely with experimental measurements and the deviation is attributed to the difference in the input conditions for the two cases. The presence of residual and electrode emitted hydrocarbon species in the chamber during experiments may also lead to a difference in the excited hydrogen concentration, contributing to the deviation between experimental and modeling results. The expected trends and qualitative variations based on experiments are displayed by the modeled emission intensities.

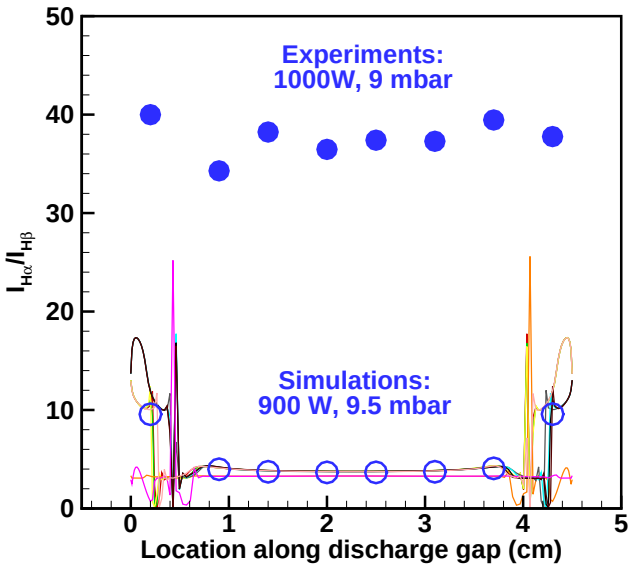

Figure 3.9. Comparison of computational and experimental ratio of emission intensities of the H_α and H_β lines. The lines show simulation results at different instances of time and open symbols show cycle-averaged simulation results. Experimental measurements provided by Dr. Majed Alrefae from Prof. Timothy Fisher's research group.

3.4 Hydrocarbon Chemistry

Although most of the graphene growth studies in the literature are largely empirical, recently some efforts have been made to understand the physiochemical mechanisms that govern the deposition of single layer graphene using CVD [137, 138]. In particular, 0D modeling and spectroscopy have been performed by Pashova *et al.* [139] to better understand the MPCVD of graphene. Along similar lines, this section presents the quasi-0D steady-state modeling of the hydrocarbon chemistry using hydrogen plasma properties to estimate various precursor concentrations, which can ultimately aid the prediction of carbon nanostructure growth rates. This method helps the identification of the key species responsible for the deposition process without significant computational demands. It is significant to note that this study only

provides the steady state concentrations of various species at the given plasma conditions and does not conserve the element concentrations over time.

Table 3.3. Ionic reactions modeled for hydrocarbon chemistry.

Chemical reaction	**Reference**
$CH_4^+ + CH_4 \rightarrow CH_5^+ + CH_3$	140
$CH_4^+ + H_2 \rightarrow CH_5^+ + H$	140
$C_2H_2^+ + CH_4 \rightarrow C_2H_3^+ + CH_3$	140
$C_2H_3^+ + C_2H_4 \rightarrow C_2H_5^+ + C_2H_2$	140
$H_3^+ + CH_4 \rightarrow CH_5^+ + H_2$	140
$H_3^+ + C_2H_2 \rightarrow C_2H_3^+ + H_2$	140
$H_3^+ + C_2H_4 \rightarrow C_2H_5^+ + H_2$	140
$CH_5^+ + C_2H_6 \rightarrow C_2H_5^+ + CH_4 + H_2$	141

The quasi-0D steady state model solves the species conservation equation at the conditions determined for pure hydrogen plasma in Section 3.2 at a specific location in the discharge gap. It is assumed that the electron number density, electron temperature and gas temperature are not affected by the introduction of small quantities of methane. These properties at various locations in the discharge gap under different conditions are kept constant while solving the steady state species conservation equation given by:

$$\frac{d\omega_i}{dt} = \frac{M_i S_i}{\rho} = 0 \tag{3.10}$$

where, ω_i is the mass fraction of species i, M_i is its molar mass, and ρ is the density of the mixture. The mass fraction stays constant under steady state which requires that the reaction rates balance each other in such a way that the source term, S, for every species has a net production rate of 0. The mass fraction is determined based on the molar concentration of the species, C, as $\omega_i = C_i M_i/\rho$. The total molar concentration is determined based on the pressure and temperature at the

location (which are known from the 1D hydrogen plasma modeling results) as $\sum_i C_i = P_g/R_u T_g$. 17 neutral species, 10 ionic species and electrons are used in the chemistry model based on the work of Lombardi *et al.* [142]. In addition to the hydrogen species and reactions included in Section 3.1, the carbon containing species modeled are CH_4, CH_3, $^3CH_2$, $^1CH_2$, CH, C, C_2H_6, C_2H_5, C_2H_4, C_2H_3, C_2H_2, C_2H, CH_5^+, CH_4^+, $C_2H_6^+$, $C_2H_5^+$, $C_2H_4^+$, $C_2H_3^+$, and $C_2H_2^+$. The GRI-Mech 3.0 reaction mechanism [143] with reactions involving species containing C and/or H is used for the neutrals. In addition, the ionic reactions and electron impact reactions given in Tables 3.3 and 3.4 are used for the charged species. Their corresponding references for reaction rates or cross sections also also provided in the tables. The neutral reactions are modeled as reversible reactions with the reverse rates calculated based on equilibrium constants determined from the thermodynamic properties. The charged species reactions are modeled as irreversible reactions. The thermodynamic properties of the neutrals are taken from [144] and those of the charged species are taken from [145].

The simulations are performed for different concentrations of methane, locations in the discharge gap, and CCRF plasma regimes. The reactions rates are dependent on the fixed values of T_g and T_e and the number density of electrons is maintained constant. The initial guess for the mole fractions of the hydrogen species are based on the results of the hydrogen plasma model. The initial mole fraction of methane is assumed to be 5%, 10% or 30% and those of all the other hydrocarbon species are taken as 0.

Figure 3.10 compares the steady state mole fractions of different neutral and ionic species for various gas mixture compositions using plasma properties at the midpoint of the discharge gap for a hybrid discharge with V_{amp} = 209.5 V at 9.5 mbar. The mole fractions do not show a very strong dependence on the methane and hydrogen gas concentrations overall. This is corroborated by sensitivity analyses on experimental growth characteristics for the system performed by Alrefae [136] as shown in Figure 3.11. The mole fractions in Figure 3.10 do not vary monotonically with the methane concentration, but the assumption of extending the hydrogen plasma

Table 3.4. Electron impact reactions modeled for hydrocarbon chemistry.

Chemical reaction	**Reference**
$e + CH_5^+ \rightarrow CH_4 + H$	146
$e + C_2H_5^+ \rightarrow C_2H_4 + H$	146
$e + CH_4 \rightarrow e + CH_3 + H$	147
$e + CH_4 \rightarrow e + CH_2 + H_2$	147
$e + CH_4 \rightarrow e + CH + H + H_2$	147
$e + CH_4 \rightarrow e + C + H_2 + H_2$	147
$e + C_2H_6 \rightarrow e + C_2H_4 + H_2$	148
$e + C_2H_4 \rightarrow e + C_2H_2 + H_2$	148
$e + C_2H_2 \rightarrow e + C_2H + H$	148
$e + CH_4 \rightarrow 2e + CH_4^+$	149
$e + C_2H_6 \rightarrow 2e + C_2H_6^+$	149
$e + C_2H_6 \rightarrow 2e + C_2H_5^+ + H$	150
$e + C_2H_6 \rightarrow 2e + C_2H_4^+ + H_2$	150
$e + C_2H_6 \rightarrow 2e + C_2H_3^+ + H + H_2$	150
$e + C_2H_6 \rightarrow 2e + C_2H_2^+ + H_2 + H_2$	150
$e + C_2H_4 \rightarrow 2e + C_2H_4^+$	149
$e + C_2H_2 \rightarrow 2e + C_2H_2^+$	149

properties for higher methane concentration mixtures may result in some deviation from reality.

Apart from H_2 and H, the neutral species with the highest mole fractions are C_2H and C_2H_2, and the ionic species are $C_2H_3^+$, $C_2H_4^+$ and $C_2H_6^+$. In contrast to diamond, CH_3 is not the most important precursor for graphene growth [139] and thus, CH_3 has a low mole fraction $\sim 10^{-6}$. The dominant ionization reactions in all the cases are the electron impact ionization of C_2H_6 and C_2H_4 into $C_2H_6^+$ and $C_2H_4^+$,

respectively. For the 10% CH_4 case, the electron impact dissociation of CH_4 into C and hydrogen impact dissociation of C_2H_2 into C and CH_3 have high rates increasing the concentration of C in the gas mixture. When the CH_4 concentration is further increased to 30%, the third body dissociation reaction $C_2H_2 + M \rightarrow H + C_2H + M$ plays a major role due to the enhanced rate in the presence of CH_4 as a third body. In addition, electron impact dissociation of C_2H_2 into C_2H and H leads to a high concentration of C_2H in the mixture.

The sensitivity analysis indicates that the parameters which exert the greatest influence are the gas pressure and nitrogen concentration. Nitrogen is not modeled in this work. However, a change in the gas pressure or input power at threshold values changes the CCRF discharge regime of operation. The species mole fractions under different regimes at the midpoint of the discharge for 95% H_3 and 5% CH_4 are compared in Figure 3.12. For all the cases, the dominant neutral hydrocarbon species are still C_2H and C_2H_2, and the dominant ions are $C_2H_6^+$ and $C_2H_4^+$. The low gas temperature of the α discharge leads to a high rate of formation of C_2H_6 from CH_3, reducing the concentration of CH_3 and H in the discharge. The high electron temperature leads to higher electron impact ionization and dissociation rates leading to higher concentrations of C_2H_4, C_2H_3, C_2H_2, C_2H, $C_2H_4^+$ and $C_2H_6^+$. However, the formation of $C_2H_3^+$ and $C_2H_5^+$ ions occurs due to H_3^+ as seen in Table 3.3. The higher concentration of H_3^+ for the hybrid and γ modes when compared to the α mode leads to higher concentration of these ions for the hybrid and γ modes. For these modes, $C_2H_3^+$ is also one of dominant ionic species in the discharge.

The major differences in the mole fractions occur due to the difference in electron temperatures, which can not only be varied by operating in different regimes, but also by moving the substrate close to or away from the electrodes based on the desired precursor concentrations. Figure 3.13 compares the species mole fractions for a 95% H_2 and 5% CH_4 hybrid discharge at V_{amp} = 209.5 V and P_g = 9.5 mbar at 3 different locations. The location x = 0.05 cm lies in the sheath region very close to the electrode and has high electron temperature and low electron number density.

This leads to high ionization rates and the ions have the highest mole fractions at this location. The dominant ions are $C_2H_3^+$, $C_2H_4^+$ and $C_2H_6^+$. The electron temperature is high enough to ionize CH_4 into CH_4^+ which undergoes ion conversion to CH_5^+ in the presence of H_2. The dominant neutrals at this location are C_2H and CH_3.

If the substrate is moved to the edge of the electrode sheath at $x = 0.5$ cm, the electron temperature drops and the electron number density is still not as high as the center of the discharge. This leads to very low ionization rates and the hydrocarbon ions have negligible concentrations. The dominant ion is H_3^+. This location is suitable for nanostructure growth when low ion concentrations are desired and the most important precursor is CH_3. Low precursor concentrations are desirable for the deposition of single layer graphene in order to avoid over deposition [35]. At the center of the discharge gap ($x = 2.25$ cm), the electron number densities are high and the ionization rates increase once again despite the low electron temperature leading to the formation of $C_2H_3^+$, $C_2H_4^+$ and $C_2H_6^+$. Furthermore, the concentrations of C_2H and C_2H_2 are high and the concentration of CH_3 drops. Overall, for all the cases, the neutral hydrocarbon species with the highest concentration is C_2H for the R2R RFCVD system.

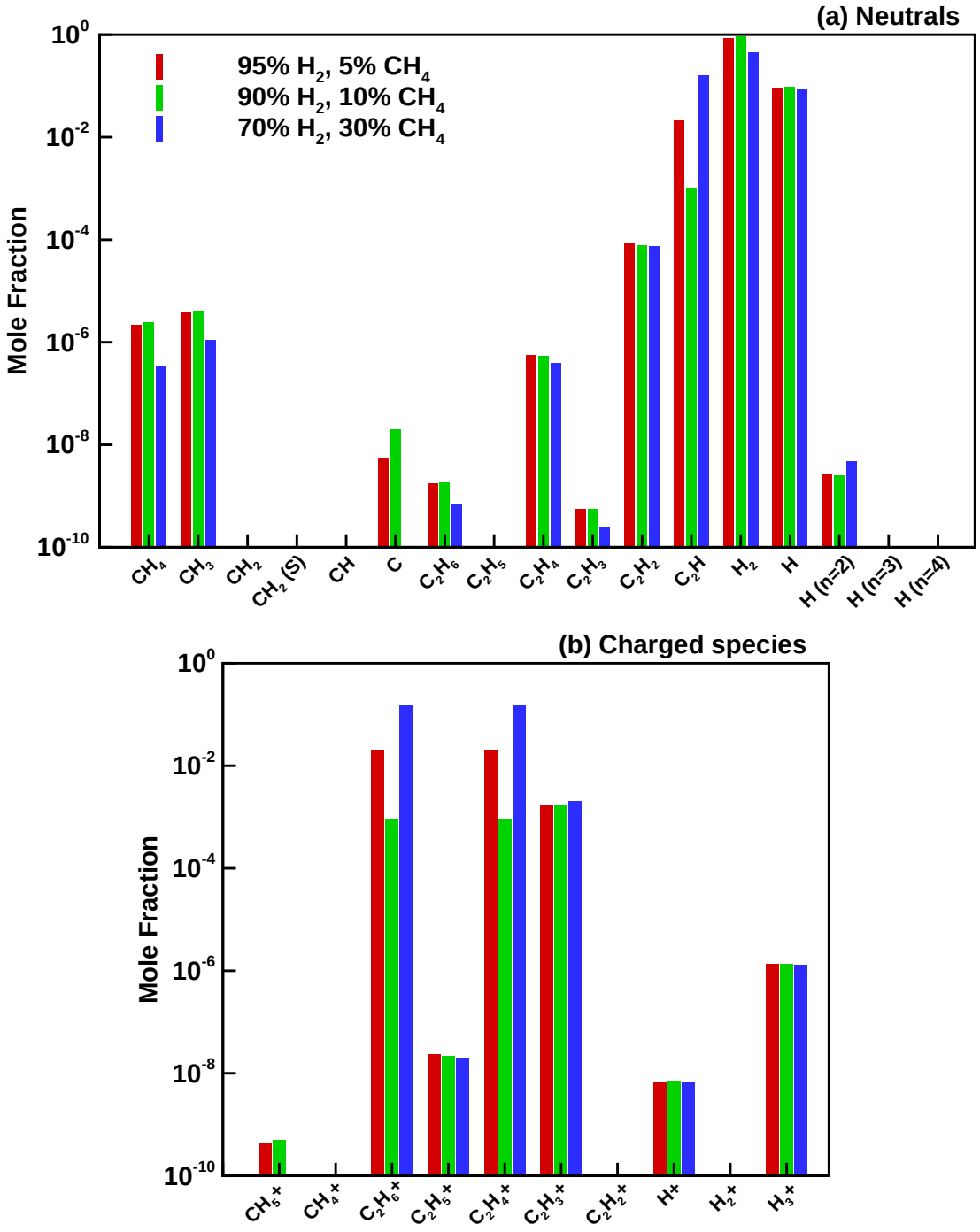

Figure 3.10. Effect of methane concentration on (a) neutral and (b) ionic species mole fractions for H_2 plasma properties at V_{amp} = 209.5 V, P_g = 9.5 mbar and x = 2.25 cm.

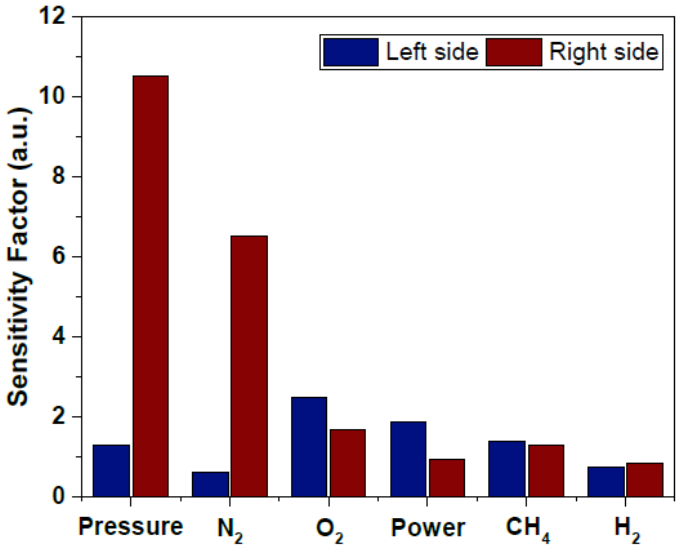

Figure 3.11. The sensitivity of graphene growth quality to different process inputs based on statistical analysis [136].

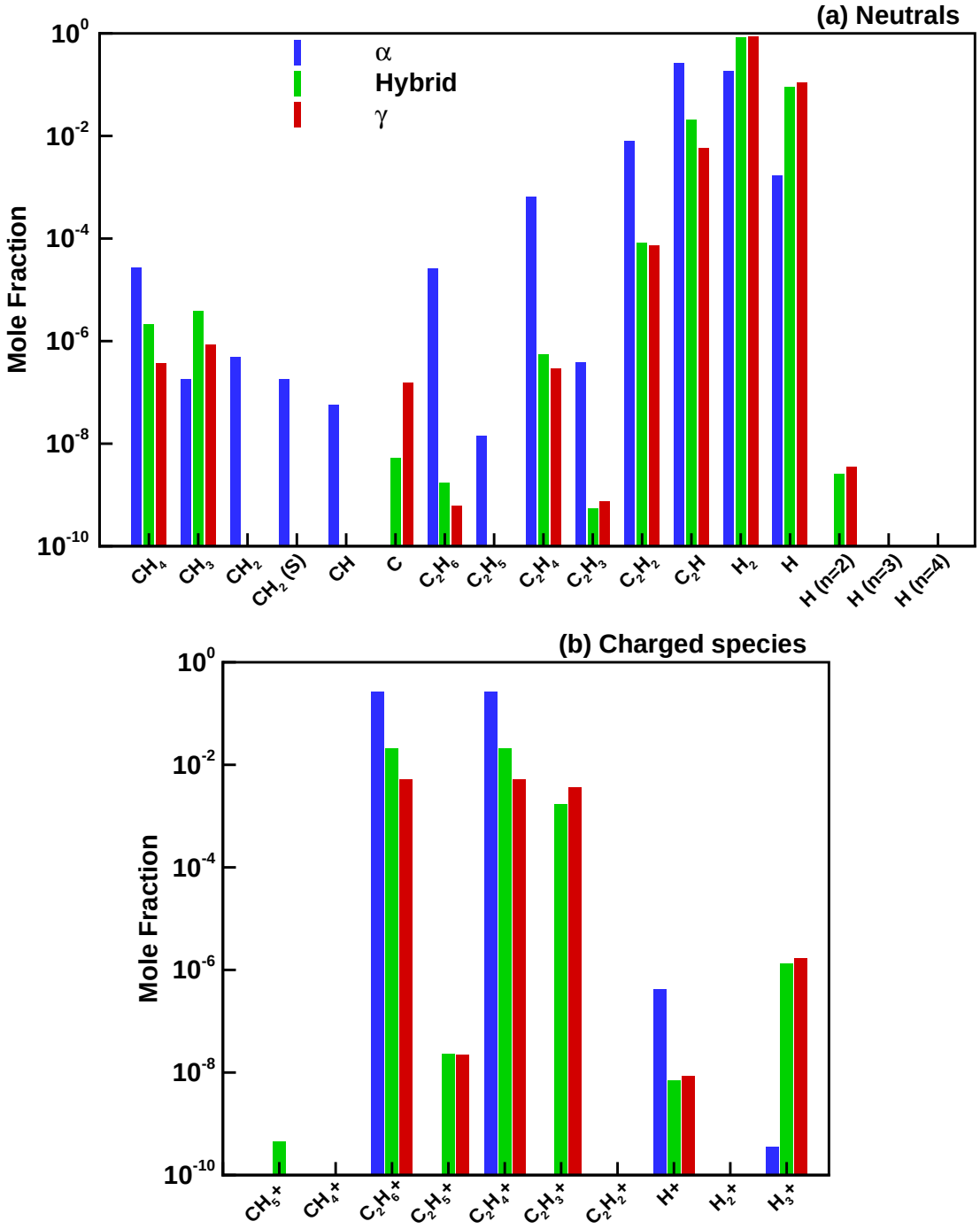

Figure 3.12. (a) Neutral and (b) ionic species mole fractions under different CCRF discharge regimes for H_2 plasma properties at $P_g = 9.5$ mbar, x = 2.25 cm and 95% H_2 and 5% CH_4. The voltage amplitude for α regime is 175 V, hybrid regime is 209.5 V and γ regime is 240 V.

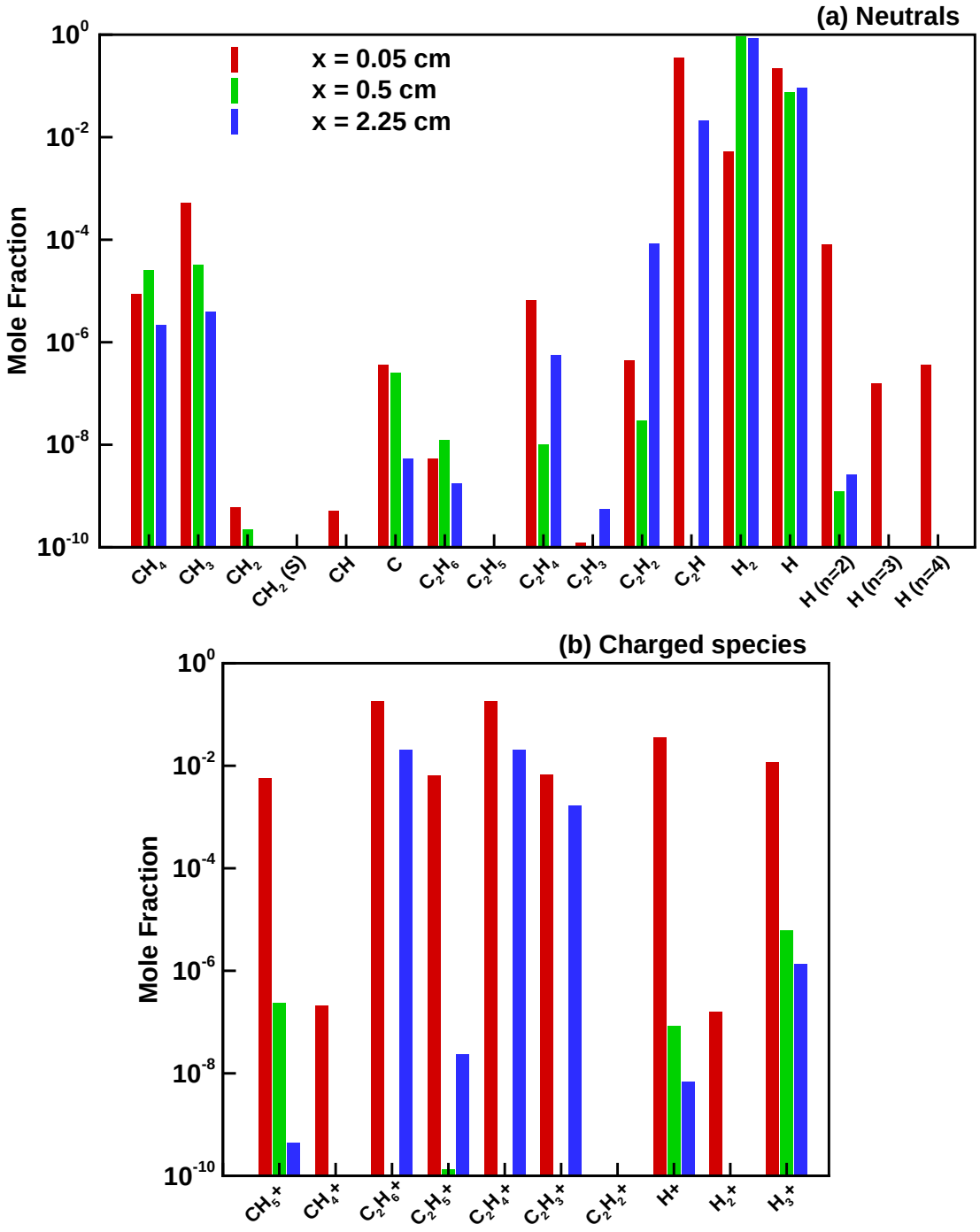

Figure 3.13. (a) Neutral and (b) ionic species mole fractions at different discharge gap locations for H_2 plasma properties at V_{amp} = 209.5 V, P_g = 9.5 mbar and 95% H_2 and 5% CH_4.

4. PLASMA MODELING OF FIELD-EMISSION DIELECTRIC BARRIER DISCHARGES

This chapter presents two different designs of FE-DBDs, outlines the kinetic approach used to simulate the FE-DBD plasma, and performs a parametric study to evaluate the effect of the input properties on the plasma characteristics.

4.1 Concept and Numerical Model

4.1.1 FE-DBD Design Concepts

The application of microplasmas for flow actuation requires surface discharges due to their ability to transfer momentum into the flow. The most popular method of achieving this in the macroscale is to use an asymmetric dielectric barrier discharge actuator as shown in Figure 4.1 (a). The actuator consists of one electrode embedded under a dielectric layer, and the other exposed to the gas. Due to the inherent asymmetry in this design with offset electrodes, the plasma pumps the neutral molecules it comes into contact with selectively along one direction. In the FE-DBD concept, the electrodes are brought together so as to increase the electric field between them. The surface irregularities lead to breakdown at low input voltages due to field emission. This concept was presented in [74, 75, 151] wherein the effects of dielectric thickness, electrode thickness, and gas pressure on the plasma properties were studied. The most optimal dielectric and electrode thicknesses were found to be 4 μm and 1 μm, respectively, for 100 μm wide electrodes, and these numbers have been adopted for the present work. The propensity of copper electrodes to oxidize in the presence of plasma renders them unfit for application to hydrogen-air combustion. Consequently, gold electrodes are used in this work. The pressure is 1 atm.

The second method of generating a surface discharge is by using planar electrodes, both of which are exposed to the gas as shown in Figure 4.1 (b). This concept is easier to microfabricate and can be made to selectively pump the flow in a direction by applying a DC bias to the AC input voltage applied. This design also uses gold electrodes that are 0.5 μm thick in order to ensure that the total thickness of the exposed electrodes for both the designs are the same. The electrode gap is modeled at 2.5 μm. The breakdown voltage can be further reduced by decreasing this spacing, but the limitations of microfabrication for successful reproduction using popular photolithography techniques restricts this value to 2.5 μm. For both types of actuators, the application of an AC voltage at the electrodes leads to transfer of momentum and energy from the plasma to the gas which can be used for pumping, mixing, and heating the flow. The rest of this chapter determines the most suitable frequency for the AC input voltage and the type of FE-DBD actuator that is suitable for different applications.

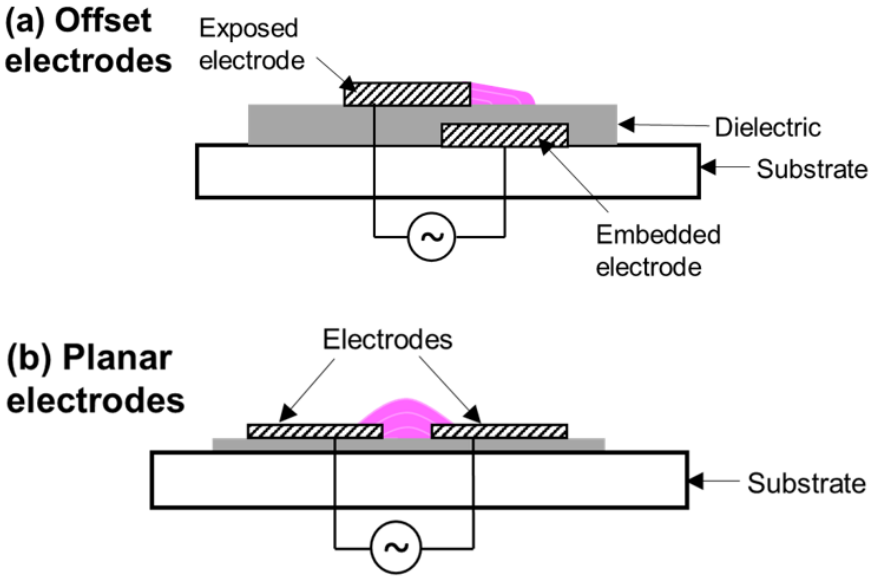

Figure 4.1. FE-DBD concepts with (a) offset and (b) planar electrodes for the generation of surface microdischarges.

4.1.2 PIC/MCC Model

The minimum characteristic length scale of the FE-DBD is the distance between the electrodes of the planar electrode actuator, which leads to a Knudsen number (Kn) of 0.2 with respect to momentum transfer collisions of electrons with neutrals for nitrogen. This Kn represents the rarefied flow regime. The energy relaxation time for the electrons is 0.15 ns, which is lower than the time period of the RF cycle. Consequently, the continuum approximation for plasma modeling is not valid and the kinetic approach of Particle-in-Cell with Monte Carlo Collisions (PIC/MCC) is used to resolve the sources of momentum and energy transferred by the plasma to the gas.

PIC models the motion of charged particles in the presence of an electric field, which is determined based on Poisson's equation at each time step. MCC models the collision of charged species with the neutrals based on the new energy and collision cross-sections at every time step using the Boltzmann equation given by:

$$\frac{\partial}{\partial t}\left(f_k n_k\right) + \vec{\mathbf{v}_k} \cdot \frac{\partial}{\partial \vec{\mathbf{r}}}\left(f_k n_k\right) + \frac{q_k \vec{\mathbf{E}}}{m_k} \cdot \frac{\partial}{\partial \vec{\mathbf{v}_k}}\left(f_k n_k\right) = C_k \tag{4.1}$$

where, k represents the charged particle which can be an electron or a nitrogen ion, t is time, $\vec{\mathbf{x}}$ and $\vec{\mathbf{v}}$ are the position and velocity of the particle, $\vec{\mathbf{E}}$ is the electric field, f is the velocity distribution function, and q, m and n are the particle charge, mass and number density respectively. C is the collision term which accounts for electron-neutral elastic, excitation, and ionization collisions [152], as well as ion-neutral elastic, and charge exchange collisions [153]. Coulomb collisions are neglected on account of the average ionization fraction being lower than 0.001 [37]. The field emission and secondary electron emission are introduced into the domain from the electrode surface boundary. The steps involved in a PIC/MCC simulation at every time step are shown in Figure 4.2.

Figure 4.3 shows the simulation domain and boundary conditions for both the offset and planar electrode FE-DBDs. For the offset electrode actuator, the exposed electrode always acts as the cathode due to the negative DC bias voltage applied. On the other hand, for the planar electrode actuator, whether or not the cathode

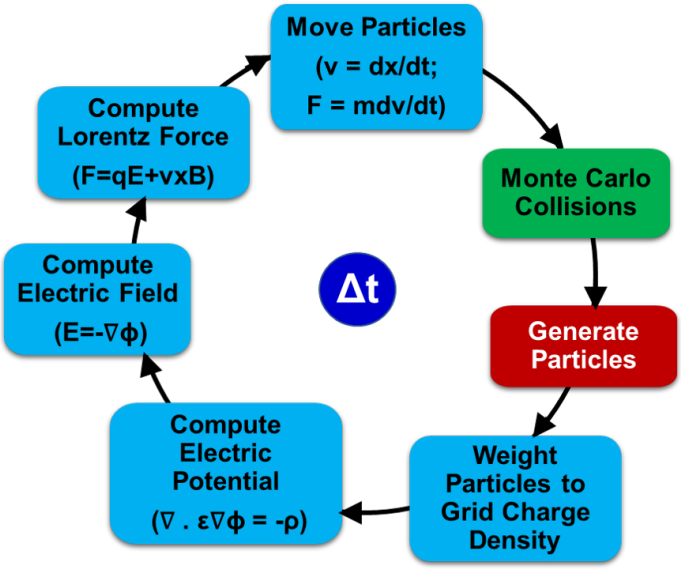

Figure 4.2. Schematic of the PIC/MCC solution steps.

and anode are fixed depends on the DC bias voltage that is applied. At microscale electrode gaps, field emission plays a significant role in the generation of an electric discharge by reducing the breakdwon voltage. Field emission is modeled using the Fowler-Nordheim equation [56] given by:

$$j_{FN} = \frac{A_{FN}\beta^2 E^2}{\phi_w t^2(y)} \exp\left(-\frac{B_{FN}\phi_w^{3/2}\nu(y)}{\beta E}\right) \tag{4.2}$$

where, j_{FN} is the field emission current density, A_{FN} and B_{FN} are Fowler-Nordheim constants, β is the field enhancement factor, E is the electric field, and ϕ_w is the work function for the electrode material. The functions of $y = 3.79 \times 10^{-5}\sqrt{\beta E}/\phi_w$ are given by $\nu(y) = 0.95 - y^2$ and $t^2 \approx 1.1$. The field enhancement factor is taken to be 50 and the secondary electron emission coefficient of the electrodes is taken as $\gamma = 0.001$. The effect of increasing these parameters is explored later in this chapter.

The maximum Debye length, λ_D, is 2.04 μm and the cell size, Δx, is 0.5 μm so that $\Delta x \leq \lambda_D/2$. The important time scales related to the plasma simulations are: (i) the smallest time period of the RF cycle which is at 10 GHz: $\tau_{RF} = 0.1$ ns, (ii)

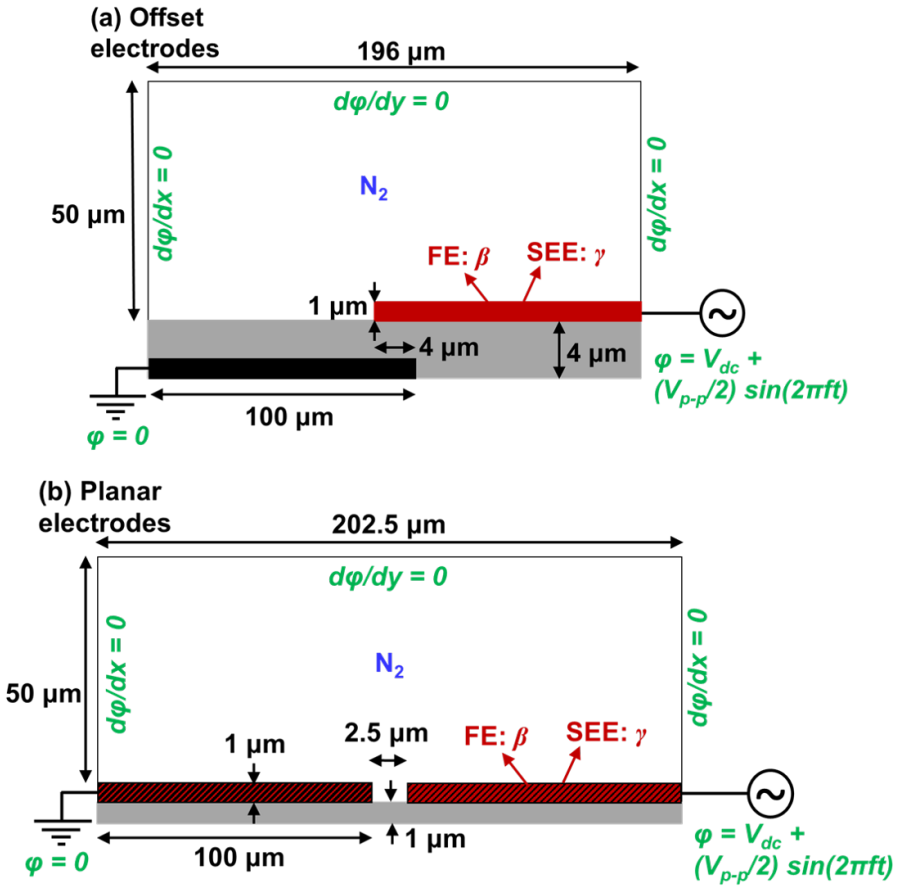

Figure 4.3. Modeling setup and boundary conditions for FE-DBD plasma simulations using PIC/MCC.

the mean collision time of electrons with neutrals: $\tau_m = 0.3$ ps, and (iii) the shortest time taken by an electron to cross a single cell: $\tau_e = 0.3$ ps. The time step of 0.2 ps is chosen for the PIC/MCC simulations so that it is smaller than the minimum of the three aforementioned time scales. The number of physical to computational particles is 10^6 i.e., each computational particle is a super-particle that represents 10^6 real particles.

4.1.3 Momentum and Energy Sources

The plasma transfers momentum and energy to the flow during the collisions between the charged particles and neutrals. These source terms can be obtained from the PIC/MCC simulations and are coupled with the Navier-Stokes equations, given in Chapter 5, by means of source terms added to the momentum and energy conservation equations [74]. The momentum sources can be approximated as directed body force terms [154,155] based on the electric field and the net space charge density neglecting negative ions as:

$$f_{b,i,approx} = eE_i \left(n_+ - n_e\right) \tag{4.3}$$

where, $f_{b,i,approx}$ and E_i are the body force and electric field in direction i respectively. The energy source can be approximated as a Joule heating term, $\dot{Q}_{approx}$, as:

$$\dot{Q}_{approx} = \vec{\mathbf{J}} \cdot \vec{\mathbf{E}} \tag{4.4}$$

where, $\vec{\mathbf{J}}$ and $\vec{\mathbf{E}}$ are the current density and electric field vectors respectively. The time-averaged values of these approximations are used for plasma-flow coupling in [74].

The momentum and energy transferred from the electrons and ions to the neutrals can also be determined directly from PIC/MCC by tracking the exchange during elastic, excitation and charge exchange collisions. This is similar to the method given in [156]. The body force term computed in this way, $f_{b,i}$, over a time Δt is given by:

$$f_{b,i} = -\frac{\sum\limits_{k=e,+}\left(np2c_k \sum\limits_{collisions} m_k \Delta v_{i,k}\right)}{\Delta x \Delta y \Delta t} \tag{4.5}$$

where, the subscript k represents electrons and ions, $np2c$ is the number of physical to computational particles, m is the mass of the particle, Δv_i is the change in velocity of the particle along the direction i due to the collision, and Δx and Δy are the 2D cell dimensions. There is a negative sign because the momentum lost by the electrons are ions represents the momentum gained by the neutrals as the source

term. The magnitude of the body force is computed from the x and y components as $f_b = \sqrt{f_{b,x}^2 + f_{b,y}^2}$. The energy source term can be calculated similarly as:

$$\dot{Q} = -\frac{\sum_{k=e,+} \left(np2c_k \sum_{collisions} \Delta\epsilon_k \right)}{\Delta x \Delta y \Delta t} \tag{4.6}$$

where, $\Delta\epsilon_k$ is the change in energy of the particle during each collision.

Figure 4.4 shows the time-averaged contours of body force magnitude obtained using the approximation based on the net space charge density as well as using the collisional momentum transfer tracking directly from PIC/MCC for the offset electrode FE-DBD. The peak-to-peak input voltage applied is 250 V at 10 MHz with a -125 V DC bias such that the exposed electrode is always the cathode. The approximation in Equation 4.3 results in a spatially averaged body force magnitude of 1.12×10^5 N/m^3. This is an order of magnitude higher than the collisional value of 1.55×10^4 N/m^3 determined based on Equation 4.5. The approximation also results in a more concentrated body force distribution over the exposed electrode, whereas collisionally, the distribution is more uniform above the entire DBD design. Figure 4.5 compares the time-averaged energy source contours based on the Joule heating approximation and the collisional energy transfer to the neutrals. The spatially averaged heat source values based on the approximation in Equation 4.4 and the collisional energy transfer in Equation 4.6 are 5.96×10^7 W/m^3 and 1.67×10^7 W/m^3 respectively. The Joule heating value is higher than the collisional value by a factor of 2.5 and the collisional source field is once again more uniform than the approximation. Since the approximate expressions overestimate the momentum and energy transfer from the charged particles to the neutrals, the more accurate collisional expressions are used to determine the source terms in this work.

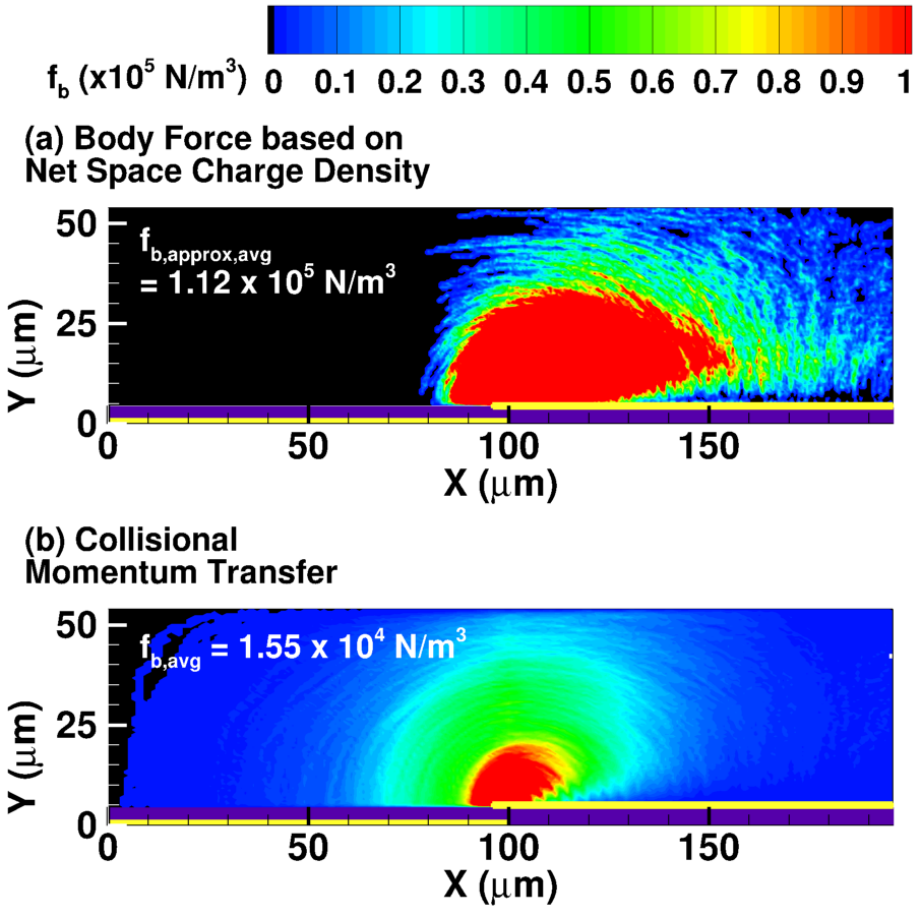

Figure 4.4. Comparison of momentum source for the offset electrode FE-DBD (Figure 4.3 (a)) computed based on (a) net space charge density (Equation 4.3) and (b) momentum transfer tracking during collisions (Equation 4.5) at 250 V_{p-p}, -125 V_{dc} and 10 MHz.

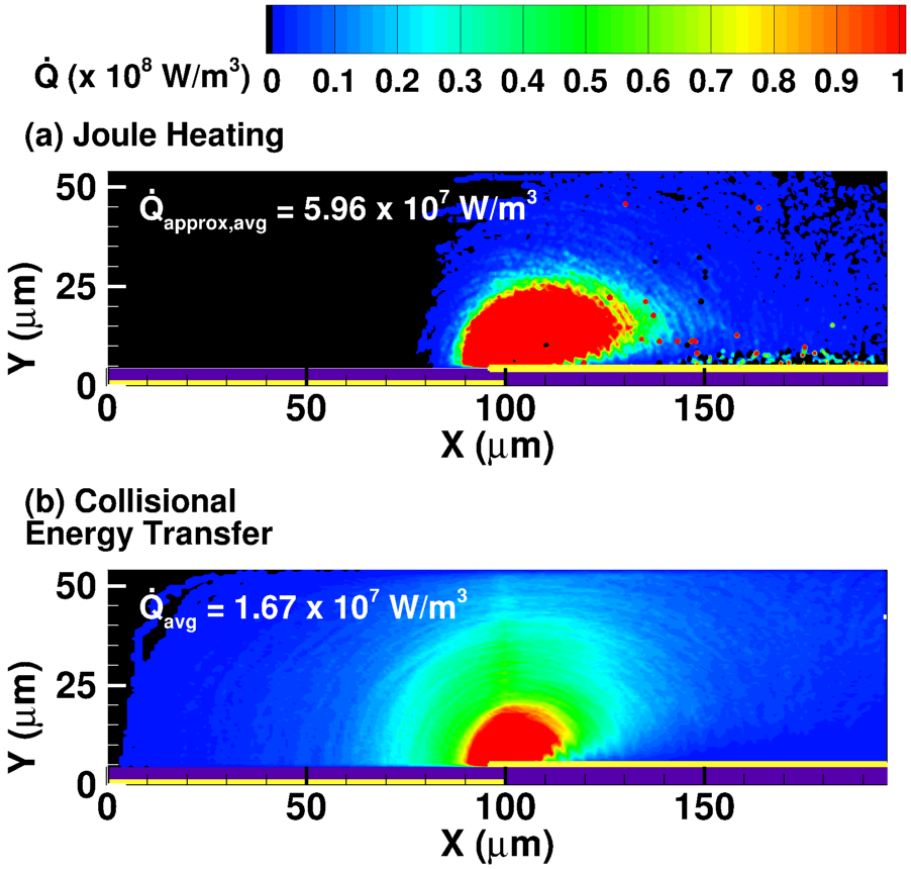

Figure 4.5. Comparison of heat source for the offset electrode FE-DBD (Figure 4.3 (a)) computed based on (a) Joule heating (Equation 4.4) and (b) energy transfer tracking during collisions (Equation 4.6) at 250 V_{p-p}, -125 V_{dc} and 10 MHz.

4.2 Plasma Properties

This section presents the results of the PIC/MCC simulations performed at different input frequencies, voltages, FE-DBD configurations, and material properties. The momentum and energy sources that are coupled to the Navier-Stokes equations in Chapter 5 are provided.

4.2.1 Effect of Frequency

PIC/MCC simulations are performed for the offset electrode FE-DBD shown in Figure 4.1 (a) for 250 V_{p-p} input voltage and -125 V_{dc} bias at different driving frequencies in the range of 10 MHz to 10 GHz. Figure 4.6 shows the time evolution of the ion number density in the discharge during a 10 MHz cycle. The ions are generated through impact ionization of the field emitted electrons and the ion density in the vicinity of the cathode (exposed electrode) changes during the cycle. This is due to the change in the electric field which controls the number density of the field emitted electrons. Figure 4.7 shows that the ion number densities generated during a 1 GHz cycle are higher than that during a 10 MHz cycle. The ions are also concentrated in the vicinity of the cathode edge that is close to the anode indicating that the ions do not have enough time to diffuse away during the faster cycle. The advantage of having a higher ion number density is greater momentum and energy transfer to the neutrals at he same input voltage.

The cycle averaged body force and heat source terms based on the collisional momentum and energy transfer given by Equations 4.5 and 4.6 are determined for each case and the spatially averaged values over the 196 x 50 μm region are tabulated in Table 4.1. The momentum and energy transferred from the charged species to the gas increase by a factor of 2 when the driving frequency increases from 10 MHz to 100 MHz. They stay relatively constant between 100 MHz and 1 GHz. At 10 GHz, they fall because the driving frequency exceeds 6.4 GHz which is the energy relaxation frequency of nitrogen at atmospheric pressure [37]. Since GHz frequencies produce the

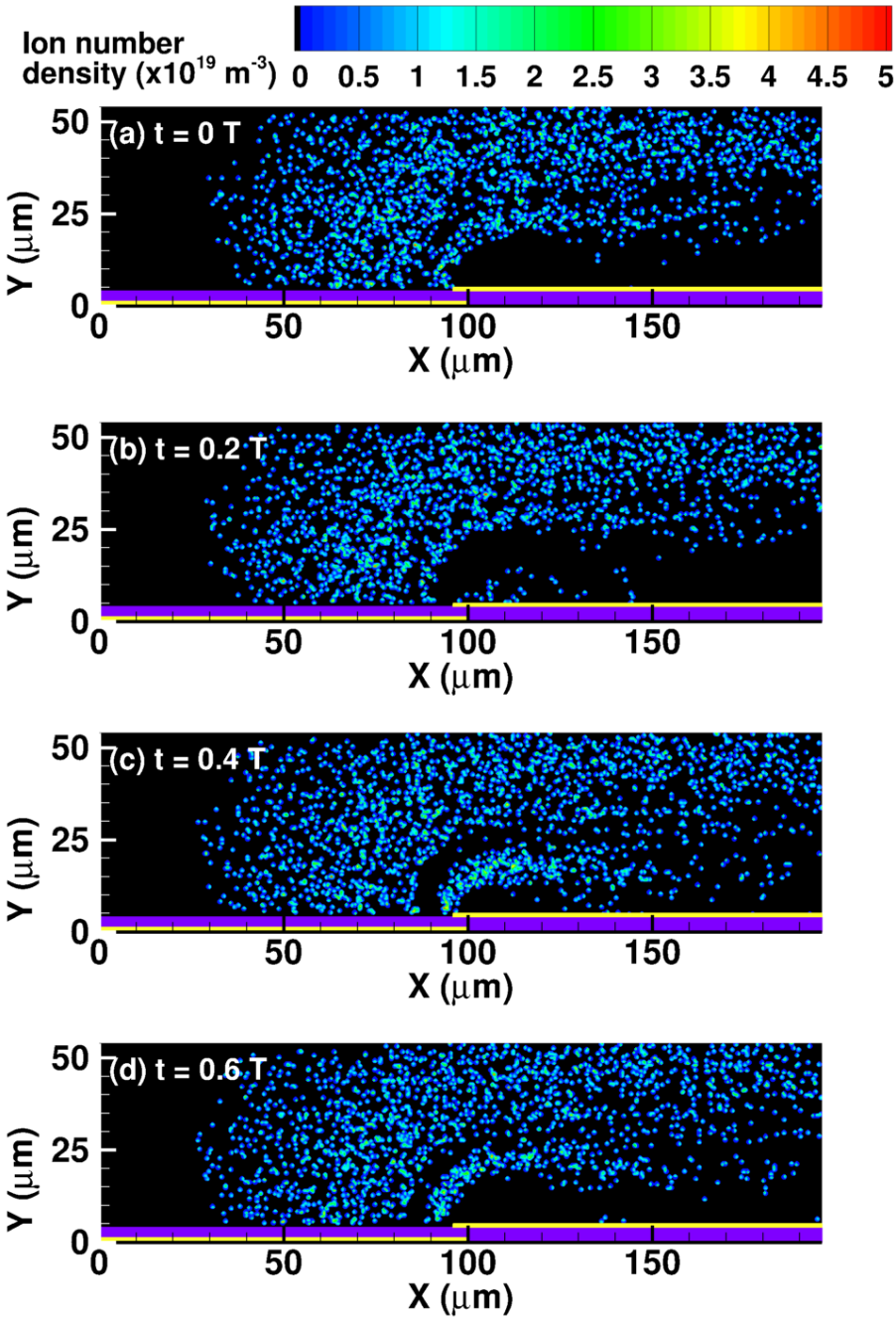

Figure 4.6. Evolution of ion number densities generated by an offset electrode FE-DBD with time for 250 V_{p-p} input voltage with -125 V_{dc} at 10 MHz.

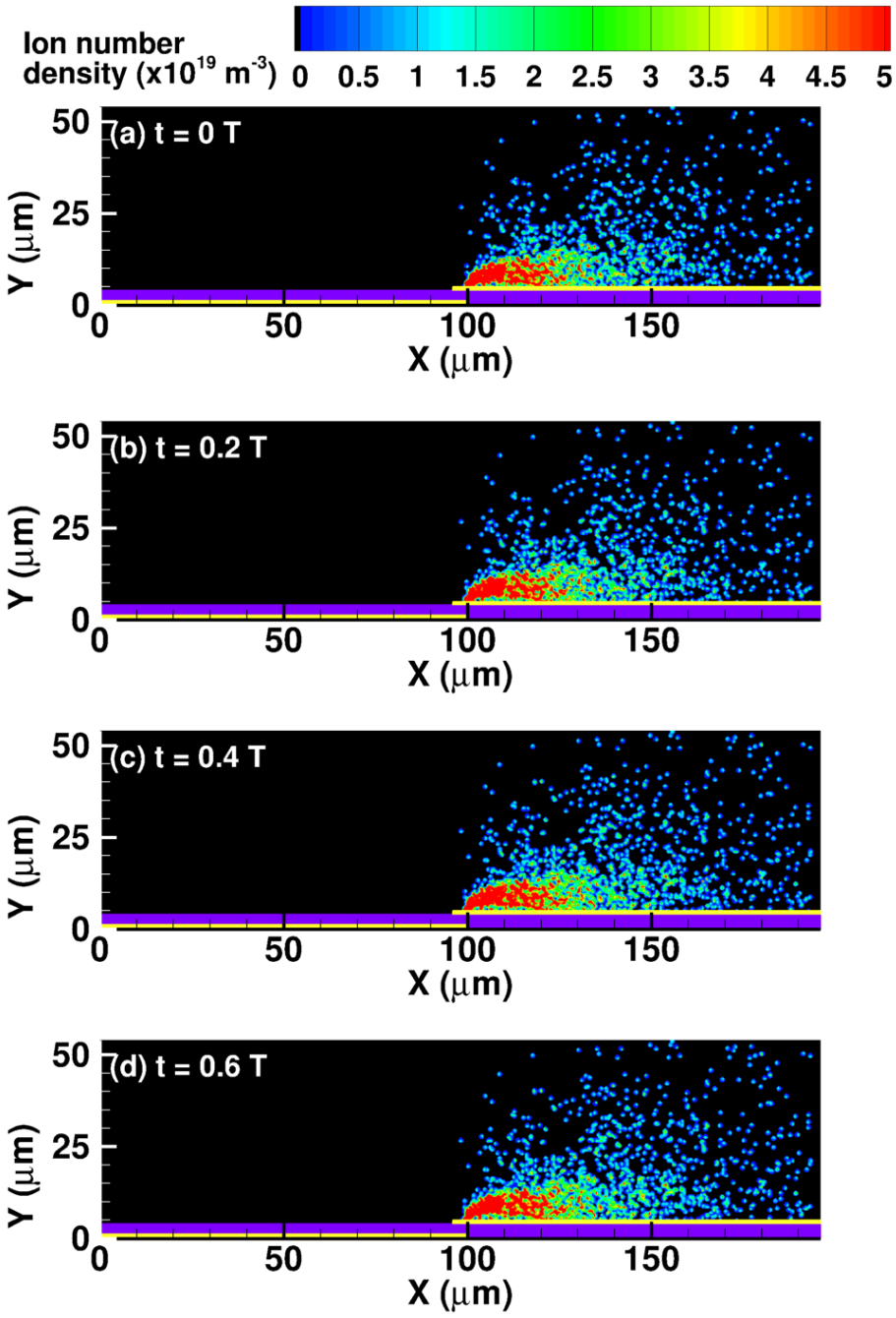

Figure 4.7. Evolution of ion number densities generated by an offset electrode FE-DBD with time for 250 V_{p-p} input voltage with -125 V_{dc} at 1 GHz.

highest momentum and energy transfer at the same input voltage when compared to other frequencies, the driving frequency is maintained at 1 GHz for all the subsequent calculations presented here.

Table 4.1. Effect of driving frequency on the spatially and cycle averaged body force and heat source for 250 V_{p-p} input voltage with -125 V_{dc} bias.

Frequency	f_b [$\mathbf{N/m^3}$]	$\dot{Q}$ [$\mathbf{W/m^3}$]
10 MHz	1.55×10^4	1.7×10^7
100 MHz	3.48×10^4	3.7×10^7
1 GHz	3.54×10^4	3.7×10^7
10 GHz	3.15×10^4	2.8×10^7

4.2.2 Microplasma Structure and Source Terms

The plasma properties and source terms for the offset and planar electrode FE-DBDs at 1 GHz are compared here. The input voltage amplitude is maintained high enough to sustain a stable discharge without arcing such that a spatially averaged body force of at least 10^6 N/m^3 and heat source of at least 10^9 W/m^3 are imparted to the gas. Even though this results in different input voltages for the offset and planar electrode FE-DBDs, this is done so that their source term induced flow actuation characteristics are comparable for the different actuator types. For the offset electrode FE-DBD, the voltage is maintained at 325 V_{p-p} with a DC bias voltage of -162.5 V such that the exposed electrode is always the cathode. Cycle averaged contours of the ion number density, electron number density and electron temperature are shown in Figure 4.8. The ion number densities are more than an order of magnitude higher than the electron number densities and both are concentrated in the 100 x 50 μm region above the cathode. The maximum and average number density values and average

electron temperature in this region where the charged particles are concentrated are provided in Table 4.2. The average electron temperature in this region is 1.53 eV.

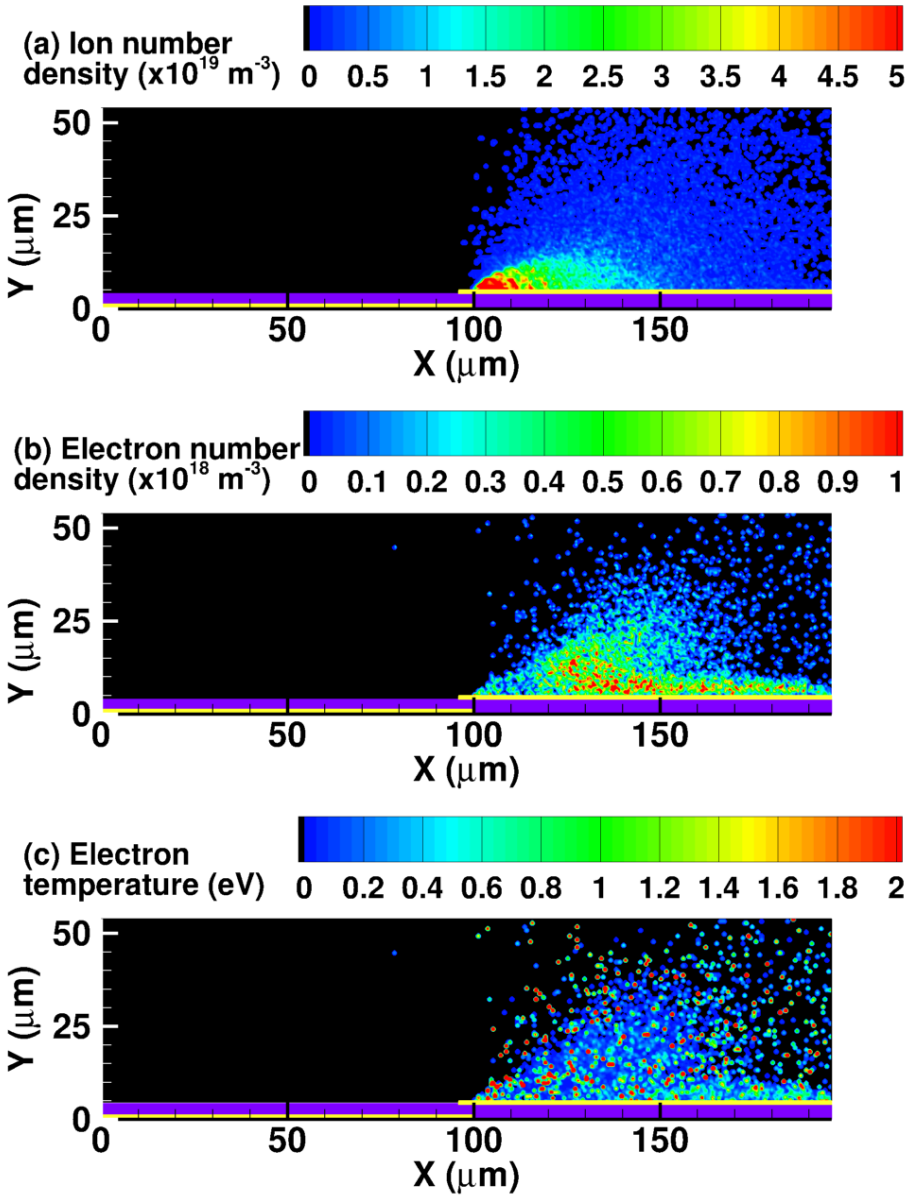

Figure 4.8. Contours of (a) ion number density, (b) electron number density, and (c) electron temperature in the microplasma generated by offset electrode FE-DBD for 325 V_{p-p} input voltage with -162.5 V_{dc} at 1 GHz.

Plasma non-neutrality is the driving force for the momentum transfer between the charged particles and neutrals. The high non-neutrality of field emission discharges makes them attractive for flow actuation applications. The difference between the ion and electron number densities depict the non-neutrality of the plasma. Figure 4.9 presents the cycle averaged contours of the non-neutrality of the plasma generated by the different FE-DBD configurations. The offset electrode actuator with the aforementioned bias conditions is shown in Figure 4.9 (a). The collisional momentum and energy transferred to the gas in the 196 x 50 μm region are shown in Figures 4.10 (a) and (b) respectively. The sources are more concentrated in the space charge region above the exposed electrode and have spatially averaged values of 1.77 MN/m^3 and 3.13 GW/m^3 respectively. The power consumed by the actuator is determined by integrating the product of the voltage and current density on the electrode surface over one RF cycle and is found to be 241.1 mW/cm for the 2D actuator of 100 μm electrode width. The power consumption per unit area of the electrode is 24.11 W/cm^2.

The planar electrode FE-DBD can be used for two different operations. The first is to transfer directed momentum and energy to the gas. This requires a DC bias voltage such that one of the electrodes is always the cathode. Figure 4.9 (b) shows the space charge number density and figures 4.10 (c) and (d) show the sources generated for 275 V_{p-p} input with -137.5 V_{dc} bias. The number densities are lower in this case due to the lower input voltage and are summarized in Table 4.2. The sources are more spread out when compared to the offset electrode FE-DBD because both the electrodes are exposed and the charged particles oscillate between the two. They possess higher values directly above the right electrode which is the cathode. The average momentum source has a value of 1.09 MN/m^3 which is comparable to the corresponding value for the offset electrode FE-DBD. The energy source is more spread out, but the high values are concentrated in a very small area and their absolute values are lower than the offset electrode case. Consequently, the average energy source has a lower value of 1.80 GW/m^3. The actuator consumes an input power of 29.7 mW/cm or 2.97 W/cm^2.

If the DC component of the voltage is not applied, the two electrodes alternate between functioning as the anode and cathode for half of an input cycle each. This results in a net zero momentum source in the X-direction. Figures 4.10 (e) and (f) show that the magnitude of the momentum and energy sources are spread out and symmetric above the two electrodes, as expected. Energy and Y-momentum are still transferred to the gas, which impart heat and vorticity to the gas. Such a device could be used to ignite the mixture in a region where flow pumping is not desired. The space charge is concentrated at the center of the discharge region as shown in Figure 4.9 (c). The average magnitude of the momentum and energy sources in this case are 2.67 MN/m^3 and 5.03 GW/m^3 respectively. The momentum source magnitude is entirely due to the Y-component. The power consumed at the electrodes has a higher value of 47.5 mW/cm or 4.75 W/cm^2 when compared to the case with a DC bias voltage. The average electron temperature in this case is 2.66 eV. The three source profiles shown in Figure 4.10 are coupled to the flow in microchannels in Chapter 5.

Table 4.2. Cycle averaged plasma properties in the simulated region for offset electrode actuators at 325 V_{p-p}, 1 GHz and planar electrode actuators at 275 V_{p-p}, 1 GHz.

Actuator	$\mathbf{n}_{+,max}$ $[\mathbf{m}^{-3}]$	$\mathbf{n}_{+,ave}$ $[\mathbf{m}^{-3}]$	$\mathbf{n}_{e,max}$ $[\mathbf{m}^{-3}]$	$\mathbf{n}_{e,ave}$ $[\mathbf{m}^{-3}]$	$\mathbf{T}_e$ [eV]
Offset (AC+DC)	3.56×10^{20}	1.40×10^{18}	2.06×10^{19}	5.50×10^{16}	1.53
Planar (AC+DC)	3.98×10^{19}	3.46×10^{16}	4.78×10^{17}	2.93×10^{14}	2.11
Planar (AC)	2.50×10^{19}	3.75×10^{16}	5.77×10^{17}	6.94×10^{14}	2.66

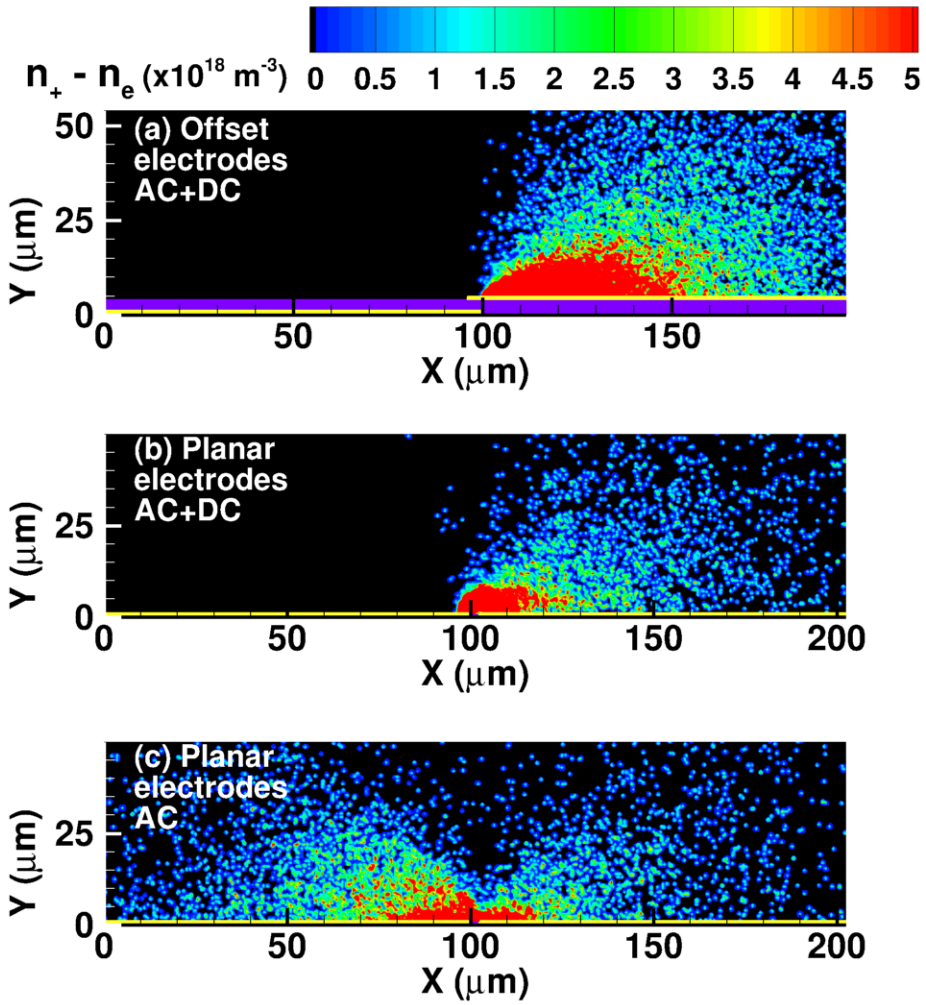

Figure 4.9. Comparison of net space charge number densities at 1 GHz for (a) 325 V_{p-p}, -162.5 V_{dc}, (b) 275 V_{p-p}, -137.5 V_{dc}, and (c) 275 V_{p-p}, 0 V_{dc}.

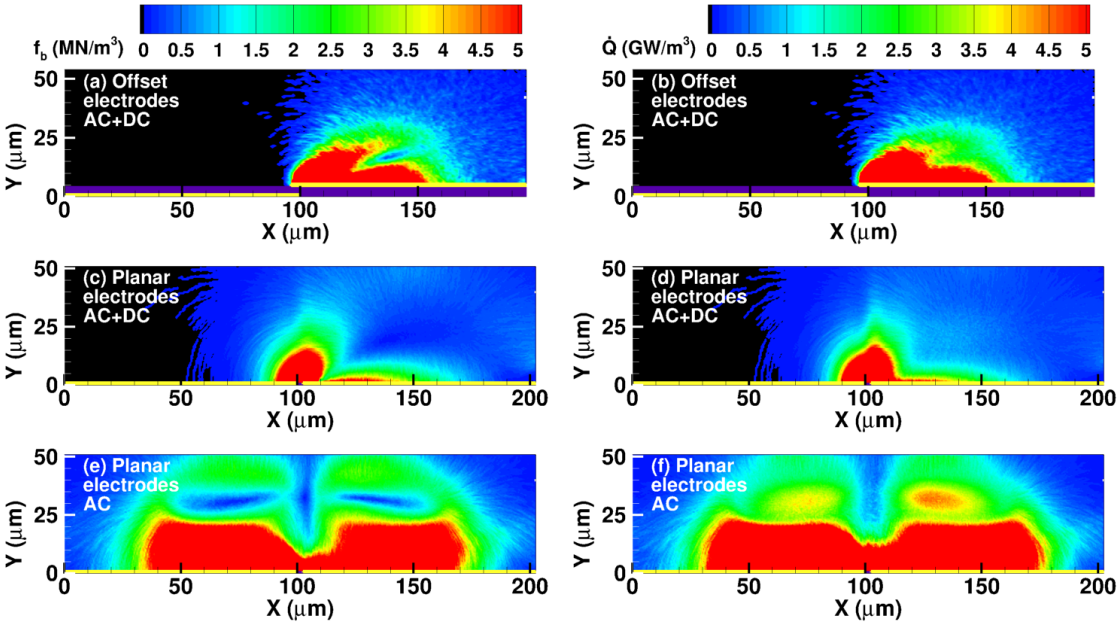

Figure 4.10. Comparison of momentum and energy transferred to the gas at 1 GHz for (a),(b) 325 V_{p-p}, -162.5 V_{dc}, (c),(d) 275 V_{p-p}, -137.5 V_{dc}, and (e),(f) 275 V_{p-p}, 0 V_{dc}.

4.2.3 Effect of Secondary Electron Emission

For the results presented in the previous sections, the secondary electron emission coefficient, γ is taken as 0.001 in accordance with previously published research [74, 85]. Also, for surface DBDs on the mm-scale, humidity reduces the secondary electron emission coefficient [157] and consequently, a low value of γ is chosen in order to ensure that the plasma properties are not overestimated for the feasibility studies presented here.

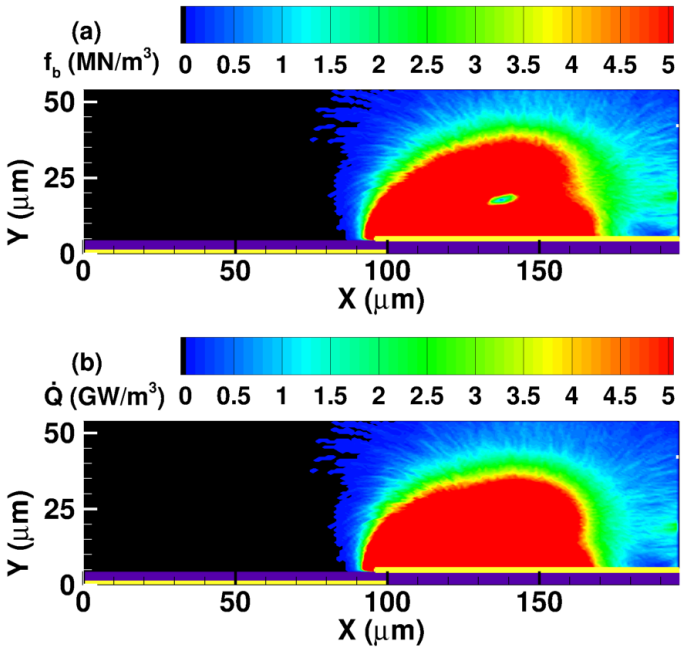

Figure 4.11. Momentum and energy source terms for the offset electrode FE-DBD at 1 GHz for 325 V_{p-p} input voltage with -162.5 V_{dc} bias for $\gamma = 0.01$.

In order to quantify the effect of a higher secondary electron emission coefficient, PIC/MCC simulations are performed with an order of magnitude higher γ value of 0.01. The resulting source terms for the offset electrode FE-DBD at 325 V_{p-p}, 1 GHz and -162.5 V_{dc} are shown in Figure 4.11. The spatially averaged sources are higher by a factor of 2 when compared to the $\gamma = 0.001$ cases presented earlier and have

values of 3.67 MN/m^3 for the body force and 5.37 GW/m^3 for the heat source. The effect of the higher source terms on the flow actuation in microchannels is explored in Chapter 5.

4.2.4 Field Enhancement Using Carbon Nanostructures

Field enhancement by carbon nanostructures of different types has been observed experimentally and characterized in the literature. Srivastava *et al.* [78] used carbon films having petal like sheets on nickel and silicon substrates deposited using microwave PECVD. These petals displayed high emission current at low electric fields with field emission characteristics which followed the Fowler-Nordheim model [56]. Bhuvana *et al.* [77] observed field enhancement in the vicinity of the growth fibers during the MPCVD of carbon nanosheets or petals from graphitic fibers. Dumpala *et al.* [79] quantitatively characterized the field enhancement due to conical carbon nanotube arrays synthesized using MPCVD and observed their ability to sustain high current densities. They observed maximum field enhancement factors of upto 7600.

Coating the FE-DBD electrode surfaces with carbon nanostructures would significantly reduce the breakdown voltage and provide momentum and energy source terms comparable to those for gold electrodes ($\beta = 50$) shown earlier at much lower input voltages. In order to quantify the reduction in voltage, a field enhancement factor of 1000 is used for FE-DBDs with a work function of 5 eV as in [79]. It is significant to note that the increase in the height of the electrode due to the carbon nanostructure coating has not been accounted for in the simulations. Figure 4.12 shows the momentum and energy source terms produced using a β of 1000 for offset and planar electrode FE-DBDs. For the offset electrode actuator, an input voltage of 50 V_{p-p} with -25 V_{dc} bias at 1 GHz produces a spatially averaged momentum source of 4.94 MN/m^3 and energy source of 6.19 GW/m^3. It is of interest to note that for higher values of β, the y-momentum source dominates the x-momentum source contrary to the trend at lower values of β. This is attributed to the high number of

electrons being field emitted normal to the electrode surface, all of which contribute to the y-component. The power at the electrode for this device is 4.18 W/cm or 418 W/cm^2, which is high due to the high current density resulting from the increased field emission even though the input voltage is an order of magnitude lower.

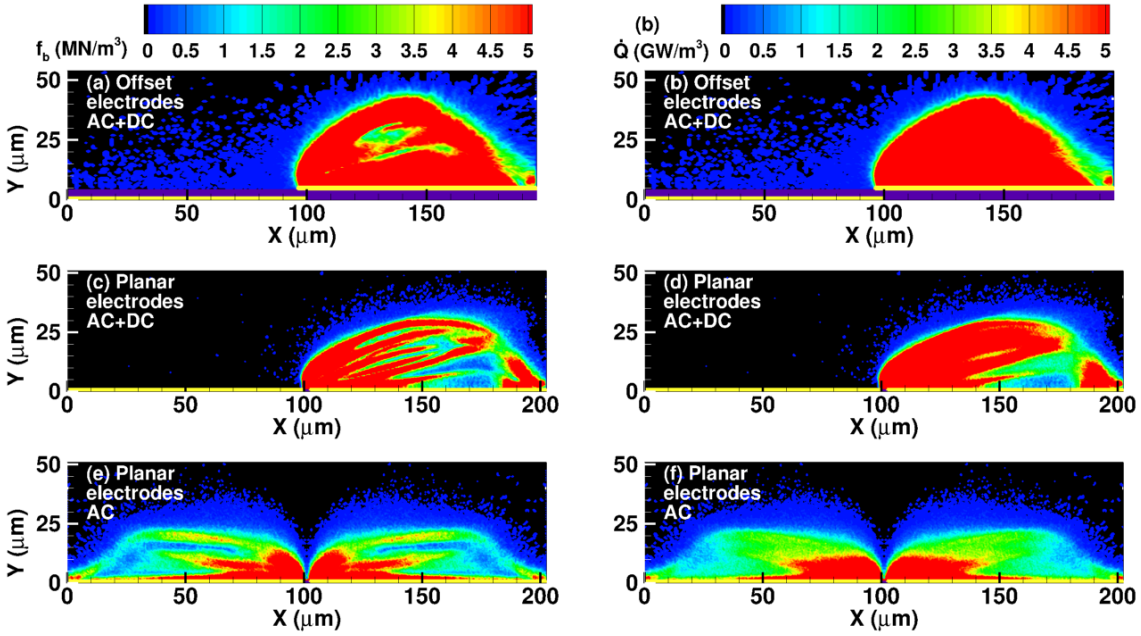

Figure 4.12. Cycle averaged (a) momentum and (b) energy transferred by the plasma generated by carbon nanostructure coated electrodes (β = 1000) to the gas at 1 GHz for (a),(b) 50 V_{p-p}, -25 V_{dc}, (c),(d) 30 V_{p-p}, -15 V_{dc}, and (e),(f) 30 V_{p-p}, 0 V_{dc}.

The carbon nanostructure coated planar electrode FE-DBDs are operated with an input voltage of 30 V_{p-p} at 1 GHz. Figures 4.12 (c) and (d) show the cases for a DC bias of -15 V. This results in average momentum and energy source values of 2.13 MN/m^3 and 2.37 GW/m^3, respectively. The power is 6.67 W/cm or 667 W/cm^2. When there is no DC bias applied, the momentum source as shown in Figure 4.12 (e) produces an average value of 1.43 MN/m^3 all of which is in the y-direction. The energy source is shown in Figure 4.12 (f) and has an average value of 1.40 GW/m^3. The power consumed once again has a high value of 8.85 W/cm or 884.6 W/cm^2.

Thus, nanostructure coated electrodes indicate promising potential for field emission aided flow actuation with at very low operational voltages on the order of tens of volts. The more pronounced y-momentum source and higher heat source value due to the nanostructure enhanced field emission for offset electrode FE-DBDs make its characteristics very similar to the planar electrode FE-DBD without a DC bias. These devices are applied for microchannel flow actuation and microcombustion in Chapter 5.

5. FE-DBD ASSISTED FLOW ACTUATION AND MICROCOMBUSTION

This chapter couples the momentum and energy sources obtained from the PIC/MCC simulations presented in Chapter 4 with CFD simulations to actuate flow in microchannels. A simple theoretical model based on Poisuille flow is presented as a first step in the analysis and compared to the CFD results. The feasibility of initiating and sustaining microcombustion using the momentum and heat imparted by the plasma is evaluated.

5.1 Theoretical Model for Plasma Flow Actuation in Microchannels

The momentum imparted by the plasma to air is modeled as a source term in the Poiseuille flow analysis. Figure 5.1 shows the schematic for the analysis where a body force, f_b', is uniformly applied across the entire length of the channel, L_c, up to a distance of y_b from the walls. The height of the channel is h and a uniform pressure gradient of dp/dx is applied. In reality, a plasma actuator along the wall imparts a body force, f_b, to the flow over discrete lengths of L_b and not over the entire channel length. If N_{DBD} actuators are used, the relation between the body force terms is given by:

$$N_{DBD}|\mathbf{f_b}|y_b L_b = f_b' y_b L_c. \tag{5.1}$$

Assuming steady, incompressible, irrotational flow, no pressure gradient in the y-direction, and neglecting gravity, the continuity and momentum conservation equations for the microchannel flow are given by:

$$\frac{\partial u}{\partial x} + \frac{\partial v}{\partial y} = 0 \tag{5.2}$$

$$\rho u \frac{\partial u}{\partial x} + \rho v \frac{\partial v}{\partial y} = -\frac{\partial p}{\partial x} + \frac{\partial}{\partial y}\left(\mu\left(\frac{\partial v}{\partial x} + \frac{\partial u}{\partial y}\right)\right) + f_b' \tag{5.3}$$

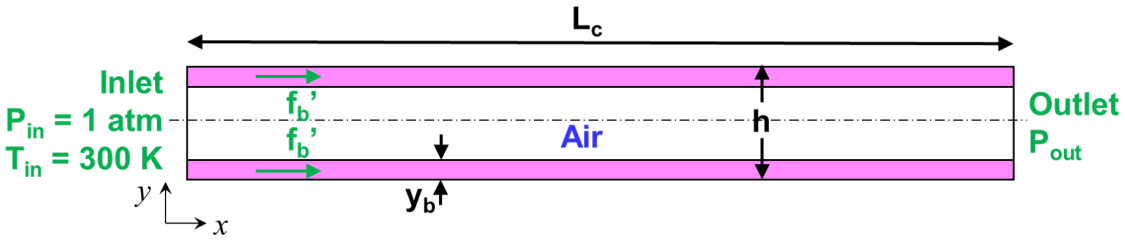

Figure 5.1. Schematic of the microchannel setup for the theoretical analysis with uniformly distributed body force along the entire length of the channel, L_c and up to a height of y_b from the walls in a channel of height h.

where, u, v, p, ρ and μ are the x-velocity, y-velocity, pressure, density and viscosity of air. Assuming fully developed flow, $v = 0$. The body force is applied upto a distance of y_b from the wall. This reduces Equations 5.2 and 5.3 for half the channel to:

$$\mu\frac{\partial^2 u}{\partial y^2} - \frac{dp}{dx} = \begin{cases} -f_b' & \text{for } \; y < y_b \\ 0 & \text{for } \; y_b < y \leq h/2 \end{cases} \tag{5.4}$$

The boundary conditions of no slip at the wall, no shear at the midplane, and continuous and differentiable velocity across the interface at y_b are applied:

$$u(0) = 0 \tag{5.5}$$

$$\left(\frac{du}{dy}\right)_{h/2} = 0 \tag{5.6}$$

$$u(y_b^+) = u(y_b^-) \tag{5.7}$$

$$\left(\frac{du}{dy}\right)_{y_b^+} = \left(\frac{du}{dy}\right)_{y_b^-} \tag{5.8}$$

The solution of Equation 5.4 with the boundary conditions in Equations 5.5-5.8 is given by:

$$u(y) = \begin{cases} \frac{1}{\mu}\left(\frac{dp}{dx} - f_b'\right)\frac{y^2}{2} + \left(-\frac{h}{2\mu}\frac{dp}{dx} + \frac{f_b' y_b}{\mu}\right) y & \text{for } \; y \leq y_b \\ \frac{1}{\mu}\frac{dp}{dx}\frac{y^2}{2} - \left(\frac{h}{2\mu}\frac{dp}{dx}\right) y + \frac{f_b' y_b^2}{2\mu} & \text{for } \; y_b < y \leq h/2 \end{cases} \tag{5.9}$$

The flow rate, Q_{fb} through the half channel is given by:

$$Q_{fb} = 2\int_0^{h/2} u(y)dy = \frac{h^3}{12\mu}\left(-\frac{dp}{dx} + f_b'\left(6\left(\frac{y_b}{h}\right)^2 - 4\left(\frac{y_b}{h}\right)^3\right)\right). \tag{5.10}$$

The gain or enhancement, G in the flow rate is given by:

$$G = \frac{Q_{fb} - Q}{Q} = \frac{f_b' \left(6 \left(\frac{y_b}{h}\right)^2 - 4 \left(\frac{y_b}{h}\right)^3\right)}{-\frac{dp}{dx}}. \tag{5.11}$$

Based on Equation 5.11, the gain is inversely proportional to the Reynolds number, Re, because Re is directly proportional to the pressure gradient.

It is also evident from Equation 5.11 that flow can be actuated without the presence of a pressure gradient. In other words, the microchannel with FE-DBDs along the wall acts a micropump. Therefore, the pumping effect can be better described quantitatively by a normalized pressure difference induced by the body force given by:

$$\frac{\Delta p_b}{p_{ref}} = \frac{N_{DBD} f_b L_b y_b}{p_{ref} h} \tag{5.12}$$

where, the reference pressure $p_{ref} = 1$ atm and Δp_b is the equivalent pressure difference due to the plasma-gas momentum transfer.

5.2 Numerical Model

Although the theoretical model can provide an estimate of the pumping effect produced by the FE-DBDs, the assumptions of fully developed, incompressible and irrotational flow are not valid in the actual flow of air in microchannels. The heat imparted by the plasma to the gas is not taken into account and in reality the FE-DBDs are present in discrete locations and not continuously distributed along the walls of the microchannel. The source terms are also not uniform in the plasma actuation region, but display profiles as shown in Figure 4.10. These factors are accounted for by using Computational Fluid Dynamics (CFD) to study the flow pumping, mixing, and heating through the microchannels.

The momentum and energy source profiles are coupled with the Navier-Stokes equations to model FE-DBD flow actuation in microchannels as shown in Figure 5.2. Since Kn for for a microchannel of height 0.5 mm is 0.0001 for air at atmospheric pressure, the continuum approach of Navier-Stokes equations is used to simulate the

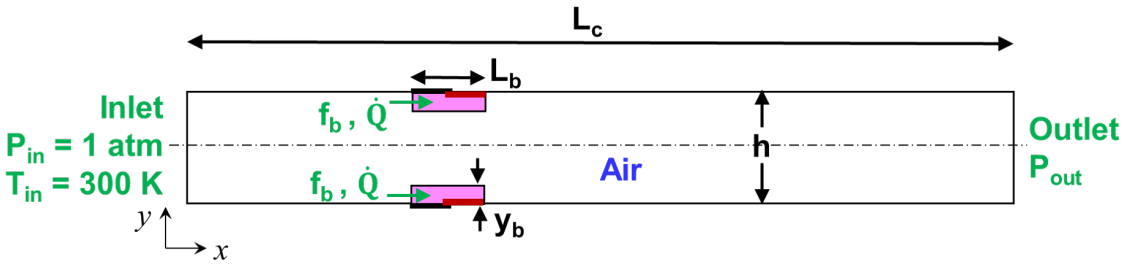

Figure 5.2. Example of the modeling setup and boundary conditions for discrete FE-DBD aided flow actuation in a microchannel of length L_c and height h using CFD. The plasma flow actuation occurs in discrete regions of length L_b and height y_b.

plasma actuated flow. A commercial CFD solver, ANSYS Fluent, is used to model the compressible, laminar, steady flow of air through the 2D channel. The Semi-Implicit Pressure Linked Equations (SIMPLE) algorithm [158] is used to solve the conservation equations and constitutive relations given by:

$$\nabla \cdot (\rho \vec{\mathbf{v}}) = 0 \tag{5.13}$$

$$\nabla \cdot (\rho \vec{\mathbf{v}})\, \vec{\mathbf{v}} = -\nabla p + \nabla \cdot \left(\mu \left(\nabla \vec{\mathbf{v}} + \nabla \vec{\mathbf{v}}^T - \frac{2}{3} \nabla \cdot \vec{\mathbf{v}} I \right) \right) + \vec{\mathbf{f}_b} \tag{5.14}$$

$$\nabla \cdot \left(\vec{\mathbf{v}} \left(\rho e + \rho \frac{|\vec{\mathbf{v}}|^2}{2} + p \right) \right) = -\nabla \cdot (k \nabla T) + \dot{Q} \tag{5.15}$$

where, ρ is the fluid density, $\vec{\mathbf{v}}$ is the velocity vector, p is the pressure, I is the identity vector, e is the internal energy, k is the thermal conductivity and T is the gas temperature. The viscosity coefficient, μ, is computed based on the Sutherland viscosity model given by:

$$\mu = \mu_{ref} \left(\frac{T}{T_{ref}} \right)^{3/2} \frac{T_{ref} + S}{T + S} \tag{5.16}$$

where, the effective temperature, $S = 110.56$ K for air. The momentum and energy sources, f_b and $\dot{Q}$, are computed from PIC/MCC based on Equations 4.5 and 4.6 and their cycle-averaged values are coupled with the conservation equations because the bulk flow does not react instantaneously to the sources.

Initial guesses of constant pressure and zero velocity are used to solve the 2D momentum conservation equations given by Equation 5.14, with the source term obtained from PIC/MCC, in order to obtain intermediate values of velocities. These intermediate velocities do not satisfy the continuity equation, but generate a mass source. The pressure is corrected in order to annihilate the mass source and this is done by solving the continuity equation in Equation 5.13. The pressure correction is used to correct the intermediate velocities. The density is updated due to pressure changes. The new velocities, density and pressure are used in the energy conservation Equation 5.15, with the heat source term obtained from PIC/MCC, to compute the temperature. The viscosity is computed from the Sutherland viscosity model given by Equation 5.16. The new values of pressure and velocities are used as initial values and the procedure is repeated till a convergence of residuals is obtained. The Reynolds number at the channel outlet is computed as:

$$Re_{out} = \frac{|\vec{\mathbf{v}_{out}}|h}{\nu_{out}} \tag{5.17}$$

where, $|\vec{\mathbf{v}_{out}}|$ is the average magnitude of the velocity at the outlet, h is the channel height, and ν_{out} is the average kinematic viscosity at the outlet.

The inlet of the microchannel is modeled at 1 atm pressure and 300 K temperature. The walls are adiabatic with the no slip boundary condition. Grid convergence studies are performed for a 1.5 mm long channel of height 0.5 mm. The grid is composed of 15000 cells with greater refinement closer to the walls. The maximum deviation in the maximum temperature in the channel is 2.1% and the average outlet velocity is 1.3% when the number of cells is increased by 100% to 30000. Consequently, the refinement level of the grid with 15000 cells is for all the calculations presented here.

5.3 Microchannel Flow Actuation

5.3.1 Effect of Reynolds Number

CFD simulations are performed to analyze the performance of FE-DBD actuation in a microchannel with pressure gradient using (a) uniform momentum source distribution (spatially averaged from offset electrode PIC/MCC results) at discrete locations (CFD - Discrete f_b) as shown in Figure 5.2 and (b) uniform momentum source distribution (obtained from Equation 5.1) all along the microchannel (CFD - Continuous f_b) as shown in Figure 5.1. The simulation setup for this involves a 2 cm long microchannel of height 100 μm. The inlet pressure is maintained at 1 atm. The Reynolds number is varied by changing the outlet pressure as listed in Table 5.1. This changes the pressure gradient dp/dx. These simulations for varying outlet pressure only consider the momentum sources from the PIC/MCC simulations and not the heat source so as to be comparable to the theory presented in Section 5.1. In addition, the simulations with uniform body force distribution along the microchannel assume incompressible flow. The discrete actuator centers are separated by 0.6 mm in the x-direction with the first actuator center at 0.5 mm from the inlet.

Table 5.1. Flow conditions for the simulations performed for a 2 cm long and 100 μm tall microchannel for $\Delta p/p_{ref} = 0.8\%$.

Outlet pressure [Torr]	Re
722	75
684	143
646	205
608	262
570	356
532	432

The percentage gain in the flow rate, $G = 100(Q_{fb}/Q - 1)$ is computed using Equation 5.11. The numerical results which consider discrete actuators of length $L_b = 196$ μm and height $h_b = 50$ μm are compared with the theoretical results. The flow rate enhancement is inversely proportional to the Reynolds number as shown in Figure 5.3 for both numerical (continuous and discrete) and theoretical results. This indicates that the FE-DBD configuration considered is extremely useful under low Re, where viscous losses are high.

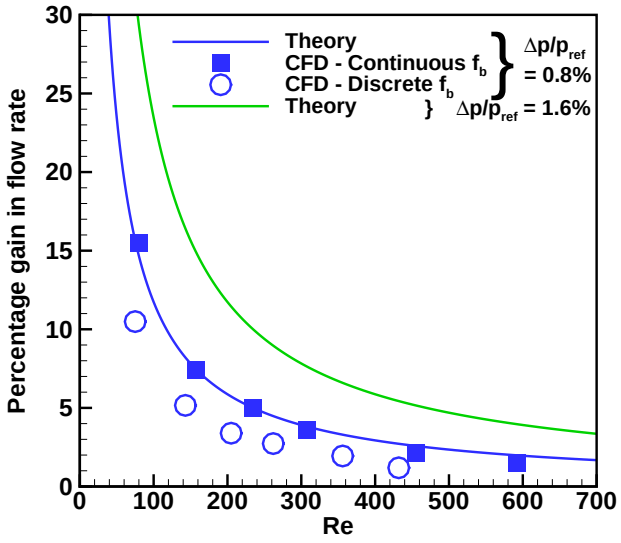

Figure 5.3. Theoretical and numerical flow rate enhancement as a function of Reynolds number for $L_c = 2$ cm and $h = 100$ μm.

The good agreement of 'CFD - Continuous f_b' with theory indicates that the theoretical analysis is sufficient if the FE-DBD actuators are closely placed along the channel to create a continuous body force under incompressible conditions. Theoretical results clearly show that doubling the number of actuators almost doubles the percentage gain in flow rate. However, it is important to note that theory is more than 50% higher in comparison to simulations with discrete f_b, varying from 62% at $Re = 75$ to 162% at $Re = 432$. Therefore, for discrete actuation, which is

more realistic in terms of power consumption, CFD simulations are required as analytical estimates are far off from the reality. The compressibility of the flow and heat imparted by the plasma must also be accounted for in the CFD simulations to realistically evaluate the feasibility of FE-DBD flow actuation.

5.3.2 Plasma-Flow Interaction

The theoretical analysis for plasma flow actuation indicates that the gain in the flow rate increases with decreasing Reynolds number. In other words, as the channel height is reduced, the effect of the plasma actuation becomes more prominent. Also, as the number of actuators used increases, the flow is actuated over a larger region and thereby, the gain in the flow rate is higher. In this section, CFD simulation results for microchannel flow actuation coupled with spatially non-uniform momentum and energy source profiles as determined from the PIC/MCC simulations are presented. The microchannels simulated here are of length 1.5 mm and height 0.5 mm. The inlet of the channel is maintained at atmospheric pressure and no external pressure gradient is applied between the inlet and the outlet. The flow is driven from the inlet to the outlet purely by the directional momentum transfer from the plasma. The only exception to this is the case with planar electrode FE-DBDs without DC bias as will be explained subsequently.

Figure 5.4 shows the microchannel flow velocity and temperature contours using the offset electrode FE-DBD source profiles shown in Figures 4.10 (a) and (b). Two FE-DBDs are used in all cases with different arrangements, and their locations are indicated by the source term coupling region represented by the black rectangles. For the case in Figures 5.4 (a) and (b), the FE-DBDs are placed symmetrically on the top and bottom walls at 0.5 mm from the channel inlet. The maximum temperature and velocity of the flow are 514 K and 29.1 m/s respectively. However, the high temperature location is very small and this arrangement is useful when relatively uniform pumping with low vorticity and preheating of the gases are required.

Figures 5.4 (c) and (d) show the flow actuation with both FE-DBDs along the bottom wall separated by 0.5 mm. The maximum temperature and velocity here are 633.6 K and 29.1 m/s respectively. The heating is non-uniform in the channel, but reaches a higher value which is useful for ignition purposes. Although the maximum velocity is the same as the case with symmetric FE-DBDs, the high vorticity induced in the top half of the channel leads to a much lower velocity at the outlet. Figures 5.4 (e) and (f) show a staggered arrangement of FE-DBDs along the top and bottom walls of the microchannel. The flow actuation is very similar to the symmetric FE-DBD arrangement with a maximum temperature of 521.1 K and maximum velocity of 29.1 m/s. However, this arrangement could provide high vorticity if used in shorter microchannels. It is desirable in micromixing applications where high heating of the flow is not required.

The sources generated by planar electrode FE-DBDs with a DC bias input as shown in Figures 4.10 (c) and (d) are applied symmetrically for flow actuation on the top and bottom walls and the velocity and temperature contours are shown in Figure 5.5. Since the y-component of the momentum source is higher for the planar electrode devices than the offset electrode devices, high vorticity is induced in the microchannel. This leads to better mixing of the flow and the temperature profile at the outlet is very uniform. The maximum temperature and velocity have lower values of 411.1 K and 14.2 m/s indicating that more concentrated f_b and $\dot{Q}$ are more desirable to reach higher flow velocities and temperatures when compared to more spread out source distributions with similar average values.

Figure 5.6 shows similar results as the previous case, except for planar electrode actuators without a DC bias. In this case, since there is no effective flow pumping in the x-direction, a velocity of 0.01 m/s is provided at the inlet. Due to the high vorticity, the flow is mixed well with a uniform temperature profile at the outlet. Since the velocity is very low with a maximum value of just 2.7 m/s, the residence time of the flow in the channel is much longer than the other cases, which leads to much higher temperatures overall with a maximum value of 4925.6 K. This temperature is

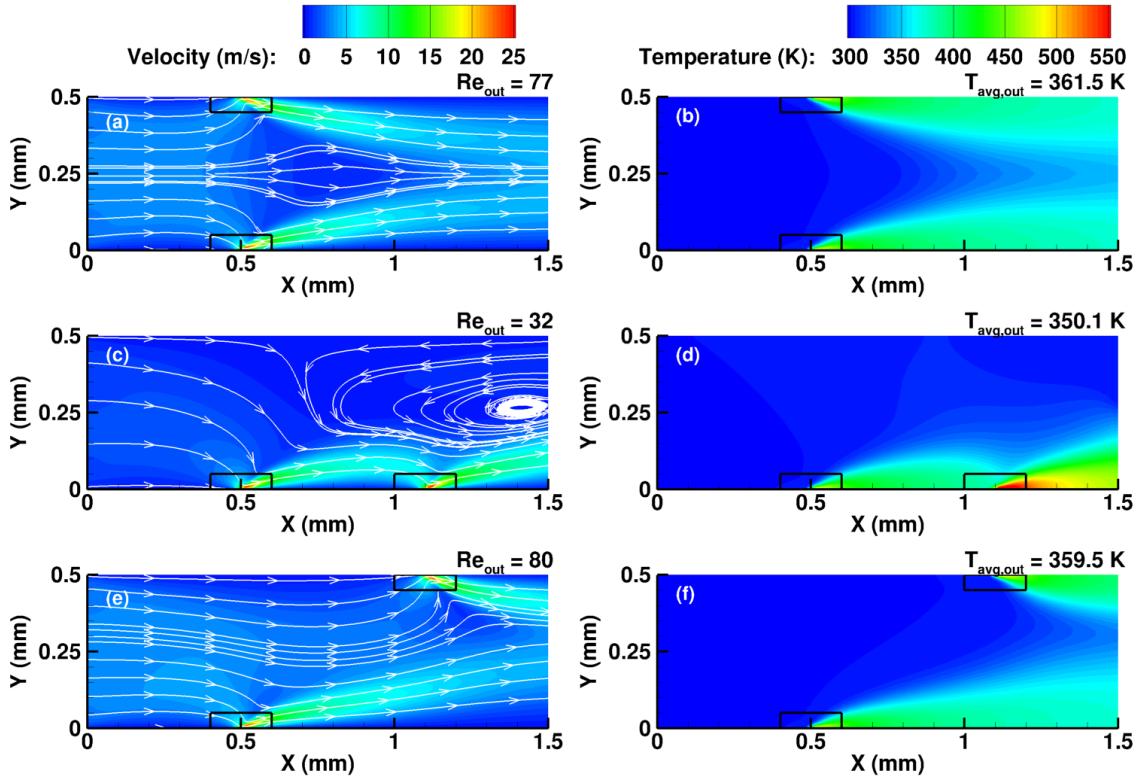

Figure 5.4. Velocity and temperature contours in microchannels with L_c = 1.5 mm, h = 0.5 mm actuated by 2 offset electrode actuators with 325 V_{p-p} and -162.5 V_{dc} for different arrangements. Black rectangles indicate regions actuated by the plasma.

high enough to ignite most fuel-air mixtures and the best application for these devices are as igniters or preheaters.

Different types of actuators and input conditions can be used in conjunction with one another to product the desired effects. One such example is shown in Figure 5.7 where offset electrode actuators are placed closer to the inlet of the channel to pump the flow towards the outlet and the planar electrode actuators with no DC bias are used to increase the temperature and provide better flow mixing. The maximum temperature is 1413 K, which is high enough to ignite hydrogen-air mixture, and the average x-velocity at the outlet is 3.6 m/s. The actuator configurations used can be

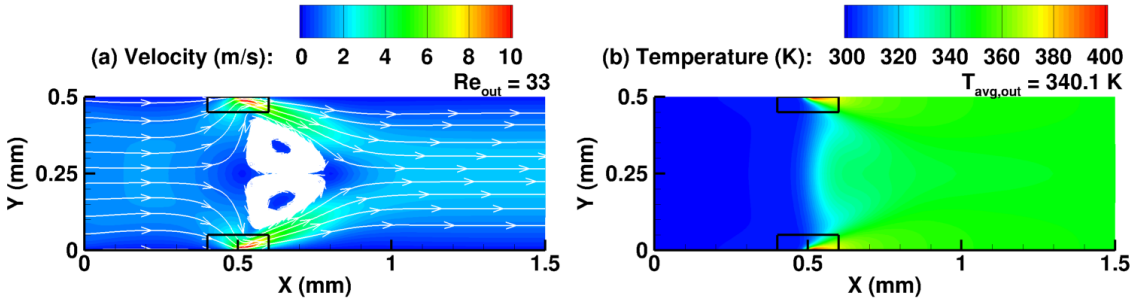

Figure 5.5. (a) Velocity and (b) temperature contours in a microchannel with $L_c = 1.5$ mm, $h = 0.5$ mm actuated by 2 planar electrode actuators with 275 V_{p-p} and -137.5 V_{dc}. Black rectangles indicate regions actuated by the plasma.

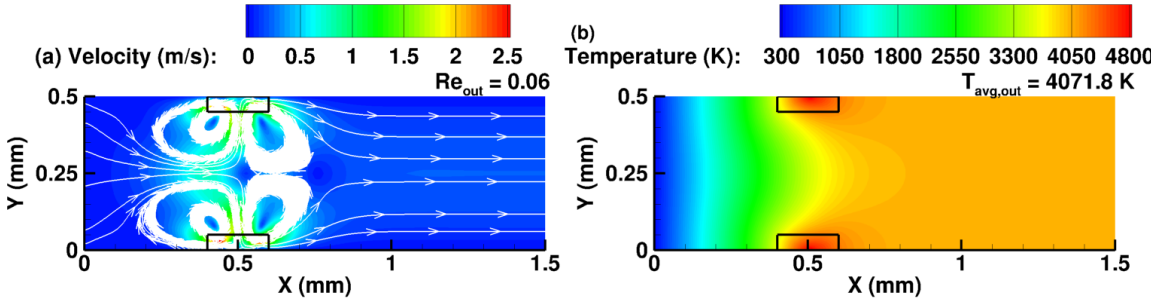

Figure 5.6. (a) Velocity and (b) temperature contours in a microchannel with $L_c = 1.5$ mm, $h = 0.5$ mm actuated by 2 planar electrode actuators with 275 V_{p-p} and no DC bias. Black rectangles indicate regions actuated by the plasma.

catered to each application and can be switched on or off depending on the specific requirement at different instances of time. Moreover, the momentum and heat sources can be tuned based on the actuator input voltage to increase or decrease the velocity and temperature.

The flow actuation in this 1.5 mm long, 0.5 mm tall microchannel is simular to the T-shaped micropump considered by Wang *et al.* [73] in terms of L_c/h. The exit velocity of 3.6 m/s using 4 FE-DBDs is comparable to their 3.1 m/s using 5 plasma

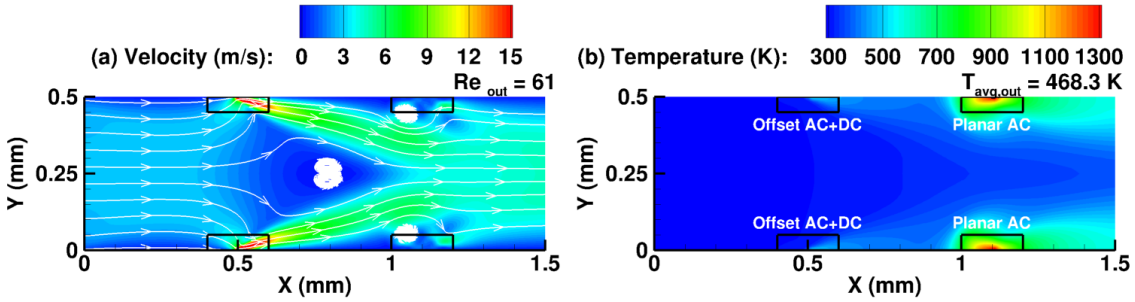

Figure 5.7. (a) Velocity and (b) temperature contours in a microchannel with $L_c = 1.5$ mm, $h = 0.5$ mm actuated by 2 offset electrode actuators with 325 V_{p-p} and -162.5 V_{dc} in conjunction with 2 planar electrode actuators with 275 V_{p-p} and no DC bias. Black rectangles indicate regions actuated by the plasma.

actuators. The microchannel proposed here leads to a flow rate of 107.63 ml/min/mm which is about twice that of the plasma micropump [73] with 25% lower peak voltage.

Simulations are performed to evalute the effect of microchannel length on the FE-DBD flow actuation. Figure 5.8 shows actuation similar to that in Figure 5.4 (a) and (b) in a microchannel of length 3 mm. The channel height is the same and FE-DBDs are placed at the same location of 0.5 mm from the inlet. Here, the flow is fully developed by $x = 1.8$ mm unlike the 1.5 mm channel where the flow is not fully developed even at the outlet. This can be clearly seen in Figure 5.9 which compares the velocity profiles at the outlet for the two cases. The highest velocity in this case is 29 m/s which is higher than the short channel, but the maximum temperature is 489.8 K which is lower than the short channel case. The vorticity induced by the actuators is higher for the long channel.

The average exit velocity for the long channel is 2.6 m/s which is lower than that for the short channel which is 3.3 m/s. This can be attributed to the greater viscous losses beyond the FE-DBD actuation region in the case of the long channel. The viscous dissipation also increases the average exit temperature from 361.5 K for the short channel to 370.2 K for the long channel.

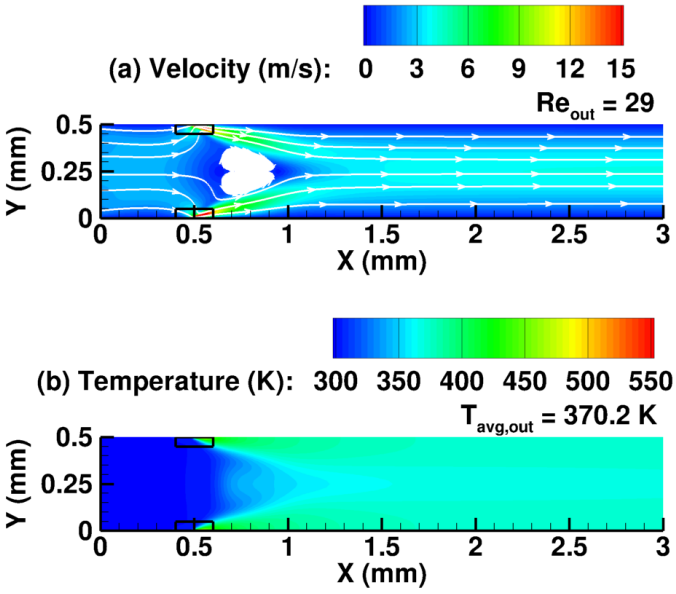

Figure 5.8. (a) Velocity and (b) temperature contours in a microchannel with $L_c = 3$ mm, $h = 0.5$ mm actuated by 2 offset electrode actuators with 325 V_{p-p} and -162.5 V_{dc} at 1 GHz. Black rectangles indicate regions actuated by the plasma.

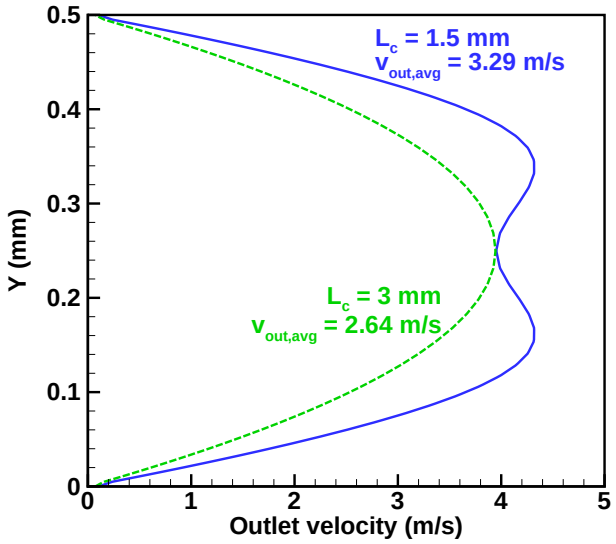

Figure 5.9. Effect of channel length on the outlet velocity profile for a microchannel of height 0.5 mm actuated using 2 offset electrode actuators with 325 V_{p-p} and -162.5 V_{dc} at 1 GHz.

5.3.3 Plasma and Flow Coupling

The simulations presented in the previous section only perform a one way coupling between the plasma and the fluid where the plasma affects the fluid by means of momentum and energy sources, but the fluid solution is not coupled back to the plasma. The fluid can couple with the plasma in two ways namely, velocity and temperature. The velocities induced by the plasma are very small and the Reynolds numbers in the microchannels are <100. The flow is laminar and thus, the effect of this small flow velocity on the plasma properties may be neglected. In order to quantify the effect of higher gas temperature on the plasma, PIC/MCC simulations are performed for the offset electrode FE-DBD for 325 V_{p-p} input with -162.5 V_{dc} bias at 1 GHz at higher gas temperatures. For the plasma-flow coupling shown in Figure 5.4 (d), the average gas temperature in the region actuated by the FE-DBD located at 1.1 mm is 520 K. Figure 5.10 shows the momentum and energy sources imparted by the plasma to the neutral gas at a gas temperature of 520 K. Increasing the gas temperature by 73% increases the spatially averaged momentum source from 1.77 MN/m^3 to 2.39 MN/m^3 by 35%. The increase in the spatially averaged heat source is 42% from 3.13 GW/m^3 to 4.45 GW/m^3.

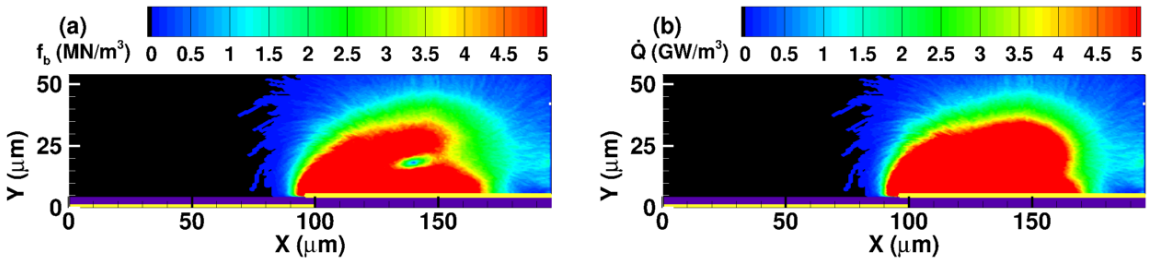

Figure 5.10. (a) Momentum and (b) energy sources for an offset electrode actuator with 325 V_{p-p} and -162.5 V_{dc} at 1GHz simulated at gas temperature of 520 K.

However, when these source terms are coupled to the flow in the microchannel, the effect of the higher source terms translate to much lower impact on the flow properties.

The microchannel velocity and temperature contours for the source terms computed at 520 K are shown in Figure 5.11. the maximum temperature in the microchannel increases by 13% from 633.6 K to 714.3 K. The increase in average temperature and velocity at the outlet are lower than this. When the neutral gas temperature in the PIC/MCC simulations is increased to 1000 K, the momentum and heat source terms increase by just 13% and 15% respectively from the corresponding values at 520 K. Along similar lines, their effect on the flow velocity and temperature are expected to be lower. Thus, a deviation of under 15% on average can be expected when two-way coupling between the plasma and fluid simulations is included.

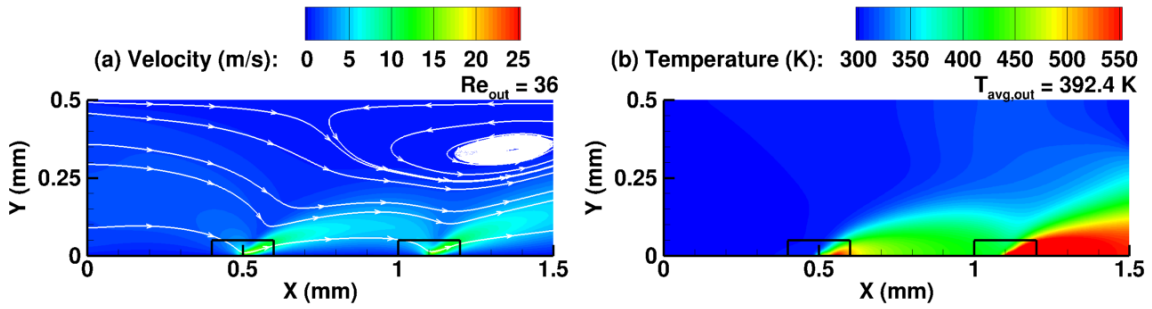

Figure 5.11. (a) Velocity and (b) temperature contours in a microchannel with L_c = 1.5 mm, h = 0.5 mm actuated by 2 520 K offset electrode actuators with 325 V_{p-p} and -162.5 V_{dc} at 1GHz. Black rectangles indicate regions actuated by the plasma.

5.3.4 Effect of Secondary Electron Emission and Field Enhancement

To evaluate the effect of a higher secondary electron emission coefficient of 0.01 on the microchannel flow properties, CFD simulations are performed for a 1.5 mm long, 0.5 mm tall microchannel with the momentum and energy source profiles shown in Figure 4.11. The resulting velocity and temperature profiles are shown in Figure 5.12 where the maximum temperature in the channel is 710.6 K and the average velocity at the outlet is 2.8 m/s. Comparing this to the results in the previous section,

increasing the secondary electron emission coefficient by an order of magnitude from 0.001 to 0.01 increases the average outlet velocity at the channel outlet by 14.3%, the average temperature at the outlet by 7.1%, and the maximum temperature in channel by 12.1%. The qualitative aspects of the flow actuation remain the same with a quantitative deviation of <15%. This is in agreement with the expectation that the secondary electron emission coefficient does not significantly alter the plasma and flow properties in field emission dominated regimes.

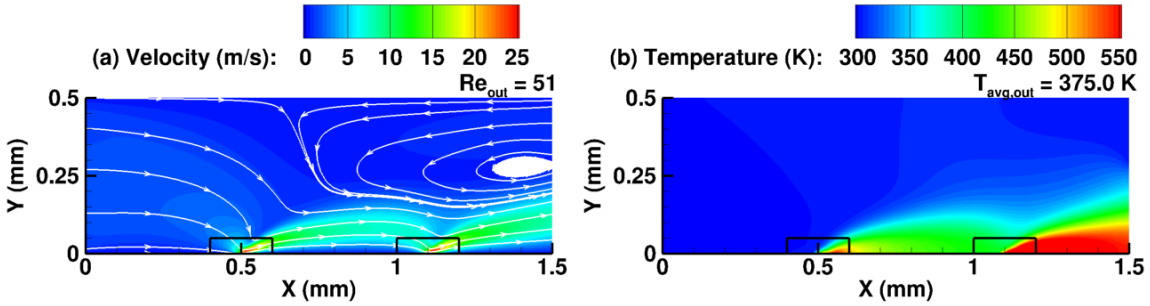

Figure 5.12. (a) Velocity and (b) temperature contours in a microchannel with $L_c = 1.5$ mm, $h = 0.5$ mm actuated by 2 offset electrode actuators with $\gamma = 0.01$, 325 V_{p-p} and -162.5 V_{dc} at 1GHz. Black rectangles indicate regions actuated by the plasma.

Similar computations are performed using the momentum and energy source terms obtained using the higher field enhancement factor of 1000 for electrode surfaces that are coated with carbon nanostructures. The lower voltage requirement and plasma properties of these devices are shown in Chapter 4. Microchannel flow actuation using the nanostructure coated offset electrode FE-DBDs show much lower velocities along the length of the channel and much higher vorticity. This is attributed to the high y-component of the momentum source. The average velocity at the outlet has a 42% lower value of 1.4 m/s when compared to the case with β of 50. The maximum temperature reached in the microchannel is 2367.5 K and is high enough for the auto-ignition of hydrogen-air mixtures. The higher vorticity also leads to better mixing

which can aid complete combustion. The higher temperature in in channel leads to low density of air which reduces the Re by a factor of 4 as seen in Figure 5.13.

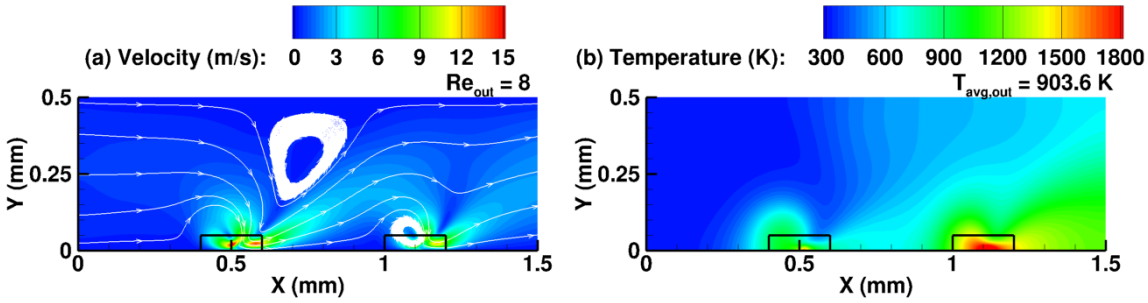

Figure 5.13. (a) Velocity and (b) temperature contours in a microchannel with $L_c = 1.5$ mm, $h = 0.5$ mm actuated by 2 offset electrode actuators with $\beta = 1000$, 50 V_{p-p} and -25 V_{dc} at 1GHz. Black rectangles indicate regions actuated by the carbon nanostructure aided field emission plasma.

5.4 Electrohydrodynamic Effects

Non-equilibrium plasmas find use in a wide variety of aerospace applications, the most common of which are flow control over a wing to prevent flow separation and plasma assisted ignition and combustion (PAI/PAC). Macheret *et al.* [72] studied the EHD effects of weakly ionized plasmas for hypersonic flow control and characterized the effect of EHD forces on fluid flow using an interaction parameter, Z_{EHD}, given by:

$$Z_{EHD} = \frac{e\,(n_+ - n_- - n_e)\,\Delta\phi}{\rho v^2} \tag{5.18}$$

where, e is the elementary charge, n_+, n_- and n_e are the number densities of positive ions, negative ions and electrons respectively, $\Delta\phi$ is the voltage fall across the space charge region, which is the cathode sheath region of a glow discharge, ρ is the flow density and v is the flow velocity through the space charge region. Table 5.2 summarizes the EHD interaction parameter for various types of discharges used for flow actuation and combustion.

Table 5.2. EHD interaction parameter for aerospace plasmas.

Plasma type	**Application**	**Reference**	**Operational voltage [V]**	**Flow velocity [m/s]**	$\mathbf{Z}_{EHD}$
Macroscale DBD	PFA	[63]	2000	15.2	0.14
Macroscale DBD	PFA	[64]	3000 to 5000	0.5 to 4	>2.45
Macroscale DBD	PFA	[68, 69]	3000	10	8.27
Microscale DBD	PFA	[159]	5000	2	6.12
DC Glow	PFA	[160]	1000	668	0.006
Pulsed plasma	PAC	[94]	1000	1552.7	0.572
RF plasma	PAC	[161]	600	10	0.07
NPD (peak ionization)	PAC	[96]	8300	2	1.5×10^{6}
NPD	PAC	[162]	15000	20	2.5
FE-Corona	Cooling	[156, 163]	400	0.25	136
Offset FE-DBD	μC		325	7.23	1.07
Planar FE-DBD	μC		275	4.3	0.30

PFA: Plasma Flow Actuation, PAC: Plasma Assisted Combustion

NPD: Nanosecond Pulsed Discharge, μC: Microcombustion

Corke *et al.* [63] used a single DBD on an airfoil surface for wing flow control at 7000 ft altitude. The average ion number density in the space charge region of a typical glow discharge is on the order of 10^{17} m^{-3} [72]. For the freestream velocity of 15.2 m/s, this actuator produces a Z_{EHD} of 0.14. This value is higher in the region where the flow actuation takes place i.e. within the boundary layer where the flow velocities are lower. Roth *et al.* [64] similarly used the atmospheric glow discharge produced by a series of DBDs to actuate flow on the upper surface of an airfoil. The interaction parameter for each DBD actuator at atmosphere is at least 2.45 even at the highest velocity. Since multiple actuators are used, the total effect of EHD forces increases proportionately. Im *et al.* [68, 69] applied a DBD to manipulate a turbulent boundary layer at a Mach number of 4.7. The temperature and pressure of air were 60 K and 1 kPa respectively, and the wall jet produced by the DBD in

the flow actuation region had a velocity on the order of 10 m/s. Using a typical glow discharge space charge density value of 10^{17} m^{-3} reveals a high interaction parameter value of 8.27 for this device. Zito *et al.* [159] used a microscale DBD for flow control and force inducement. Although this is a microscale DBD, the electrode gap is 10 μm where the field emission effects are negligible. The force induced by the plasma measured using a torsional balance is found to be 3 mN/m at a velocity of 2 m/s in atmosphere. For an electrode width of 100 μm, the interaction parameter produced by the actuator is 6.12. Poggie [160] numerically evaluated the application of DC glow discharges to manipulate high-speed flow. Three-dimensional simulation of a parallel plate DC discharge at 64 Pa and 43 K produced an interaction parameter value of 0.006. In this case, the interaction parameter corresponding to the electromagnetic effects is 3 orders of magnitude higher than that of the electric force, indicating that the manipulation of the flow structure is primarily due to the dissipative heating effects rather than the electric force on the bulk gas.

Byturin *et al.* [94] used high frequency pulsed repetitive discharges for plasma assisted propane-air combustion in a hot wind tunnel. An ion number density of 10^{21} m^{-3} in the streamer produces a Z_{EHD} of 0.572 for each discharge generator in atmospheric air. Leonov *et al.* [161] used RF plasma for the ignition and combustion of ethylene-air in the cavity of a high speed duct. Assuming an ion number density of 10^{17} m^{-3} for a typical RF discharge, the Z_{EHD} has a value of 0.07 in the separation zone behind the wallstep where the actuation takes place. Nanosecond pulsed discharges as described by Pai *et al.* [164] were used by Lefkowitz *et al.* [96] for the ignition of ethylene-air and aviation gasoline-air mixtures in a pulsed detonation engine. The interaction parameter produced at peak ionization has a very high value of 1.5 x 10^6. However, this peak ionization lasts for a very short period of time and is much lower during the rest of the cycle. Nanosecond barrier discharges were also studied by Starikovskii *et al.* [162] to improve the kinetics of alkane oxidation, reduce ignition delay, and initiate deflagration to detonation transition in propane-air mixtures. The velocity ranged from 10 to 120 m/s and voltage ranged from 10 to

21 kV. An average charge separation density of 5 x 10^{17} m^{-3} produces an interaction parameter of 2.5 at 20 m/s and this is higher at lower velocities.

Go *et al.* [156, 163] investigated the feasibility of applying the ionic wind generated by a field emission driven corona discharge for atmospheric air cooling at the microscale. The body force generated here was $\sim 10^7$ N/m^3 over a small distance of 1 μm from the cathode. The velocity of the bulk flow was 0.25 m/s and the driving voltage was 400 V. This produces a high interaction parameter of 135.6. However, the momentum transferred by the discharge generated by this device was found to be ineffective in inducing any significant variation in the flow velocity. This was attributed to the heating and frictional force which mitigated any momentum added to the flow. The interaction parameter defined in Equation 5.18 does not take into account the effect of viscosity. For the FE-DBD simulations presented in this work, the friction and viscous effects for the heated flow are accounted for and the velocity induced by the FE-DBD overcomes these forces at the microscale.

For each FE-DBD actuator operating in atmospheric nitrogen, the voltage is 325 V for the offset electrode configuration and 275 V for the planar. The average flow velocity in the plasma actuation region is calculated based on the results presented in Section 5.3.2. For the offset electrode FE-DBD, the average space charge density i.e., the difference between the ion and electron number densities, is 2.51 x 10^{18} m^{-3} which produces an interaction parameter of 1.07. The planar electrode FE-DBD with an average space charge density of 2.95 x 10^{17} m^{-3} produces an interaction parameter of 0.30. These values indicates promising potential for flow actuation at low input voltages.

Starikovskaia [95] summarized the parameters for various types of plasmas traditionally used for plasma assisted ignition and combustion. Taking the average values of the gas temperature and pressure ranges, the average air density is computed in each discharge. The assumption of quasi-neutrality in the plasma bulk is made, n_- is neglected in the space charge region, and the average value of the voltage range is taken as the potential drop across the space charge region. Using equation 5.18, the

maximum flow velocity through the space charge region at which the EHD effects of the plasma are still significant is calculated. The average values of the voltage and current are used to compute the input power values. Table 5.3 presents the maximum flow velocity for which $Z_{EHD} \geq 0.1$. It is evident that the FE-DBDs, especially with the offset electrode configuration, are limited to the very low flow velocities, but consume very low voltage when compared to most other plasma types. Arc discharges operate at lower voltages, but cannot be used for steady state operation and consume large power due to the high current flowing through the electrodes. The combination of low operational voltage and power requirement of FE-DBDs renders them ideal for application in microcombustors where low flow velocities are encountered.

Table 5.3. Maximum flow velocity for different plasmas to produce significant EHD effects ($Z_{EHD} \geq 0.1$). Parameters taken from [95].

Plasma type	**Density** [**kg/m^3**]	**Voltage** [**V**]	**Power** [**W**]	$n_+ - n_e$ [**m^{-3}**]	v_{max} [**m/s**]
Arc	0.8	50	5000	5 x 10^{21}	707
Glow	0.05	500	2.5	5 x 10^{17}	89
Streamer	0.5	50000	25	5 x 10^{17}	283
DBD	0.4	5000	2.5	5 x 10^{17}	100
Fast ionization wave	0.13	10^5	10^7	5 x 10^{18}	2481
Radio Frequency (RF)	0.04	2500	12.5	1 x 10^{17}	100
Microwave	0.06	5000	2500	5 x 10^{22}	81650
Offset FE-DBD	1.17	325	24/cm^2	2.51 x 10^{18}	23.6
Planar FE-DBD	1.17	275	3/cm^2	2.95 x 10^{17}	7.45

5.5 Microcombustor Concept and Model

Figure 5.14 presents a MEMS microcombustor concept that uses the planar electrode FE-DBDs to ignite and aid in the combustion of hydrogen-air mixtures. The channel is made of quartz and sits atop a silicon bottom plate. The design is based on the microburner concept presented by Mackay *et al.* [85]. The location of the actuators is close to the fuel and oxidizer inlets in order to enhance mixing and increase residence time in the channel. The momentum and energy imparted by the plasma are used to heat and mix the fuel and oxidizer, and the exhaust gases are comprised primarily of environmentally friendly H_2O and N_2.

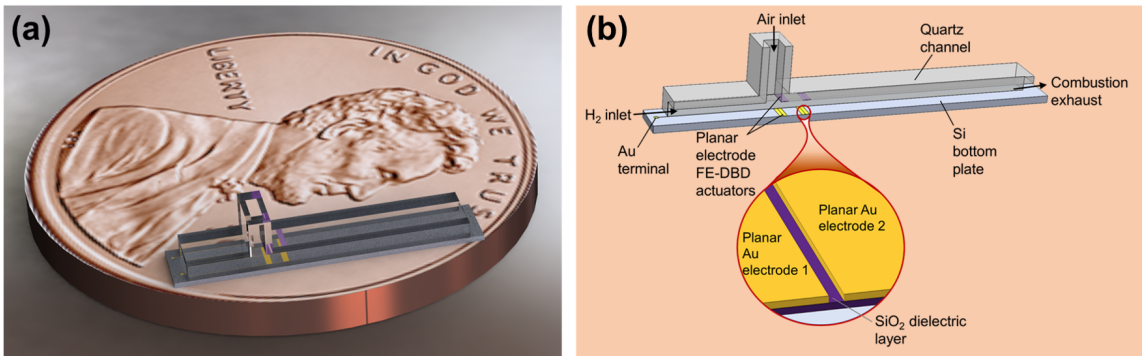

Figure 5.14. H_2-air MEMS microcombustor concept (a) design and (b) sectional view indicating planar electrode actuator setup.

The momentum and energy sources described and shown in Chapter 4 are used to model hydrogen-air combustion using CFD as shown in Figure 5.15. A steady parabolic flow of hydrogen with a centerline velocity, v_0, of 0.25 m/s and temperature of 300 K is introduced at the inlet of the main channel. In order to maintain stoichiometric proportions, a parabolic flow of air with a centerline velocity of 0.53 m/s and temperature of 300 K is introduced at the other inlet, which is perpendicular to the main channel. Heat loss through the quartz walls to ambient air at 300 K is included. The conservation equations given by equations 5.13-5.15 are solved in conjunction with the species transport equation.

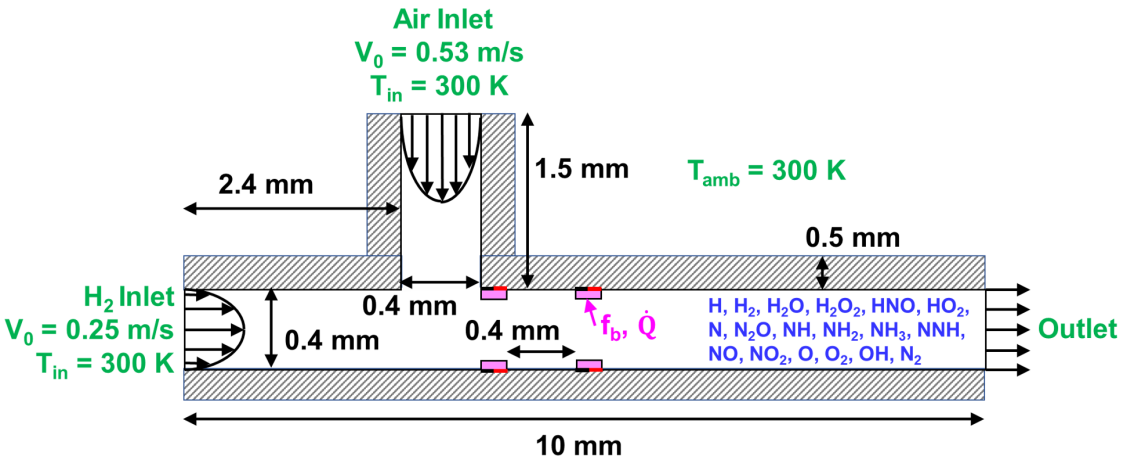

Figure 5.15. Modeling setup and boundary conditions for field emission plasma assisted microcombustion using CFD.

In order to model the combustion chemistry, an 18 species, 70 reaction model is used in the species conservation equation given by:

$$\nabla \cdot (\rho \vec{\mathbf{v}} Y_i) = \nabla \cdot (\rho D_i \nabla Y_i) + R_i \tag{5.19}$$

where, the subscript i refers to the species, Y is the species mass fraction, D is its diffusion coefficient in the mixture, and R is its net rate of production by chemical reactions. The 70 reaction model is obtained by retaining all the chemical reactions involving H, N and O in the GRI-Mech 3.0 combustion mechanism [143] and using the Arrhenius rates from the reaction data set. Of the 53 species in the GRI-Mech 3.0 mechanism, 18 consist of H, O and/or N only and these are indicated in Figure 5.15. The thermodynamic properties for the species are computed based on the NASA Polynomial fit [144]. The transport properties i.e., the viscosities, conductivities and diffusivities of all the species are determined based on kinetic theory [131, 165] using parameters obtained from [144]. It is significant to note that the modification of the combustion mechanism by the charged species is not modeled here and may further contribute to faster ignition and enhanced combustion [95, 98, 99].

A uniform grid with 1,150,000 cells is used to model the flow in the microcombustor. A grid convergence study is performed using grids with number of cells in the range of 287,500 to 4,600,000. The temperature, H_2O mole fraction and velocities are compared for the different grids. The maximum deviation in the properties when the number of cells is increased beyond 1,150,000 is 2.5% and this refinement is thus sufficient for the calculations.

A major challenge to overcome when designing a microcombustor is to ensure that the residence time of the fluid in the chamber is longer than the chemical time required for complete combustion to occur [166]. The planar electrode FE-DBDs without DC bias voltage aid this by creating vortices which reduces the velocity of the fluid directed towards the outlet. They supply heat which is required to ignite the fuel, without providing additional velocity directed towards the channel exit. Here, 4 such actuators are used for the combustion of hydrogen and air.

5.6 FE-DBD Microcombustion Results

The results of the microcombustion simulation are shown in Figure 5.16. The temperature reaches a maximum value of 2990.8 K. This is 611.4 K higher than the adiabatic flame temperature of 2379.4 K for stoichiometric H_2-air mixture at 300 K and 1 atm determined using NASA CEA [167]. The high temperature reached is a result of the additional heat imparted by the plasma to the flow. The average velocity of the products at the outlet is 4.39 m/s. 99.6% of the hydrogen entering the combustor is consumed. Dissociation along the channel length reduces the mole fraction of H_2O from 0.28 near the plasma region to 0.17 at the channel exit. The exhaust is primarily comprised of H_2O and N_2 which account for a total mole fraction of 0.82. Trace amounts of OH, H_2, O_2 H, O and NO account for the remaining exhaust gases. The mole fractions of all the species at the outlet of the microcombustor are summarized in Table 5.4.

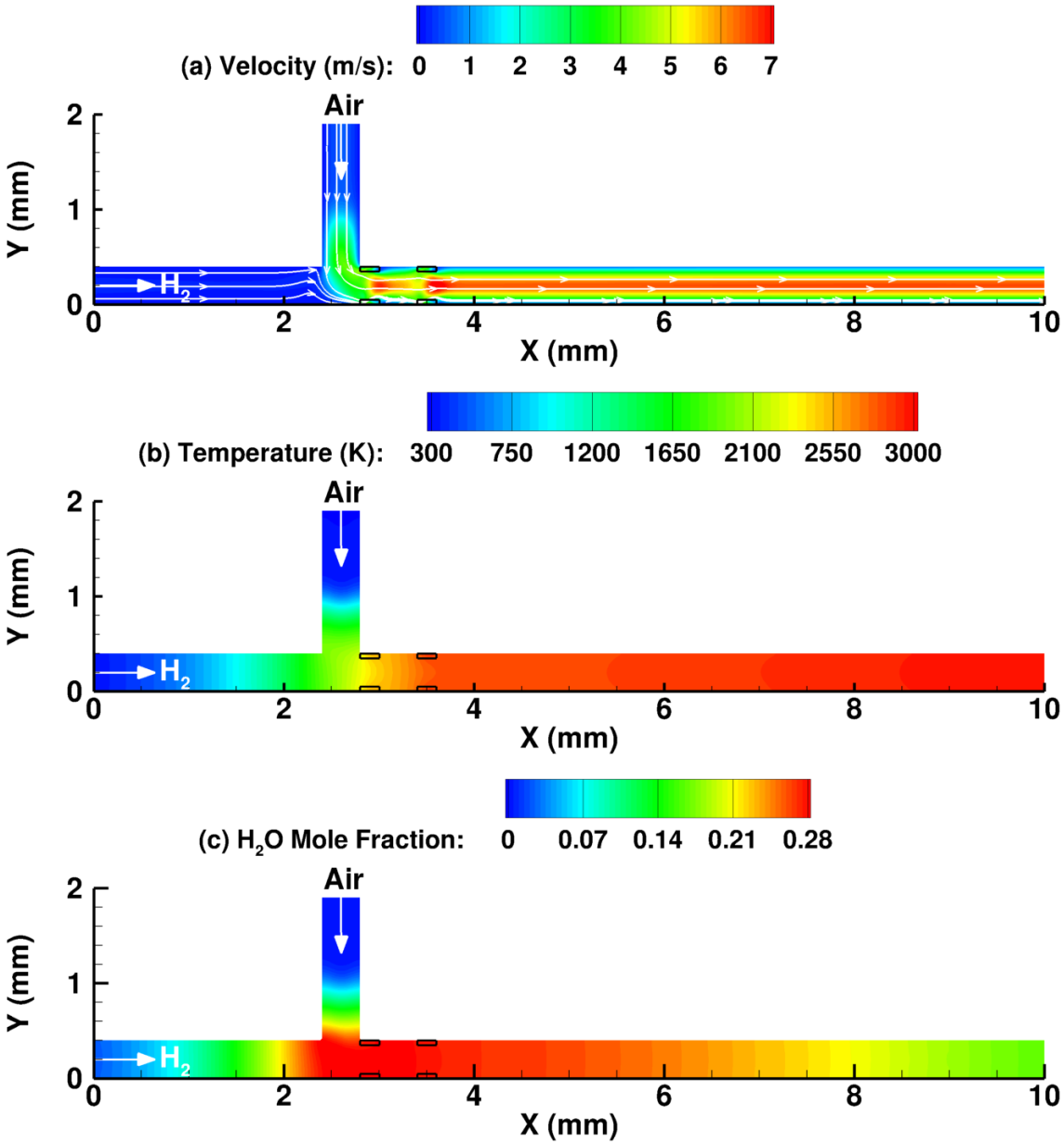

Figure 5.16. (a) Velocity, (b) Temperature and (c) H_2O mole fraction contours in the microcombustor using 4 planar electrode actuators with 275 V_{p-p} and no DC bias. Black rectangles indicate regions actuated by the plasma.

Table 5.4. Average mole fraction of different species at the microcombustor outlet.

Species	**Average exit mole fraction**	**Species**	**Average exit mole fraction**
N_2	0.65	N	8.9×10^{-6}
H_2O	0.17	NO_2	3.7×10^{-6}
OH	0.04	HNO	1.1×10^{-6}
H_2	0.04	N_2O	9.0×10^{-7}
O_2	0.03	NH	8.8×10^{-7}
H	0.03	H_2O_2	5.6×10^{-7}
O	0.02	NH_2	1.1×10^{-7}
NO	0.01	NNH	6.5×10^{-8}
HO_2	1.4×10^{-5}	NH_3	3.9×10^{-8}

This study chiefly explores the contribution of the energy imparted by the plasma to heat the flow and sustain steady-state combustion in the microcombustor. When the actuators are not used, combustion does not occur as seen in Figure 5.17. The temperature of the gases are 300 K along the entire length of the channel and the H_2O mole fraction is 0. When the actuators are used, the heat transferred from the plasma increases the temperature by an order of magnitude and causes autoignition of H_2 in air. Figure 5.17 (a) shows that the heat loss through the channel walls reduces the maximum temperature by 189 K. Figure 5.17 (b) shows that although the outlet temperature is lower when wall heat losses are accounted for, the mole fraction of H_2O is higher because lower temperature leads to lower rate of dissociation of H_2O when compared to the case with adiabatic walls.

The supply of radicals by the plasma required to sustain the chain reactions for combustion are not accounted for. This would reduce the ignition time and improve

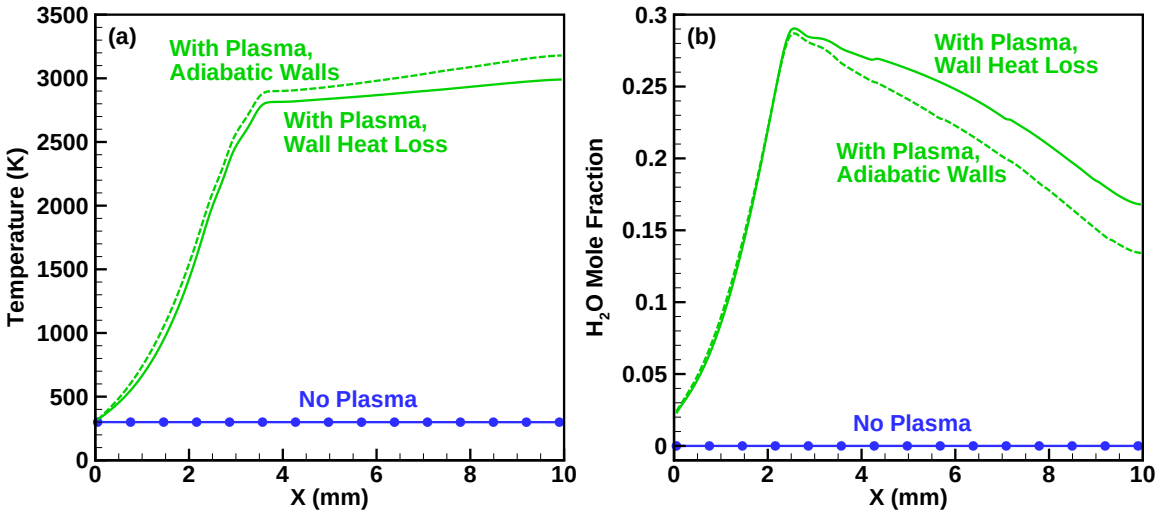

Figure 5.17. Effect of the presence of plasma and the wall heat loss on the (a) temperature and (b) H_2O mole fraction along the centerline of the microcombustor main channel.

the combustion efficiency of the system [95, 98, 99]. The total rate of heat release by all the reactions close to the plasma actuators are shown in Figure 5.18. Most of the heat is released in the vicinity of the flame, which for the present geometry, inlet velocities, and actuator positions is located near the intersection of the microcombustor main channel and the air inlet channel. Based on previous work [168] as well as the simulations shown here, the most important radicals that determine the temperature and velocity are OH, O and H. The reactions with the highest rates that lead to radical formation or heat release are:

R1: $H + O_2 \rightarrow OH + O$

R2: $OH + H_2 \rightarrow H_2O + H$

R3: $2OH \rightarrow O + H_2O$

The total electrical input power to the 4 AC planar electrode actuators is 0.2 W/cm. The power generated by the complete combustion of the hydrogen entering the combustor is 6.63 W/cm. Thus, the total input power to the system is $\mathcal{P}_{input} =$ 6.83 W/cm. The total electrical power consumed by the actuators is just 3% of the

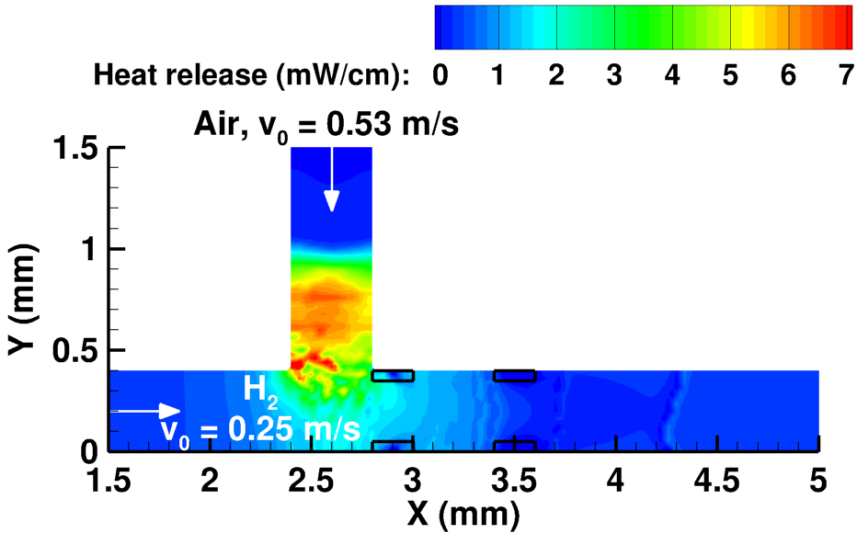

Figure 5.18. Total reaction heat release close to the plasma actuation region.

power released by complete combustion of the fuel. The total power released due to the chemical reactions during combustion can be determined based on the enthalpy of reaction for all the processes occurring in the combustor. The energy released by combustion manifests itself as a combination of chemical, thermal and kinetic energy at the outlet of the microcombustor. A part of the kinetic energy may also be converted to thermal energy due to viscous dissipation. However, since the source of the energy is due to the heat release during the reactions, the total power output of the system is computed as:

$$\mathcal{P}_{output} = -\Delta \left(\rho \sum_{j} \left(Y_j h_j^0 \right) \left(\vec{\mathbf{v}} \cdot \vec{\mathbf{n}} \right) A \right) \tag{5.20}$$

where, h_j^0 is the formation enthalpy of species j, n is the surface normal, and A is the area of the surface. Δ represents the difference in the computed quantity between the outlet and the inlet of the microcombustor. The negative sign exists to account for the negative enthalpy of reaction for exothermic reactions. The total output power for the 2D microcombustor is $\mathcal{P}_{output} = 1.97$ W/cm. This can be increased or decreased based on the application requirement by controlling the number, type, and voltage

input of the FE-DBDs used to actuate the flow. The combustion efficiency of the microcombustor is calculated as the ratio of the total output to the total output power for complete combustion of the fuel and has a value of $\eta_{comb} = 29.7\%$. The efficiency of the microcombustor is determined as the ratio of total output and input powers and has a value of $\eta = \mathcal{P}_{output}/\mathcal{P}_{input} = 28.8\%$.

Figure 5.16 shows that the flame is maintained near the oxygen inlet and not exactly at the location of the plasma actuators. This is because the flame always moves towards the reactants and is maintained as close to the inlet as possible under steady state for the inlet velocities and mole fractions specified. Hence, the heat release occurs in this region. Increasing the velocity at one of the inlets would move the flame further away from that inlet. In order to demonstrate this, a simulation is performed with the same H_2 inlet velocity of 0.25 m/s and a higher air velocity of 0.75 m/s (compared to 0.53 m/s shown earlier). The contour of the total reaction heat release for these conditions is shown in Figure 5.19. The location of the flame and thereby, the region with the highest heat release moves away from the air inlet toward the first FE-DBD location when compared to Figure 5.18.

The operational volatge of FE-DBDs can be significantly reduced by coating the electrodes with carbon nanostructures as shown in Chapter 4. The offset electrode FE-DBDs when coated with nanostructures such that $\beta = 1000$ produce a very high heat source term which is capable to igniting H_2-air mixtures at an operational voltage of just 50 V as shown in Section 5.3.4. The high y-momentum source also increases the vorticity which can effectively mix the fuel and oxidizer in the microcombustor. The high energy transfer and vorticity are the major reasons for using the planar electrode FE-DBD without a DC bias in the MEMS microcombustor. An additional reason is that there is no momentum imparted in the x-direction which helps in increasing the residence time of the gases to ensure complete combustion.

Another method of ensuring a longer residence time of the gas is by providing a small x-momentum in the negative x-direction. This is explored here using the nanostructure coated offset electrode FE-DBDs at 50 V arranged in such a way that the

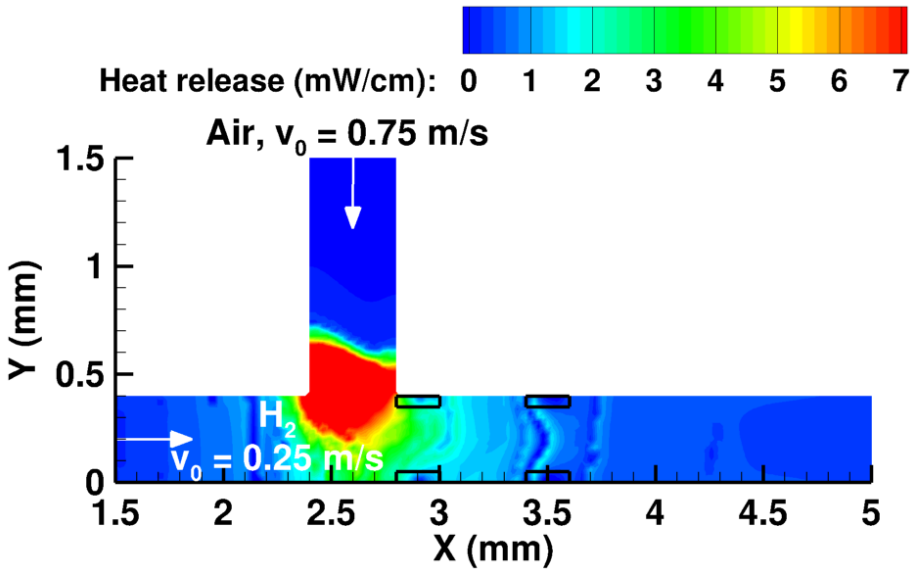

Figure 5.19. Total reaction heat release close to the plasma actuation region for a higher air inlet velocity of 0.75 m/s.

exposed cathode is to the left of the embedded anode. This provides a small pumping effect along -x to the flow along +x, slows down the gases, and creates additional vorticity when coupled with the y-momentum source to ensure better mixing. The results of microcombustion using such an arrangement in shown in Figure 5.20. The maximum temperature in this case is 2468.6 K which is still higher than the adiabatic flame temperature for the mixture, but is lower than the case shown in Figure 5.16. The average velocity of the products at the outlet is 2.97 m/s and the exhaust in this case has a higher average H_2O mole fraction of 0.34 indicating very low dissociation of H_2O along the main channel.

The cause for the low dissociation is explored further in Figure 5.21. The low velocity of the flow due to the negative x-momentum transfer from the FE-DBD actuators leads to low viscous dissipation along the length of the channel. Thus, the temperature is about 500 K lower in the main channel which leads to lower dissociation of H_2O. The total input power to the microcombustor in this case is 23.35 W/cm.

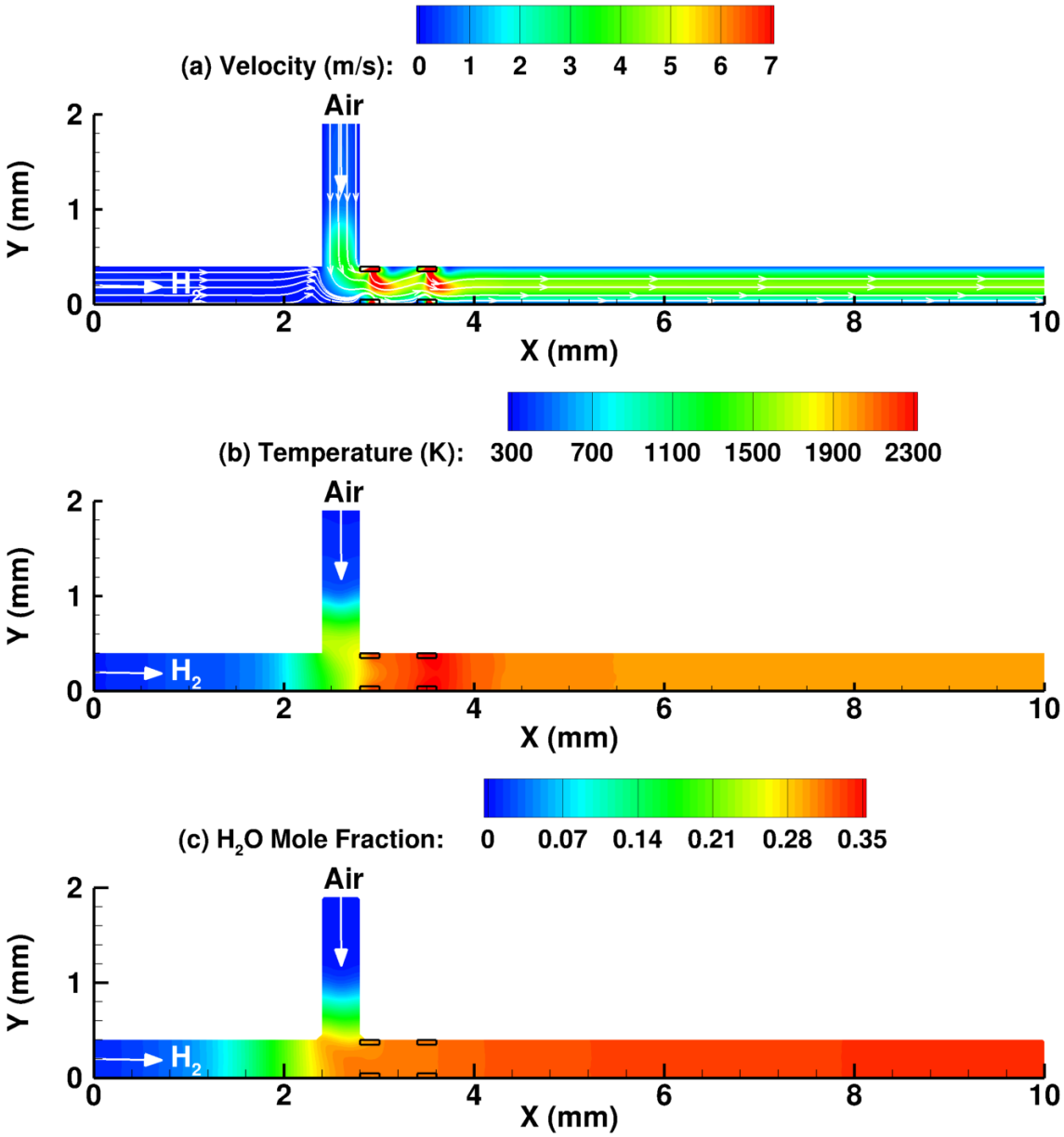

Figure 5.20. (a) Velocity, (b) Temperature and (c) H_2O mole fraction contours in the microcombustor using 4 carbon nanostructure coated offset electrode actuators with 50 V_{p-p} and -25 V_{dc} bias. Black rectangles indicate regions actuated by the plasma.

The output power calculated using Equation 5.20 is 5.11 W/cm. This results in a combustion efficiency of 77.1 %, which is a factor of 2.5 higher than the case for lower field enhancement factor. The total efficiency, however, is 21.9 % which is lower due to the large power consumption at high field enhancement factors. Thus, the carbon nanostructure coating achieves combustion with a higher combustion efficiency with an input voltage of just 50 V.

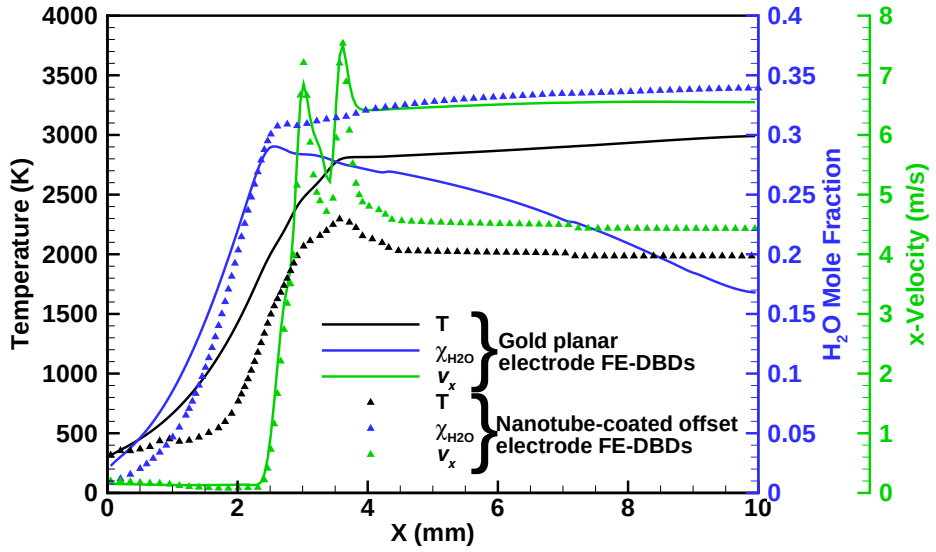

Figure 5.21. Comparison of the flow velocity induced by the gold planar and carbon nanostructure coated offset electrode FE-DBDs and its effect on the temperature and H_2O mole fraction along the centerline of the microcombustor main channel.

6. SUMMARY

A numerical model is built to study argon plasma properties for a square wave input with a cycle frequency of 80 kHz in a R2R RFCVD system for carbon nanostructures, and the results are compared to experimental measurements. The higher frequency harmonics associated with the 80 kHz cycle frequency square wave voltage enable the sustenance of the high sheath displacement current required for an α discharge. An increase in voltage leads to sheath breakdown causing transition to a hybrid mode between the α and γ modes, with a 4 orders of magnitude higher electron number density than the α mode. The sheath displacement current of the hybrid mode is high during the rapid rise and fall of voltage and low during the constant voltage duration of the RF cycle. A further increase in the voltage produces the γ mode where the sheath displacement current is low throughout the cycle. The variations of gas temperature with voltage and gas pressure follow the same trend for simulations and experiments. The modeled values are 22.5% higher on average due to the presence of residual molecular hydrogen and hydrocarbon species in the experiments. Variation of the cycle and rise frequencies for the square wave reveals that a minimum rise frequency of 400 kHz and a minimum cycle frequency of 40 kHz are required for the sustenance of the α and the hybrid modes at 9.5 mbar.

The Ar emission intensity is modeled for 186 V voltage amplitude and 80 kHz cycle frequency square wave input at 9.5 mbar using a CRM, and the results are compared to OES measurements at 3 different locations in the discharge for the 400 to 870 nm wavelength range. The first 41 states of argon are modeled and excitation, relaxation, ionization, recombination, diffusion, spontaneous emission and radiation trapping are considered to determine the population densities of each state. The RSS deviation between OES and CRM is found to be 0.07 at the discharge center, indicating very good agreement between the two. The deviation is higher close to

the electrodes due to the uncertainty in the measurement location, non-uniformity of plasma properties close to the electrodes, and contribution from ion emissions which are not considered in the CRM.

The 1D argon plasma model is extended to include hydrogen chemistry and the plasma properties are studied for a square wave input of cycle frequency 80 kHz at a pressure of 9.5 mbar in the R2R RFCVD system. The existence of the α and hybrid modes in addition to the γ mode are seen for hydrogen plasma, but the transition voltage values are higher for hydrogen than for argon plasma at the same pressure. This is attributed to the diatomic nature of hydrogen which leads to electron energy transfer to the rotational and vibrational modes. The higher energy input requirement for avalanche ionization leads to higher breakdown voltage in the sheath and thereby, higher transition voltage from the α to the hybrid and the hybrid to the γ regimes. The dominant ionic species during the α mode is H_3^+ and during the hybrid and γ modes is H^+. The gas temperature predicted by the model lies in the expected range of rotational temperature values based on experimental measurements. Moreover, the ratio of the emission intensities of the H_α to the H_β lines displays the expected trend based on OES measurements.

The plasma properties obtained from the pure H_2 model are used in a 0D steady state chemistry model for hydrogen and hydrocarbon species for H_2/CH_4 plasma at different locations in the discharge gap. The dominant neutral species in the discharge overall are found to be H_2, H, C_2H and C_2H_2. The hydrocarbon ionic species with the highest mole fractions are $C_2H_3^+$, $C_2H_4^+$ and $C_2H_6^+$. Increasing the concentration of methane from 5% to 30% does not have a significant impact on the precursor concentrations which is in agreement with experimental sensitivity analysis. In the region close to the electrode or for α discharges, the high electron temperature leads to higher dissociation and ionization rates, which increases the mole fraction of the ions. The low electron temperature and number density at the edge of the sheath lead to negligible ion concentration at this location. This might be suitable for nanostructure

deposition in cases where low precursor concentrations are desirable (such as for single layer graphene) to avoid over deposition.

A new field emission dielectric barrier discharge flow control and power generation methodology is proposed for microsystems where large viscous losses and moving parts make conventional pumping highly inefficient. We present two FE-DBD configurations with different electrode arrangements to generate surface discharges, namely the offset electrode actuators with one electrode embedded in a dielectric layer, and the planar electrode actuators where both electrodes are exposed to the atmosphere. The electrodes and dielectric of the DBD are to be only a few microns thick for the device to be field emission dominated for voltages around a few hundred volts and below. PIC/MCC is used to model the plasma properties, and the source terms are computed by tracking the momentum and energy exchange over all collisions and averaging over time. An input frequency of 1 GHz is found to produce the highest source terms when compared to other frequencies for the same input voltage. A single FE-DBD produces period averaged momentum source of $\sim$1 MN/m^3 and energy source of $\sim$1 GW/m^3 with power consumption of on the order of tens or hundreds of mW/cm.

These source terms are coupled to the energy and momentum conservation equations to model flow through microchannels. Theoretical analysis for plasma actuated Poiseulle flow is in good agreement with CFD, when the actuators are closely placed along the microchannel to create a continuous uniform body force under incompressible conditions. The gain in flow rate is inversely proportional to Re. CFD simulations of the compressible flow actuated by discrete FE-DBDs show that the offset electrode configuration is better for providing directed velocity for micropumping applications. The planar electrode actuators, on the other hand, provide more efficient mixing by generating vortices and when a DC bias voltage is not applied, they impart heat without pumping the flow. A variety of actuators, arrangements, and inputs can be combined to produce temperature, velocity, and vorticity profiles that are catered to different applications.

The electrohydrodynamic interaction parameters of commonly used aerospace plasmas are summarized and the maximum flow velocity at which the EHD forces still play a significant role in flow actuation for each plasma type are evaluated. Field emission based actuators are best suited for microcombustion applications owing to their ability to overcome the viscous forces associated with low Reynolds number flows by consuming very low power. They also provide a source of heat to overcome the large heat lost through the walls of the microcombustor. The planar electrode FE-DBDs are found to initiate and sustain the microcombustion of hydrogen-air mixtures with a power output of 1.97 W/cm at 29.7% combustion efficiency and 28.8% total efficiency. Coating the electrode surfaces of FE-DBDs enhances the field emission and reduces the breakdown voltage further achieving microcombustion with a 77.1% combustion efficiency using 4 offset electrode actuators at just 50 V input.

7. RECOMMENDATIONS

This work presents 1D analysis of argon and hydrogen plasma between the electrodes in a R2R RFCVD system. The next step would be to include the copper foil growth substrate between the electrodes to evaluate the effect of its presence on the plasma structure and properties. The field emission due to the nanostructures grown on the substrate could modify the plasma characteristics and this effect must be resolved. The chemistry for N_2, O_2 and CH_4 would need to be included in the 1D model in order to determine the precursors that contribute to the growth of different nanostructures. The results of the model at different conditions would have to be related to the growth characteristics similar to the Goodwin-Harris [30, 169] model for diamond deposition. A higher dimensional (2D or 3D) model that includes all the different gases used in the system and the coupling effect of the plasma with the growth substrate would be of interest for nanostructure growth optimization. The RF power losses and various heat transfer effects in the chamber could be simulated using this method. However, it would require parallel processing capabilities to handle the large number of cells associated with such a large-scale model. Another interesting direction for growth optimization is to perform Molecular Dynamics (MD) simulations near the growth region to model the deposition process based on the plasma chemistry and properties. Growth optimization and control would ultimately result in reducing the harmful emission of Polycyclic Aromatic Hydrocarbons (PAHs) and improve the utilization of methane in the system, thereby contributing to more environmentally friendly manufacturing.

The feasibility of FE-DBDs for flow actuation and microcombustion are evaluated in this work using 2D PIC/MCC and CFD simulations. The actuators in the microcombustor are located near the intersection of the microcombustor main channel and the air inlet channel. It would be interest to investigate the influence of the actuator

location on the combustion performance in future work. The effect of the plasma radicals on the combustion mechanism is not included here and may further enhance the combustion characteristics of this MEMS microcombustor concept. The inclusion of air chemistry for PIC/MCC, charged species chemistry for CFD, and evaluation of these effects would be the next step to advance the simulations. It would also be of great interest to fabricate the FE-DBD device designed in this work and evaluate its ability to generate microplasma. Experimental plasma properties and flow actuation characteristics would have to be compared with the predicted 2D results. The ultimate goal would be to deposit carbon nanostructures on the electrode surfaces in order to reduce operational voltage as well as use electrodes that do not experience disintegration or degradation when applied for microcombustion power generation.

REFERENCES

[1] C Lan, PB Amama, TS Fisher, and RG Reifenberger. Correlating electrical resistance to growth conditions for multiwalled carbon nanotubes. *Applied Physics Letters*, 91(9):093105, 2007.

[2] J Hone, MC Llaguno, NM Nemes, AT Johnson, JE Fischer, DA Walters, MJ Casavant, J Schmidt, and RE Smalley. Electrical and thermal transport properties of magnetically aligned single wall carbon nanotube films. *Applied Physics Letters*, 77(5):666–668, 2000.

[3] PB Amama, C Lan, BA Cola, X Xu, RG Reifenberger, and TS Fisher. Electrical and thermal interface conductance of carbon nanotubes grown under direct current bias voltage. *The Journal of Physical Chemistry C*, 112(49):19727–19733, 2008.

[4] AHC Neto, F Guinea, NMR Peres, KS Novoselov, and AK Geim. The electronic properties of graphene. *Reviews of modern physics*, 81(1):109, 2009.

[5] MM Shokrieh and R Rafiee. A review of the mechanical properties of isolated carbon nanotubes and carbon nanotube composites. *Mechanics of composite materials*, 46(2):155–172, 2010.

[6] MM Shokrieh and R Rafiee. Prediction of young's modulus of graphene sheets and carbon nanotubes using nanoscale continuum mechanics approach. *Materials & Design*, 31(2):790–795, 2010.

[7] J Che, T Cagin, and WA Goddard III. Thermal conductivity of carbon nanotubes. *Nanotechnology*, 11(2):65, 2000.

[8] MS Dresselhaus and PC Eklund. Phonons in carbon nanotubes. *Advances in Physics*, 49(6):705–814, 2000.

[9] G Xiong. Synthesis of graphene nanomaterials and their application in electrochemical energy storage. 2013.

[10] G Xiong, C Meng, RG Reifenberger, PP Irazoqui, and TS Fisher. Graphitic petal electrodes for all-solid-state flexible supercapacitors. *Advanced Energy Materials*, 4(3), 2014.

[11] JC Claussen, A Kumar, DB Jaroch, MH Khawaja, AB Hibbard, DM Porterfield, and TS Fisher. Nanostructuring platinum nanoparticles on multilayered graphene petal nanosheets for electrochemical biosensing. *Advanced Functional Materials*, 22(16):3399–3405, 2012.

[12] B Zhang, VR Patlolla, D Chiao, DK Kalla, H Misak, and R Asmatulu. Galvanic corrosion of al/cu meshes with carbon fibers and graphene and ito-based nanocomposite coatings as alternative approaches for lightning strikes. *The International Journal of Advanced Manufacturing Technology*, pages 1–7, 2013.

[13] S Chen, L Brown, M Levendorf, W Cai, S Ju, J Edgeworth, X Li, CW Magnuson, A Velamakanni, RD Piner, et al. Oxidation resistance of graphene-coated Cu and Cu/Ni alloy. *ACS nano*, 5(2):1321–1327, 2011.

[14] AS Kousalya, A Kumar, R Paul, D Zemlyanov, and TS Fisher. Graphene: An effective oxidation barrier coating for liquid and two-phase cooling systems. *Corrosion Science*, 69:5–10, 2013.

[15] MFL De Volder, SH Tawfick, RH Baughman, and AJ Hart. Carbon nanotubes: present and future commercial applications. *science*, 339(6119):535–539, 2013.

[16] DDL Chung. Carbon materials for structural self-sensing, electromagnetic shielding and thermal interfacing. *Carbon*, 50(9):3342–3353, 2012.

[17] O Gohardani, MC Elola, and C Elizetxea. Potential and prospective implementation of carbon nanotubes on next generation aircraft and space vehicles: a review of current and expected applications in aerospace sciences. *Progress in Aerospace Sciences*, 70:42–68, 2014.

[18] VAM Selvan, RB Anand, and M Udayakumar. Effect of cerium oxide nanoparticles and carbon nanotubes as fuel-borne additives in diesterol blends on the performance, combustion and emission characteristics of a variable compression ratio engine. *Fuel*, 130:160–167, 2014.

[19] J Park, S Rosenblatt, Y Yaish, V Sazonova, H Üstünel, S Braig, TA Arias, PW Brouwer, and PL McEuen. Electron-phonon scattering in metallic single-walled carbon nanotubes. *Nano Letters*, 4(3):517–520, 2004.

[20] S Bianco, M Giorcelli, S Musso, M Castellino, F Agresti, A Khandelwal, S Lo Russo, M Kumar, Y Ando, and A Tagliaferro. Hydrogen adsorption in several types of carbon nanotubes. *Journal of nanoscience and nanotechnology*, 9(12):6806–6812, 2009.

[21] C Liu, YY Fan, M Liu, HT Cong, HM Cheng, and MS Dresselhaus. Hydrogen storage in single-walled carbon nanotubes at room temperature. *Science*, 286(5442):1127–1129, 1999.

[22] X Shi, JL Hudson, PP Spicer, JM Tour, R Krishnamoorti, and G Mikos. Injectable nanocomposites of single-walled carbon nanotubes and biodegradable polymers for bone tissue engineering. *Biomacromolecules*, 7(7):2237–2242, 2006.

[23] M Meyyappan. A review of plasma enhanced chemical vapour deposition of carbon nanotubes. *Journal of Physics D: Applied Physics*, 42(21):213001, 2009.

[24] T Guo, P Nikolaev, A Thess, DT Colbert, and RE Smalley. Catalytic growth of single-walled manotubes by laser vaporization. *Chemical physics letters*, 243(1):49–54, 1995.

[25] KS Novoselov, AK Geim, SV Morozov, D Jiang, Y Zhang, SV Dubonos, IV Grigorieva, and AA Firsov. Electric field effect in atomically thin carbon films. *science*, 306(5696):666–669, 2004.

[26] S Iijima. Helical microtubules of graphitic carbon. *nature*, 354(6348):56–58, 1991.

[27] C Journet, WK Maser, P Bernier, A Loiseau, ML de La Chapelle, S Lefrant, P Deniard, R Lee, and JE Fischer. Large-scale production of single-walled carbon nanotubes by the electric-arc technique. *nature*, 388(6644):756–758, 1997.

[28] M Füner, C Wild, and P Koidl. Numerical simulations of microwave plasma reactors for diamond CVD. *Surface and coatings technology*, 74:221–226, 1995.

[29] H Yamada, A Chayahara, and Y Mokuno. Simplified description of microwave plasma discharge for chemical vapor deposition of diamond. *Journal of applied physics*, 101(6):063302, 2007.

[30] K Hassouni, F Silva, and A Gicquel. Modelling of diamond deposition microwave cavity generated plasmas. *Journal of Physics D: Applied Physics*, 43(15):153001, 2010.

[31] S Bhaviripudi, X Jia, MS Dresselhaus, and J Kong. Role of kinetic factors in chemical vapor deposition synthesis of uniform large area graphene using copper catalyst. *Nano Letters*, 10(10):4128–4133, 2010.

[32] X Li, CW Magnuson, A Venugopal, RM Tromp, JB Hannon, EM Vogel, L Colombo, and RS Ruoff. Large-area graphene single crystals grown by low-pressure chemical vapor deposition of methane on copper. *Journal of the American Chemical Society*, 133(9):2816–2819, 2011.

[33] I Vlassiouk, M Regmi, P Fulvio, S Dai, P Datskos, G Eres, and S Smirnov. Role of hydrogen in chemical vapor deposition growth of large single-crystal graphene. *ACS Nano*, 5(7):6069–6076, 2011.

[34] Z Luo, Y Lu, DW Singer, ME Berck, LA Somers, BR Goldsmith, and ATC Johnson. Effect of substrate roughness and feedstock concentration on growth of wafer-scale graphene at atmospheric pressure. *Chemistry of Materials*, 23(6):1441–1447, 2011.

[35] C Miao, C Zheng, O Liang, and Y-H Xie. Chemical vapor deposition of graphene. In *Physics and Applications of Graphene-Experiments*. IntechOpen, 2011.

[36] C-M Seah, S-P Chai, and AR Mohamed. Mechanisms of graphene growth by chemical vapour deposition on transition metals. *Carbon*, 70:1–21, 2014.

[37] Y P Raizer. *Gas discharge physics*. Springer, 1991.

[38] S M Levitskii. An investigation of the sparking potential of a rf discharge in a gas in the transition range of frequencies and pressures. *Sov. Phys.–Tech. Phys*, 2:887–893, 1957.

[39] Y P Raizer, M N Shneider, and N A Yatsenko. *Radio-frequency capacitive discharges*. CRC Press, 1995.

[40] V A Godyak and A S Khanneh. Ion bombardment secondaty electron maintenance of steady rf discharge. *IEEE Transactions on Plasma Science*, 14(2):112–123, 1986.

[41] V A Godyak, R B Piejak, and B M Alexandrovich. Evolution of the electron-energy-distribution function during rf discharge transition to the high-voltage mode. *Physical Review Letters*, 68(1):40, 1992.

[42] V Godyak. Hot plasma effects in gas discharge plasma. *Physics of Plasmas*, 12(5):055501, 2005.

[43] S Y Moon, D B Kim, B Gweon, and W Choe. Driving frequency effects on the characteristics of atmospheric pressure capacitive helium discharge. *Applied Physics Letters*, 93(22):221506, 2008.

[44] J L Walsh, F Iza, and M G Kong. Atmospheric glow discharges from the high-frequency to very high-frequency bands. *Applied Physics Letters*, 93(25):251502, 2008.

[45] Y T Zhang, Q Q Li, J Lou, and Q M Li. The characteristics of atmospheric radio frequency discharges with frequency increasing at a constant power density. *Applied Physics Letters*, 97(14):141504, 2010.

[46] Y T Zhang and S Y Cui. Frequency effects on the electron density and α-γ mode transition in atmospheric radio frequency discharges. *Physics of Plasmas*, 18(8):083509, 2011.

[47] I V Schweigert and A L Alexandrov. Transition between different modes of a capacitively coupled radio frequency discharge in CH_4 in one-and two-dimensional pic-mcc simulations. *IEEE transactions on plasma science*, 33(2):615–623, 2005.

[48] J J Shi, X T Deng, R Hall, J D Punnett, and M G Kong. Three modes in a radio frequency atmospheric pressure glow discharge. *Journal of Applied Physics*, 94(10):6303–6310, 2003.

[49] F Paschen. Ueber die zum funkenübergang in luft, wasserstoff und kohlensäure bei verschiedenen drucken erforderliche potentialdifferenz. *Annalen der Physik*, 273(5):69–96, 1889.

[50] I Odrobina and M Kando. Discontinuous transitions between alpha and gamma regimes of rf capacitive discharge. *Plasma Sources Science and Technology*, 5(3):517, 1996.

[51] V Lisovskiy, J-P Booth, K Landry, D Douai, V Cassagne, and V Yegorenkov. Modes and the alpha-gamma transition in rf capacitive discharges in N_2O at different rf frequencies. *Physics of Plasmas*, 13(10):103505, 2006.

[52] L Xiang-Mei, S Yuan-Hong, and W You-Nian. Driving frequency effects on the mode transition in capacitively coupled argon discharges. *Chinese Physics B*, 20(6):065205, 2011.

[53] S Conti, PI Porshnev, A Fridman, L A Kennedy, J M Grace, K D Sieber, D R Freeman, and K S Robinson. Experimental and numerical investigation of a capacitively coupled low-radio frequency nitrogen plasma. *Experimental Thermal and Fluid Science*, 24(3-4):79–91, 2001.

[54] JS Townsend. Electricity in gases, 1915.

[55] DB Go and A Venkattraman. Microscale gas breakdown: ion-enhanced field emission and the modified Paschen's curve. *Journal of Physics D: Applied Physics*, 47(50):503001, 2014.

[56] RH Fowler and L Nordheim. Electron emission in intense electric fields. *Proceedings of the Royal Society of London A*, 119(781):173–181, 1928.

[57] RS Dhariwal, J-M Torres, and MPY Desmulliez. Electric field breakdown at micrometre separations in air and nitrogen at atmospheric pressure. *IEE Proceedings - Science, Measurement and Technology*, 147(5):261–265, 2000.

[58] A Venkattraman and AA Alexeenko. Scaling law for direct current field emission-driven microscale gas breakdown. *Physics of Plasmas*, 19(12):123515, 2012.

[59] M Radmilović-Radjenović and B Radjenović. The influence of ion-enhanced field emission on the high-frequency breakdown in microgaps. *Plasma Sources Science and Technology*, 16(2):337, 2007.

[60] WS Boyle and P Kisliuk. Departure from Paschen's law of breakdown in gases. *Physical Review*, 97(2):255, 1955.

[61] E Hourdakis, BJ Simonds, and NM Zimmerman. Submicron gap capacitor for measurement of breakdown voltage in air. *Review of scientific instruments*, 77(3):034702, 2006.

[62] J Roth, D Sherman, and S Wilkinson. Boundary layer flow control with a one atmosphere uniform glow discharge surface plasma. In *36th AIAA Aerospace Sciences Meeting and Exhibit*, page 328, 1998.

[63] T Corke, E Jumper, M Post, D Orlov, and T McLaughlin. Application of weakly-ionized plasmas as wing flow-control devices. In *40th AIAA Aerospace Sciences Meeting & Exhibit*, page 350, 2002.

[64] J Roth, H Sin, RCM Madhan, and S Wilkinson. Flow re-attachment and acceleration by paraelectric and peristaltic electrohydrodynamic (EHD) effects. In *41st Aerospace Sciences Meeting and Exhibit*, page 531, 2003.

[65] ML Post and TC Corke. Separation control on high angle of attack airfoil using plasma actuators. *AIAA Journal*, 42(11):2177–2184, 2004.

[66] E Moreau. Airflow control by non-thermal plasma actuators. *Journal of Physics D: Applied Physics*, 40(3):605, 2007.

[67] TC Corke, ML Post, and DM Orlov. Single dielectric barrier discharge plasma enhanced aerodynamics: physics, modeling and applications. *Experiments in Fluids*, 46(1):1–26, 2009.

[68] S Im, H Do, and MA Cappelli. Dielectric barrier discharge control of a turbulent boundary layer in a supersonic flow. *Applied Physics Letters*, 97(4):041503, 2010.

[69] S Im, H Do, and MA Cappelli. The manipulation of an unstarting supersonic flow by plasma actuator. *Journal of Physics D: Applied Physics*, 45(48):485202, 2012.

[70] E Moreau, A Debien, N Benard, T Jukes, R Whalley, KS Choi, A Berendt, J Podlinski, and J Mizeraczyk. Surface dielectric barrier discharge plasma actuators. *ERCOFTAC Bulletin*, 94:5–10, 2013.

[71] S El-Khabiry and GM Colver. Drag reduction by dc corona discharge along an electrically conductive flat plate for small reynolds number flow. *Physics of Fluids*, 9(3):587–599, 1997.

[72] SO Macheret, MN Shneider, and RB Miles. Magnetohydrodynamic and electrohydrodynamic control of hypersonic flows of weakly ionized plasmas. *AIAA Journal*, 42(7):1378–1387, 2004.

[73] C-C Wang and S Roy. Microscale plasma actuators for improved thrust density. *Journal of applied physics*, 106(1):013310, 2009.

[74] SS Tholeti, G Shivkumar, and AA Alexeenko. Field emission microplasma actuation for microchannel flows. *Journal of Physics D: Applied Physics*, 49(21):215203, 2016.

[75] G Shivkumar, SS Tholeti, and AA Alexeenko. Microchannel flow enhancement by microplasma actuation. In *ASME 2015 13th International Conference on Nanochannels, Microchannels, and Minichannels collocated with the ASME 2015 International Technical Conference and Exhibition on Packaging and Integration of Electronic and Photonic Microsystems*, pages V001T04A006–V001T04A006. American Society of Mechanical Engineers, 2015.

[76] G Shivkumar, L Qiao, and AA Alexeenko. Plasma-flow interactions in field-emission discharges with applications in microcombustion. *Journal of Physics D: Applied Physics*, 52(38):384001, 2019.

[77] T Bhuvana, A Kumar, A Sood, RH Gerzeski, J Hu, VS Bhadram, C Narayana, and TS Fisher. Contiguous petal-like carbon nanosheet outgrowths from graphite fibers by plasma CVD. *ACS Applied Materials & Interfaces*, 2(3):644–648, 2010.

[78] SK Srivastava, AK Shukla, VD Vankar, and V Kumar. Growth, structure and field emission characteristics of petal like carbon nano-structured thin films. *Thin Solid Films*, 492(1-2):124–130, 2005.

[79] S Dumpala, A Safir, D Mudd, RW Cohn, MK Sunkara, and GU Sumanasekera. Controlled synthesis and enhanced field emission characteristics of conical carbon nanotubular arrays. *Diamond and Related Materials*, 18(10):1262–1266, 2009.

[80] SS Tholeti. *Particle modeling of non-equilibrium field emission driven RF microplasmas*. PhD thesis, Purdue University, 2016.

[81] B Jayaraman and W Shyy. Modeling of dielectric barrier discharge-induced fluid dynamics and heat transfer. *Progress in Aerospace Sciences*, 44(3):139–191, 2008.

[82] NY Babaeva, DV Tereshonok, and GV Naidis. Fluid and hybrid modeling of nanosecond surface discharges: effect of polarity and secondary electrons emission. *Plasma Sources Science and Technology*, 25(4):044008, 2016.

[83] X Che, T Shao, W Nie, and P Yan. Numerical simulation on a nanosecond-pulse surface dielectric barrier discharge actuator in near space. *Journal of Physics D: Applied Physics*, 45(14):145201, 2012.

[84] W Hilbun and B Case. Preliminary development of a computational model of a dielectric barrier discharge. In *43rd AIAA Aerospace Sciences Meeting and Exhibit*, page 1176, 2005.

[85] KK Mackay, JB Freund, and HT Johnson. Enhancement of hydrogen microcombustion via field-emission dielectric barrier discharge. *Plasma Sources Science and Technology*, 27(8):085007, 2018.

[86] Y Zhu, S Shcherbanev, B Baron, and S Starikovskaia. Nanosecond surface dielectric barrier discharge in atmospheric pressure air: I. measurements and 2D modeling of morphology, propagation and hydrodynamic perturbations. *Plasma Sources Science and Technology*, 26(12):125004, 2017.

[87] H Shan and Y-T Lee. Numerical modeling of dielectric barrier discharge plasma actuation. *Journal of Fluids Engineering*, 138(5):051104, 2016.

[88] N Benard, S Laizet, and E Moreau. PIV-based dynamic model of EHD volume force produced by a surface dielectric barrier discharge. In *55th AIAA Aerospace Sciences Meeting*, page 1579, 2017.

[89] CM Spadaccini, X Zhang, CP Cadou, N Miki, and IA Waitz. Preliminary development of a hydrocarbon-fueled catalytic micro-combustor. *Sensors and Actuators A: Physical*, 103(1-2):219–224, 2003.

[90] HL Cao and JL Xu. Thermal performance of a micro-combustor for micro-gas turbine system. *Energy Conversion and Management*, 48(5):1569–1578, 2007.

[91] Y Ju and K Maruta. Microscale combustion: technology development and fundamental research. *Progress in Energy and Combustion Science*, 37(6):669–715, 2011.

[92] M A Alrefae, A Kumar, P Pandita, A Candadai, I Bilionis, and T S Fisher. Process optimization of graphene growth in a roll-to-roll plasma CVD system. *AIP Advances*, 7(11):115102, 2017.

[93] K R Saviers, M A Alrefae, and T S Fisher. Roll-to-roll production of graphitic petals on carbon fiber tow. *Advanced Engineering Materials*, 20(8):1800004, 2018.

[94] V Byturin, A Nedospasov, B Tolkunov, A Kuznetsov, N Vyatavkin, A Klimov, and D vanWie. Plasma-assisted combustion. In *40th AIAA Aerospace Sciences Meeting & Exhibit*, page 493, 2001.

[95] SM Starikovskaia. Plasma assisted ignition and combustion. *Journal of Physics D: Applied Physics*, 39(16):R265, 2006.

[96] JK Lefkowitz, Y Ju, CA Stevens, T Ombrello, F Schauer, and J Hoke. The effects of repetitively pulsed nanosecond discharges on ignition time in a pulsed detonation engine. In *49th AIAA/ASME/SAE/ASEE Joint PropulsionConference*, page 3719. 2013.

[97] SM Starikovskaia. Plasma-assisted ignition and combustion: nanosecond discharges and development of kinetic mechanisms. *Journal of Physics D: Applied Physics*, 47(35):353001, 2014.

[98] Y Ju and W Sun. Plasma assisted combustion: dynamics and chemistry. *Progress in Energy and Combustion Science*, 48:21–83, 2015.

[99] JC Schulz, KC Gottiparthi, and S Menon. Ionization in gaseous detonation waves. *Shock Waves*, 22(6):579–590, 2012.

[100] G Shivkumar, MA Alrefae, SS Tholeti, SO Macheret, TS Fisher, and AA Alexeenko. Discharge regimes and emission characteristics of capacitively coupled radio frequency argon plasma with a square wave input. *Journal of Applied Physics*, 125(22):223301, 2019.

[101] G J Nienhuis, W J Goedheer, E A G Hamers, W G J H M Van Sark, and J Bezemer. A self-consistent fluid model for radio-frequency discharges in SiH_4-H_2 compared to experiments. *Journal of Applied Physics*, 82(5):2060–2071, 1997.

[102] D Herrebout, A Bogaerts, M Yan, R Gijbels, W Goedheer, and E Dekempeneer. One-dimensional fluid model for an rf methane plasma of interest in deposition of diamond-like carbon layers. *Journal of Applied Physics*, 90(2):570–579, 2001.

[103] Phelps database. *www.lxcat.net*, retrieved on July 12, 2016.

[104] TRINITI database. *www.lxcat.net*, retrieved on July 12, 2016.

[105] S S Tholeti, M N Shneider, and A A Alexeenko. Kinetic modeling of evolution of 3+ 1: resonance enhanced multiphoton ionization plasma in argon at low pressures. *Physics of Plasmas*, 21(6):063507, 2014.

[106] N A Dyatko, Y Z Ionikh, I V Kochetov, D L Marinov, A V Meshchanov, A P Napartovich, F B Petrov, and S A Starostin. Experimental and theoretical study of the transition between diffuse and contracted forms of the glow discharge in argon. *Journal of Physics D: Applied Physics*, 41(5):055204, 2008.

[107] D J Eckstrom, H H Nakano, D C Lorents, T Rothem, J A Betts, M E Lainhart, D A Dakin, and J E Maenchen. Characteristics of electron-beam-excited Xe^*_2 at low pressures as a vacuum ultraviolet source. *Journal of Applied Physics*, 64(4):1679–1690, 1988.

[108] V Marchenko. Dissociation of homonuclear ions by electron impact. *Zh. Eksp. Teor. Fiz*, 85:510, 1983.

[109] G Shivkumar, S S Tholeti, M A Alrefae, T S Fisher, and A A Alexeenko. Analysis of hydrogen plasma in a microwave plasma chemical vapor deposition reactor. *Journal of Applied Physics*, 119(11):113301, 2016.

[110] M A Alrefae and T S Fisher. Thermal analysis and optimization of graphene deposition in a roll-to-roll plasma CVD process. In *The International Heat Transfer Conference (IHTC)*, pages 5661–5668, August 10-15, 2018.

[111] R K Gangwar, L Sharma, R Srivastava, and A D Stauffer. Argon plasma modeling with detailed fine-structure cross sections. *Journal of Applied Physics*, 111(5):053307, 2012.

[112] K E Evdokimov, M E Konischev, V F Pichugin, and Z Sun. Study of argon ions density and electron temperature and density in magnetron plasma by optical emission spectroscopy and collisional-radiative model. *Resource-Efficient Technologies*, 3(2):187–193, 2017.

[113] M A Ali and P M Stone. Electron impact ionization of metastable rare gases: He, Ne and Ar. *International Journal of Mass Spectrometry*, 271(1-3):51–57, 2008.

[114] H Deutsch, K Becker, A N Grum-Grzhimailo, K Bartschat, H Summers, M Probst, S Matt-Leubner, and T D Märk. Calculated cross sections for the electron-impact ionization of excited argon atoms using the DM formalism. *International Journal of Mass Spectrometry*, 233(1-3):39–43, 2004.

[115] NIST atomic spectra database. *https://www.nist.gov/pml/atomic-spectra-database*, retrieved on March 13, 2018.

[116] BSR database. *www.lxcat.net*, retrieved on March 13, 2018.

[117] O Zatsarinny, Y Wang, and K Bartschat. Electron-impact excitation of argon at intermediate energies. *Physical Review A*, 89(2):022706, 2014.

[118] R K Gangwar, L Sharma, R Srivastava, and A D Stauffer. Electron-impact excitation of argon: Cross sections of interest in plasma modeling. *Physical Review A*, 81(5):052707, 2010.

[119] NGFSRDW database. *www.lxcat.net*, retrieved on March 13, 2018.

[120] J J Shi and M G Kong. Mechanisms of the α and γ modes in radio-frequency atmospheric glow discharges. *Journal of Applied Physics*, 97(2):023306, 2005.

[121] B Bruneau, T Novikova, T Lafleur, J P Booth, and E V Johnson. Ion flux asymmetry in radiofrequency capacitively-coupled plasmas excited by sawtooth-like waveforms. *Plasma Sources Science and Technology*, 23(6):065010, 2014.

[122] T J Sanders, E L Caraway, C Hall, J H Linn, C Adkins, H Deju, and T Buschor. Silicon nitride deposition process for low cost microelectronics applications. In *Proceedings of the UGIM Symposium, Microelectronics Education for the Future. Twelfth Biennial University/Government/Industry Microelectronics Symposium (Cat. No. 97CH36030)*, pages 173–176. IEEE, 1997.

[123] P Chabert and N Braithwaite. *Physics of radio-frequency plasmas*. Cambridge University Press, 2011.

[124] K Hassouni, TA Grotjohn, and A Gicquel. Self-consistent microwave field and plasma discharge simulations for a moderate pressure hydrogen discharge reactor. *Journal of Applied Physics*, 86(1):134–151, 1999.

[125] S Prasanna, C Rond, A Michau, K Hassouni, and A Gicquel. Effect of buoyancy on power deposition in microwave cavity hydrogen plasma source. *Plasma Sources Science and Technology*, 25(4):045017, 2016.

[126] Phelps database. *www.lxcat.net*, retrieved on Oct 29, 2015.

[127] RK Janev, WD Langer, DE Post Jr., and K Evans Jr. Elementary processes in hydrogen-helium plasmas: Cross sections and reaction rate coefficients. In *Springer-Verlag (Springer Series on Atoms and Plasmas)*, volume 4, 1987.

[128] TRINITI database. *www.lxcat.net*, retrieved on Sep 11, 2018.

[129] CD Scott, S Farhat, A Gicquel, and K Hassouni. Determining electron temperature and density in a hydrogen microwave plasma. *Journal of Thermophysics and Heat Transfer*, 10(3):426–435, 1996.

[130] J-H Lee. Basic governing equations for the flight regimes of aeroassisted orbital transfer vehicles. *Thermal Design of Aeroassisted Orbital Transfer Vehicles*, 96:3–53, 1985.

[131] S Chapman, TG Cowling, and D Burnett. *The mathematical theory of non-uniform gases: an account of the kinetic theory of viscosity, thermal conduction and diffusion in gases*. Cambridge University Press, 1990.

[132] NIST chemistry webbook. *https://webbook.nist.gov/chemistry*, retrieved on March 13, 2018.

[133] C Gorse, M Capitelli, M Bacal, J Bretagne, and A Lagana. Progress in the non-equilibrium vibrational kinetics of hydrogen in magnetic multicusp H-ion sources. *Chemical physics*, 117(2):177–195, 1987.

[134] JH Kiefer and RW Lutz. Vibrational relaxation of hydrogen. *The Journal of Chemical Physics*, 44(2):668–672, 1966.

[135] S Iordanova and T Paunska. A collisional radiative model of hydrogen plasmas developed for diagnostic purposes of negative ion sources. *Review of Scientific Instruments*, 87(2):02B110, 2016.

[136] MA Alrefae. *Process characterization and optimization of roll-to-roll plasma chemical vapor deposition for graphene growth*. PhD thesis, Purdue University, 2018.

[137] H Kim, C Mattevi, MR Calvo, JC Oberg, L Artiglia, S Agnoli, CF Hirjibehedin, M Chhowalla, and E Saiz. Activation energy paths for graphene nucleation and growth on cu. *ACS Nano*, 6(4):3614–3623, 2012.

[138] H Kim, E Saiz, M Chhowalla, and C Mattevi. Modeling of the self-limited growth in catalytic chemical vapor deposition of graphene. *New Journal of Physics*, 15(5):053012, 2013.

[139] K Pashova, I Hinkov, X Aubert, S Prasanna, F Bénédic, and S Farhat. Graphene synthesis by microwave plasma chemical vapor deposition: Analysis of the emission spectra and modeling. *Plasma Sources Science and Technology*, 2019.

[140] K Tachibana, M Nishida, H Harima, and Y Urano. Diagnostics and modelling of a methane plasma used in the chemical vapour deposition of amorphous carbon films. *Journal of Physics D: Applied Physics*, 17(8):1727, 1984.

[141] H Tahara, K Minami, A Murai, T Yasui, and T Yoshikawa. Diagnostic experiment and kinetic model analysis of microwave CH_4/H_2 plasmas for deposition of diamondlike carbon films. *Japanese Journal of Applied Physics*, 34(4R):1972, 1995.

[142] G Lombardi, K Hassouni, G-D Stancu, L Mechold, J Röpcke, and A Gicquel. Modeling of microwave discharges of H_2 admixed with CH_4 for diamond deposition. *Journal of Applied Physics*, 98(5):053303, 2005.

[143] GP Smith, DM Golden, M Frenklach, NW Moriarty, B Eiteneer, M Goldenberg, CT Bowman, RK Hanson, S Song, WC Gardiner Jr., VL Lissianski, and Z Qin. GRI-Mech 3.0, 1999.

[144] BJ McBride, S Gordon, and MA Reno. Coefficients for calculating thermodynamic and transport properties of individual species. *NASA Technical Memorandum 4513*, 1993.

[145] A Burcat. Burcat database.

[146] L Lehfaoui, C Rebrion-Rowe, S Laubé, JBA Mitchell, and BR Rowe. The dissociative recombination of hydrocarbon ions. i. light alkanes. *The Journal of Chemical Physics*, 106(13):5406–5412, 1997.

[147] RK Janev and D Reiter. Collision processes of CH_y and CH_y^+ hydrocarbons with plasma electrons and protons. *Physics of Plasmas*, 9(9):4071–4081, 2002.

[148] RK Janev and D Reiter. Collision processes of $C_{2,3}H_y$ and $C_{2,3}H_y^+$ hydrocarbons with electrons and protons. *Physics of Plasmas*, 11(2):780–829, 2004.

[149] Hayashi database. *www.lxcat.net*, retrieved on Mar 20, 2019.

[150] H Tawara, Y Itikawa, H Nishimura, H Tanaka, and Y Nakamura. Cross-section data for collisions of electrons with hydrocarbon molecules. *Atomic and Plasma-Material Interaction Data for Fusion*, page 41, 1992.

[151] AA Alexeenko, AD Strongrich, AG Cofer, A Pikus, IB Sebastiao, SS Tholeti, and G Shivkumar. Microdevices enabled by rarefied flow phenomena. In *AIP Conference Proceedings*, volume 1786, page 080001. AIP Publishing, 2016.

[152] Y Itikawa. Cross sections for electron collisions with nitrogen molecules. *Journal of Physical and Chemical Reference Data*, 35(1):31–53, 2006.

[153] BJ Nichols and FC Witteborn. Measurements of resonant charge exchange cross sections in nitrogen and argon between 0.5 and 17 eV. *NASA Technical Note D-3265*, 1966.

[154] JP Boeuf and LC Pitchford. Electrohydrodynamic force and aerodynamic flow acceleration in surface dielectric barrier discharge. *Journal of Applied Physics*, 97(10):103307, 2005.

[155] MJ Pinheiro and AA Martins. Electrical and kinetic model of an atmospheric rf device for plasma aerodynamics applications. *Journal of Applied Physics*, 108(3):033301, 2010.

[156] DB Go. *Ion generation and ionic wind heat transfer at millimeter andmicrometer scales*. PhD thesis, Purdue University, 2008.

[157] N Benard, N Balcon, and E Moreau. Electric wind produced by a surface dielectric barrier discharge operating over a wide range of relative humidity. In *47th AIAA Aerospace Sciences Meeting including The New Horizons Forum and Aerospace Exposition*, page 488, 2009.

[158] Suhas Patankar. *Numerical heat transfer and fluid flow*. CRC press, 1980.

[159] JC Zito, RJ Durscher, J Soni, S Roy, and DP Arnold. Flow and force inducement using micron size dielectric barrier discharge actuators. *Applied Physics Letters*, 100(19):193502, 2012.

[160] J Poggie. Numerical simulation of direct current glow discharges for high-speed flow control. *Journal of Propulsion and Power*, 24(5):916–922, 2008.

[161] SB Leonov and DA Yarantsev. Plasma-induced ignition and plasma-assisted combustion in high-speed flow. *Plasma Sources Science and Technology*, 16(1):132, 2006.

[162] AY Starikovskii, NB Anikin, IN Kosarev, EI Mintoussov, MM Nudnova, AE Rakitin, DV Roupassov, SM Starikovskaia, and VP Zhukov. Nanosecond-pulsed discharges for plasma-assisted combustion and aerodynamics. *Journal of Propulsion and Power*, 24(6):1182–1197, 2008.

[163] DB Go, SV Garimella, TS Fisher, and RK Mongia. Ionic winds for locally enhanced cooling. *Journal of Applied Physics*, 102(5):053302, 2007.

[164] DZ Pai, DA Lacoste, and CO Laux. Nanosecond repetitively pulsed discharges in air at atmospheric pressure-the spark regime. *Plasma Sources Science and Technology*, 19(6):065015, 2010.

[165] JO Hirschfelder, CF Curtiss, RB Bird, and MG Mayer. *Molecular theory of gases and liquids*, volume 26. Wiley New York, 1954.

[166] AC Fernandez-Pello. Micropower generation using combustion: issues and approaches. *Proceedings of the Combustion Institute*, 29(1):883–899, 2002.

[167] BJ McBride and S Gordon. Computer program for calculation of complex chemical equilibrium compositions and applications. *NASA Reference Publication 1311*, 1996.

[168] J Li, H Huang, Y Bai, S Li, and N Kobayashi. Combustion and heat release characteristics of hydrogen/air diffusion flame on a micro-jet array burner. *International Journal of Hydrogen Energy*, 43(29):13563–13574, 2018.

[169] DG Goodwin. Scaling laws for diamond chemical-vapor deposition. I. Diamond surface chemistry. *Journal of Applied Physics*, 74(11):6888–6894, 1993.

VITA

Gayathri Shivkumar

RESEARCH INTERESTS

Microplasmas, non-equilibrium plasma physics, plasma chemistry; Computational fluid dynamics; Conjugate heat transfer, radiation modeling; Chemical vapor deposition; Combustion; Vacuum freeze drying for bio/pharmaceutical manufacturing; Electric and micropropulsion.

EDUCATION

- PhD in Aeronautics and Astronautics, Purdue University, West Lafayette, IN, USA, 2019. Thesis: "Coupled Plasma, Fluid and Thermal Modeling of Low-Pressure and Microscale Gas Discharges". Advisor: Alina A. Alexeenko. GPA: 4.0/4.0.
- MS in Aeronautics and Astronautics, Purdue University, West Lafayette, IN, USA, 2015. Thesis: "Analysis of Hydrogen Plasma in MPCVD Reactor". Advisor: Alina A. Alexeenko. GPA: 3.89/4.0.
- BE in Mechanical Engineering, PES Institute of Technology, Bangalore, India, 2013. Thesis: "Design and Fabrication of a Fixed Wing Micro Air Vehicle". Advisor: TS. Prahlad. GPA: 9.15/10.0.

HONORS AND AWARDS

- 1^{st} Place Poster Award, LyoHUB/ASTM E55 Workshop on Lyophilization and Pharmaceutical Manufacturing Research, 2018.
- Thomas Jennings Student Paper Award, International Society of Lyophilization - Freeze Drying, 2018.

- Bilsland Dissertation Fellowship, Purdue University, 2018.
- John L. and Patricia R. Rich Scholarship, Purdue University, 2017.
- Best Student Paper Award, International Conference on Plasma Science, IEEE Nuclear and Plasma Sciences Society, 2017.
- One of 16 PhD students/Post-docs chosen nationwide to present at the CU Boulder-MIT-Stanford Women in Aerospace Symposium, 2017.
- Graduate Teaching Award, Purdue University Teaching Academy, 2016.
- Featured on the cover of the Journal of Applied Physics, Vol. 119, No. 11, 2016.

- MRD Merit Scholarship, Department of Mechanical Engineering, PESIT, 2012.

PROFESSIONAL EXPERIENCE

Graduate Research Assistant Jan 2015 - Apr 2018

School of Aeronautics and Astronautics, Purdue University

- Characterize and improve Radio Frequency and Microwave Plasma Chemical Vapor Deposition of carbon nanostructures using plasma, thermal and radiation modeling.
- Design Field Emission driven Dielectric Barrier Discharges and evaluate their feasibility for microcombustion application.
- Optimize pharmaceutical freeze-drying cycle design using CFD analysis and vial heat transfer modeling.

Operations Science & Technology Intern May 2018 - Aug 2018

AbbVie Inc., North Chicago, IL

- Characterize lyophilization edge-effect using CFD analysis and conjugate and radiative heat transfer modeling, explore new shelf design ideas and radiation cage to reduce edge-effect.
- CFD and heat transfer modeling to support drug product scale-up during validation.

Graduate Teaching Assistant Jan 2014 - Dec 2015

School of Aeronautics and Astronautics, Purdue University

- Introduction to Fluid Mechanics, AAE 333, Supervisors: Alina A. Alexeenko, Sergey O. Macheret.

JOURNAL PUBLICATIONS

To be Submitted

8. **G. Shivkumar**, K. Sinha, A.A. Alexeenko, S. Shang,"Analysis of Lyophilizer Shelf Fluid Flow and Heat Transfer to Quantify Edge Effect", *J. Pharm. Sci.*
7. M.A. Alrefae, **G. Shivkumar**, A.A. Alexeenko, S.O. Macheret, and T.S. Fisher, "Electrical and Spectroscopic Characteristics of Capacitively Coupled Radio Frequency Argon Plasma with a Square Wave Input", *Plas. Sources Sci. Tech.*.

Under Review

6. **G. Shivkumar**, P.S. Kazarin, A.D. Strongrich, A.A. Alexeenko, "LyoPRONTO: An Open Source Lyophilization PRocess OptimizatioN TOol", *AAPS PharmSciTech*.

Published/Accepted

5. **G. Shivkumar**, L. Qiao, A.A. Alexeenko, "Plasma-Flow Interactions in Field Emission Discharges with Applications in Microcombustion", *J. Phys. D: App. Phys. – Spl. Iss. on Electrical Discharges for Aerospace Applications*, Vol. 52, No. 38, 2019.
4. **G. Shivkumar**, M.A. Alrefae, S.S. Tholeti, S.O. Macheret, T.S. Fisher, and A.A. Alexeenko, "Discharge Regimes and Emission Characteristics of Capacitively Coupled Radio Frequency Argon Plasma with a Square Wave Input", *J. App. Phys.*, Vol. 125, No. 22, 2019.
3. **G. Shivkumar**, V. Kshirsagar, T. Zhu, I.B. Sebastiao, S.L. Nail, G.A. Sacha, A.A. Alexeenko, "Freeze-Dryer Equipment Capability Limit: Comparison of Computational Modeling with Experiments at Laboratory Scale", *J. Pharm. Sci.*, 2019, DOI: https://doi.org/10.1016/j.xphs.2019.04.016.
2. S.S. Tholeti, **G. Shivkumar**, A.A. Alexeenko, "Field Emission Microplasma Actuation for Microchannel Flows", *J. Phys. D: App. Phys.*, Vol. 49, No. 21, 2016.
1. **G. Shivkumar**, S.S. Tholeti, M.A. Alrefae, T.S. Fisher, and A.A. Alexeenko, "Analysis of Hydrogen Plasma in a Microwave Plasma Chemical Vapor Deposition Reactor", *J. App. Phys.*, Vol. 119, No. 11, 2016 – **Featured Cover Article**.

CONFERENCE PROCEEDINGS/PRESENTATIONS (* denotes speaker)

9. **G. Shivkumar***, S.S. Tholeti, M.A. Alrefae, S.O. Macheret, T.S. Fisher, A.A. Alexeenko, "Gas Composition and Input Waveform Effects on Alpha-to-Gamma Transitions in CCRF Plasma", *59th APS DPP*, Oct. 23-27, 2017, Milwaukee, WI.
8. **G. Shivkumar***, A.A. Alexeenko, "Carbon Nanostructure Synthesis Optimization and Application for Microchannel Flow Actuation", *WIAS*, May 31-Jun 1, 2017, Boulder, CO.
7. A.D. Strongrich, **G. Shivkumar***, A.A. Alexeenko, "Dark-to-arc Transition in Air for Planar Electrodes with Microscale Gaps", *44th IEEE ICOPS*, May 21-25, 2017, Atlantic City, NJ - **Invited Talk**.
6. **G. Shivkumar***, S.S. Tholeti, S.O. Macheret, M.A. Alrefae, T.S. Fisher, A.A. Alexeenko,"Modeling of Capacitively Coupled RF Discharge with Non-Sinusoidal Current Waveform", *44th IEEE ICOPS*, May 21-25, 2017, Atlantic City, NJ - **Best Student Paper Award**.
5. A.A. Alexeenko*, A.D. Strongrich, A.G. Cofer, A. Pikus, I.B. Sebastiao, S.S. Tholeti, **G. Shivkumar**, "Microdevices Enabled by Rarefied Flow Phenomena", *RGD:30*, July 10-15, 2016, Victoria, BC, Canada - **Invited Talk**.
4. S.S. Tholeti*, **G. Shivkumar**, A.A. Alexeenko, "Field Emission Microplasma Actuated Microchannel Flow", *57th APS DPP*, Nov. 16-20, 2015, Savannah, GA.
3. S.S. Tholeti, **G. Shivkumar**, A.A. Alexeenko*, "PIC/ MCC Simulations of Field Emission Microplasma Pump", *DSMC:2015*, Sep. 13-17, 2015, Kauai, HI.

2. S.S. Tholeti*, **G. Shivkumar**, A.A. Alexeenko, "Field Emission Driven Microplasma Pump", *8th IWM*, May 11-15, 2015, Newark, NJ.
1. **G. Shivkumar***, S.S. Tholeti, A.A. Alexeenko, "Microchannel Flow Enhancement by Microplasma Actuation", *13th ASME ICNMM*, July 6-9, 2015, San Francisco, CA.

POSTER PRESENTATIONS

8. Annual Meeting of the ISLFD, 2019.
7. LyoHUB/ASTM Workshop on Lyophilization and Pharmaceutical Manufacturing Research, 2018 - **1st Place Poster Award**.
6. Annual Meeting of the ISLFD, 2018 - **Thomas Jennings Student Paper Award**.
5. Women in Aerospace Symposium, 2017.
4. Annual Meeting of the ISLFD, 2016.
3. SMART Films Industry Day, 2016.
2. 13th ASME ICNMM, 2015.
1. SMART Films Industry Day, 2015.

RESEARCH PROPOSAL WRITING CONTRIBUTIONS

2. National Science Foundation PFI-RP No. 1827717: "Sensors, Computational Modeling, and Bioanalytical Technologies for Closed-Loop Lyophilization", PI: Alina A Alexeenko, $750,000 Awarded on Sep 15, 2018.
1. National Science Foundation: "Fundamental Studies of Field-Emission Plasmas for Microcombustion", PI: Alina A Alexeenko, 2016.

ONLINE OPEN-SOURCE TOOLS

- First Author, "LyoPRONTO", https://www.lyopronto.org
- Co-Author, "Argon Radiation Model", https://nanohub.org/resources/crmatomic

- Co-Author, "Lyo-Calculator", https://pharmahub.org/resources/lyocalculator

RESEARCH MENTORSHIP

- Aravind Shaj, B. Tech Student at IIT Madras Department of Aerospace Engineering, Chennai, India, Purdue Undergraduate Research Experience.
- Shrividya Subramanian, BS Student at Purdue School of Aeronautics and Astronautics, West Lafayette, IN, USA, Undergraduate Individual Study Project.

PROFESSIONAL ACTIVITIES AND SERVICE

School, College, University Service

- Co-Chair, Organizing Committee, Inaugural Amelia Earhart Summit, Oct 1, 2018
- Student Leadership Council Member, Purdue AAE, 2018-2019
- President and Ambassador, Purdue AAE Graduate Women's Gatherings, 2017-2019
- Graduate Student Mentor, Aero Assist, Purdue University, 2014-2019

Reviewing Activity

Journal of Physical Chemistry, Physical Review E, Journal of Applied Physics, Journal of Physics D: Applied Physics, 2nd ASTFE Thermal and Fluids Engineering Conference and 4th International Workshop on Heat Transfer.

Outreach Activity

Mentor & Volunteer, Girl Powered STEM Mentoring, Wawasee High School, Syracuse IN, Oct 7, 2017.